Ultrasonic Modeling and Simulation of Cast Austenitic Stainless Steel

3002013160

Ultrasonic Modeling and Simulation of Cast Austenitic Stainless Steel

3002013160

Technical Update, November 2018

EPRI Project Manager
M. Dunlap

All or a portion of the requirements of the EPRI Nuclear
Quality Assurance Program apply to this product.

YES (NO)

ACKNOWLEDGMENTS

This publication is a corporate document that should be cited in the literature in the following manner:

Ultrasonic Modeling and Simulation of Cast Austenitic Stainless Steel. EPRI, Palo Alto, CA: 2018. 3002013160.

ABSTRACT

This research proposes an experiment-based strategy to set up ultrasonic models and simulations aiming at accurately simulating ultrasonic testing in a coarse grain material such as cast austenitic stainless steel (CASS). The software used for this study was the French Alternative Energies and Atomic Energy Commission's (CEA's) CIVA. A simulated parametric study of coarse grain settings was conducted by performing a best match with experimental data. The comparison of experimental and simulated data provided a testament to the relevance of the simulations when considering the inherent random material characterization limits of CASS, as well as pointing to certain restrictions with the modeling software.

Keywords
CASS
Cast austenitic stainless steel
CIVA
Modeling and simulation
NDE
Ultrasound

Deliverable Number: 3002013160

Product Type: Technical Report

Product Title: Ultrasonic Modeling and Simulation of Cast Austenitic Stainless Steel

---

PRIMARY AUDIENCE: Nondestructive evaluation (NDE) researchers, software developers, and managers

SECONDARY AUDIENCE: Regulatory bodies

KEY RESEARCH QUESTION

Can an ultrasonic modeling and simulation workflow using a commercially available software be proposed, and tested, for coarse grain materials such as cast austenitic stainless steel (CASS)?

RESEARCH OVERVIEW

This project aims to develop a proposed workflow and set of recommended practices to use when modeling coarse grain components such as CASS. The studies shown within this report were performed using a commercially available NDE modeling and simulation software, the French Alternative Energies and Atomic Energy Commission's (CEA's) CIVA. A single CASS specimen was selected for this study, and a defined set of experimental tests and simulated settings were prescribed. Quantitative amplitude measurements were made, but signal-to-noise ratio was not used as a comparative metric between simulated and experimental results.

KEY FINDINGS

- Prior to coarse grain simulations, an effort was placed on properly characterizing ultrasonic probes by using a homogeneous well-known material to define CIVA probe settings and amplitude references, and to evaluate experimental error and uncertainty.

- To minimize experimental uncertainties, a set of reference experimental immersion data was taken with a 0° longitudinal beam, and corresponding CIVA simulations were conducted. This comparison allowed for a refinement of specimen properties such as grain size, elongation, material velocity, and its velocity distribution.

- Results from a parametric study to best-fit experimental results are described within the report. The parametric study was performed with a 2.25-MHz probe because this high frequency gave maximum sensitivity with the CASS specimen's grain structure. The correspondence to experimental data was evaluated with four indicators.

- An introduction to developing and setting up CIVA coarse grain models is presented with detailed descriptions of the primary modeling inputs. Computation time for each simulation is presented in an appendix.

- A comparison is made between experimental and simulation results for a 45° longitudinal wave contact dual matrix phased array probe. The results showcase both qualitative data and amplitude responses from known features, such as side-drilled holes and a large crack.

- Limitations of the current workflow and model restrictions are presented. For instance, the version of CIVA used for this study limits the specimen to either a plate or cylindrical geometry. Other limitations are described, and future research on a cylindrical specimen is recommended.

WHY THIS MATTERS

CASS is a challenging material for NDE examination across the nuclear fleet. Reliable techniques are required for its inspection, and ultrasonic modeling and simulation can aid further development of such techniques. However, accurate and reliable coarse grain ultrasonic models and simulations must first be developed and validated. This research provides a pathway for developing and evaluating CASS models.

HOW TO APPLY RESULTS

NDE personnel can apply the proposed workflow toward their coarse grain studies. Detailed steps and recommendations for CIVA coarse grain models are described, and they can be applied to several applications.

LEARNING AND ENGAGEMENT OPPORTUNITIES

EPRI NDE staff routinely present material such as this at the annual EPRI NDE Technology Week and other industry meetings and conferences. Questions pertaining to this research can be directed to the EPRI contact listed below.

EPRI CONTACTS: Myles Dunlap, Technical Leader, mdunlap@epri.com

PROGRAM: Nondestructive Evaluation Program, 41.04.01

IMPLEMENTATION CATEGORY: Reference

CONTENTS

LIST OF FIGURES

LIST OF TABLES

1
INTRODUCTION

Ultrasonic testing (UT) of cast austenitic stainless steel (CASS), a critical material in many safety-related nuclear power plant components, is challenging due to the coarse-grained, anisotropic, and inhomogeneous nature of the material. Ultrasonic wave interaction within the material structure is subject to scattering and attenuation, resulting in reduced signal-to-noise ratios (SNRs) and difficulties in analysis and interpretation of results. Previous studies have demonstrated relations between the grain microstructure and ultrasonic wave interactions. However, no currently available and reliable nondestructive evaluation (NDE) approach exists to assess the detrimental effect that the material has upon the propagating ultrasonic wave.

Attributes of CASS

An initial step in this project was to determine a catalog of characterization properties and attributes relevant to CASS samples. For instance, CASS is a coarse grain structure with different grain types and grain orientations; therefore, grain structure was considered as a variable for experimental study. CASS microstructure can be classified as columnar, equiaxed, or a mixture thereof [1]. Furthermore, the microstructural distribution can occur in multiple bands, or layers, and can vary throughout the specimen [1]. CASS is a challenging material to inspect because not only does it have heterogenous and anisotropic material properties, but its grain size can significantly affect backscatter. The three ultrasonic scattering regimes, based on length scales, are as follows [2]:

- Specular—for objects whose size is much larger than a wavelength

- Diffractive—for objects whose size is slightly less than, or approaches, a wavelength

- Diffusive—for objects whose size is much smaller than a wavelength

Assuming a CASS specimen has a longitudinal wave (L-wave) velocity of 5,800 m/s, then the wavelengths for three expected inspection frequencies can be calculated as follows:

- 0.5 MHz has a wavelength of 11.6 mm.

- 1.0 MHz has a wavelength of 5.8 mm.

- 1.5 MHz has a wavelength of 3.9 mm.

One study found CASS average grain diameter measurements ranged from 2.6 mm to 10.3 mm with a maximum of 41 mm [3]. Thus, when comparing the typical wavelengths used for industrial ultrasonics, it's clear that they are near, or smaller than, the average grain size for CASS. Specular reflectors produced a pressure wave that does not vary with frequency [2], and features such as flaws and geometry (for example, counterbore and weld root) provide specular reflections. CASS grains will also produce specular reflections, and their ultrasonic appearance will likely resemble that of a flaw. This makes the signal interpretation difficult for CASS

materials because the large grains produce what is commonly called "noise," and its signal characteristics are nearly identical to flaws. With consideration given to the scattering, attenuation, heterogeneous, and anisotropic nature of CASS, the challenges for its inspection become more apparent.

When the study was designed, an initial test piece, designated as J7010-4, was selected that represented a columnar grain structure with grain sizes near a wavelength. Several test specimens have been developed for the nuclear industry throughout the years; the specimen selected for this study needed to have known geometric reflectors, defects, and a well-characterized large grain structure to help build a well-controlled model. Once a workflow for ultrasonic modeling and simulation is proposed for the first test specimen, more complex pieces with other defects, grains, and geometrical configurations can be evaluated. Understanding the role each of these variables plays is important, and ultrasonic modeling and simulation can potentially serve as another tool to aid in further discerning, and predicting, the behavior of this complex material.

Research Objective and Purpose

This project aims to develop a proposed workflow and set of recommended practices to use when modeling coarse grain components such as CASS. The studies shown within this report were done with the French Alternative Energies and Atomic Energy Commission's (CEA's) CIVA, a commercial NDE modeling and simulation software [4]. A set of specimen attributes was reviewed, as described above, and a single specimen was selected for this initial study.

Work Plan for Evaluating CASS Simulations

EPRI requested that EXTENDE [5] assist with the development of the proposed ultrasonic workflow for CASS samples using CIVA. This report proposes an experiment-based strategy for developing CIVA models that accurately simulate such materials. This simulation study was achieved with the latest commercial release of CIVA, CIVA 2017 SP1.

The research methodology followed the work plan depicted in Figure 1-1. Blue boxes represent the tasks for sizing the grains from J7010-4's macrographs. Green boxes represent the tasks requiring experimental activities: probe and material characterization, as well as data collection on J7010-4 to be compared with simulations. Orange boxes represent the tasks requiring CIVA simulation activities.
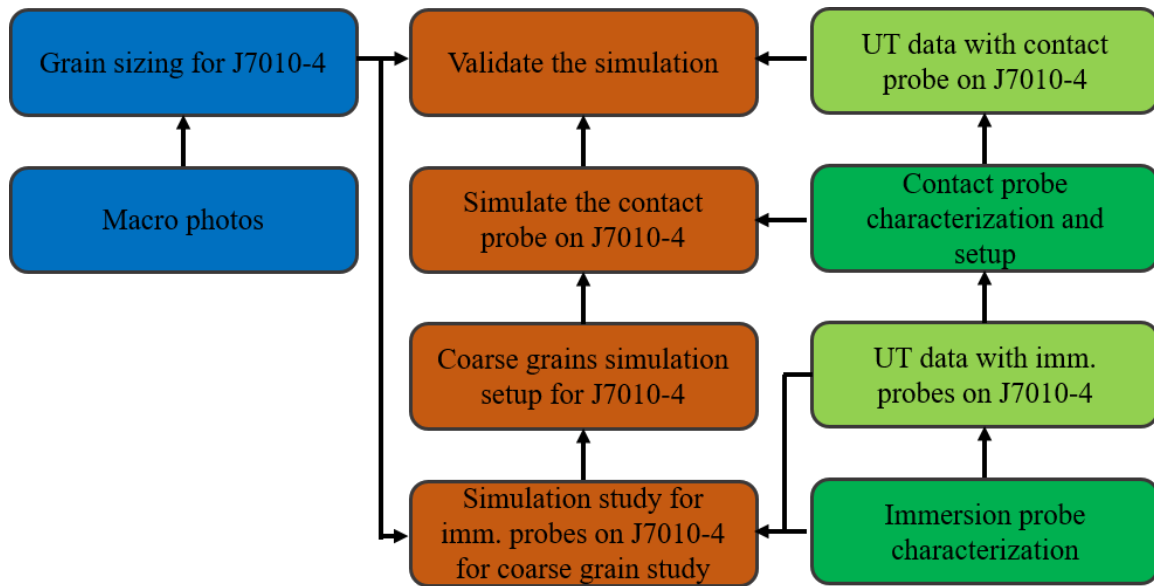
Figure 1-1
Work plan for evaluating CASS simulations
Note: imm. = immersion

The study performed the following steps:

- Select probes (three different frequencies).

- Characterize the probes.

- Collect experimental data with these probes on the CASS sample.

- Analyze the bottom face echo from the experimental data.

- Photograph and analyze the given test specimen to determine the grain size and elongation.

- Set up the initial coarse-grained material simulation with information taken from experimental data and macro photos.

- Evaluate the computational parameters required for proper results.

- Evaluate the influence of the coarse grain simulation parameters.

- Improve the coarse-grained structure setup to make the simulation data best match the experimental data.

The obtained CIVA coarse grain setup was then tested in an inspection scenario involving an angled beam interacting with known defects and geometries.

2
TEST SPECIMENS AND EQUIPMENT SETUP

Test Samples

Reference Sample

The reference sample (Figure 2-1) was a block made of homogeneous carbon steel, with 25 side-drilled holes (SDHs), each having a 2-mm diameter. These were located from 4 mm to 100 mm in depth, with a horizontal slope of 15° and a vertical step of 4 mm. This block was designed to characterize probes, identify their beam properties, and serve as a reference for amplitude calibrations.
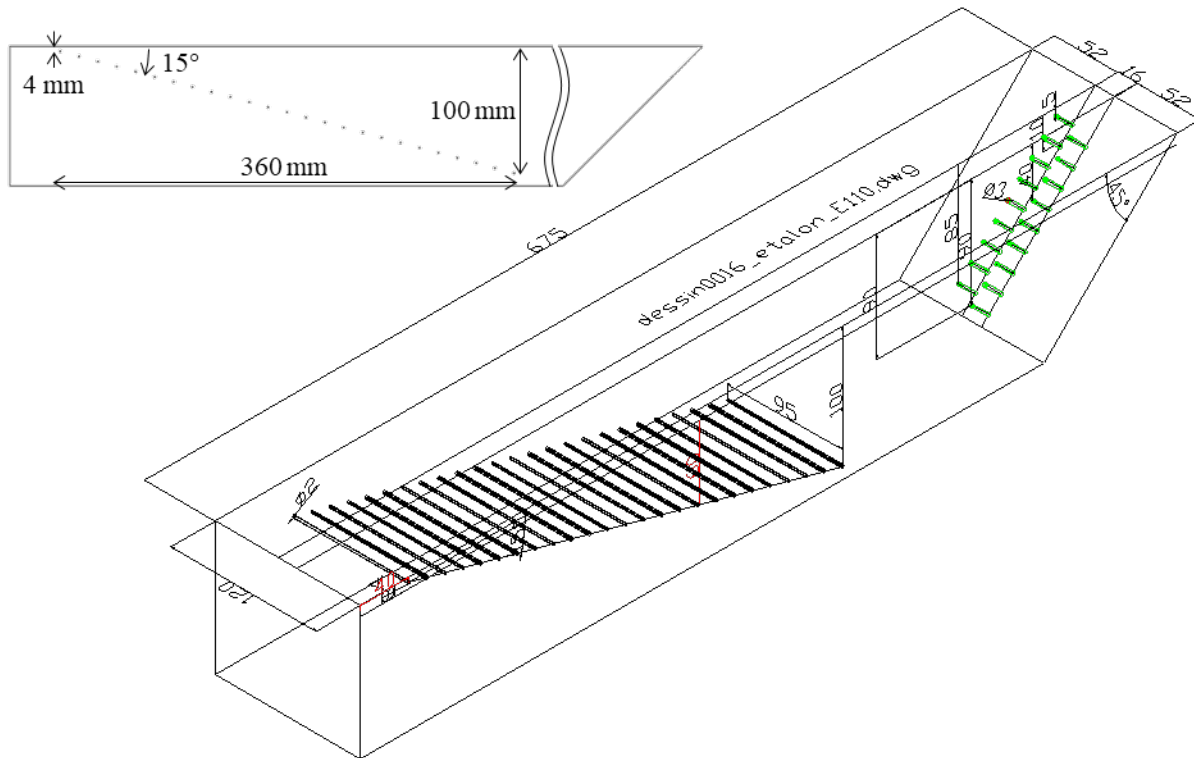
Figure 2-1
Reference sample geometry (dimensions given in millimeters)

CASS Test Specimen J7010-4

J7010-4 (Figure 2-2) is a block made of coarse grain stainless steel and is the sample under investigation within this study. Its geometry is a plane extrusion of the displayed section, containing four SDHs having a diameter of 1.6 mm, two electrical discharge machining cracks, one simulated weld root, and one radius. This sample does not contain a weld.
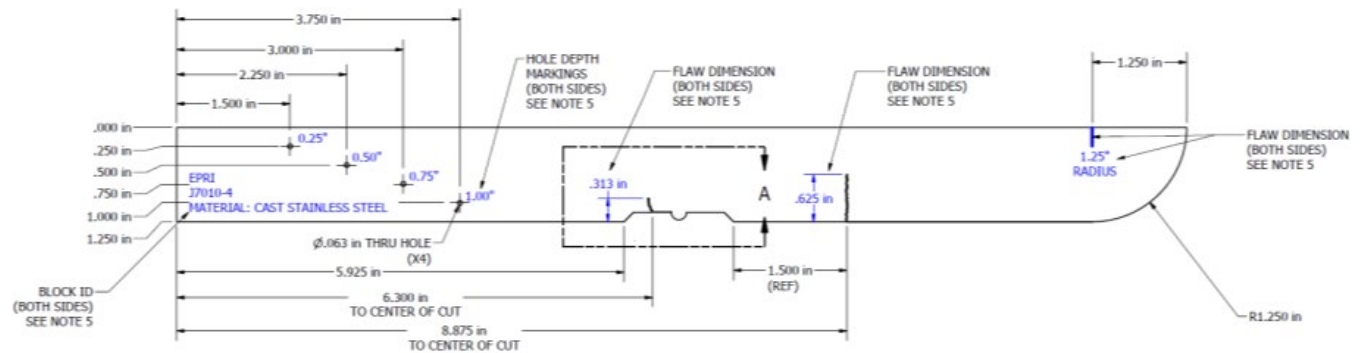
Figure 2-2
J7010-4 sample geometry

Sample J7010-4 was polished and etched to reveal its grain microstructure. A set of photographs was taken of each side to provide the ability to measure its grain structure (Figure 2-3). As seen in the side view of Figure 2-3, the grain structure is columnar.
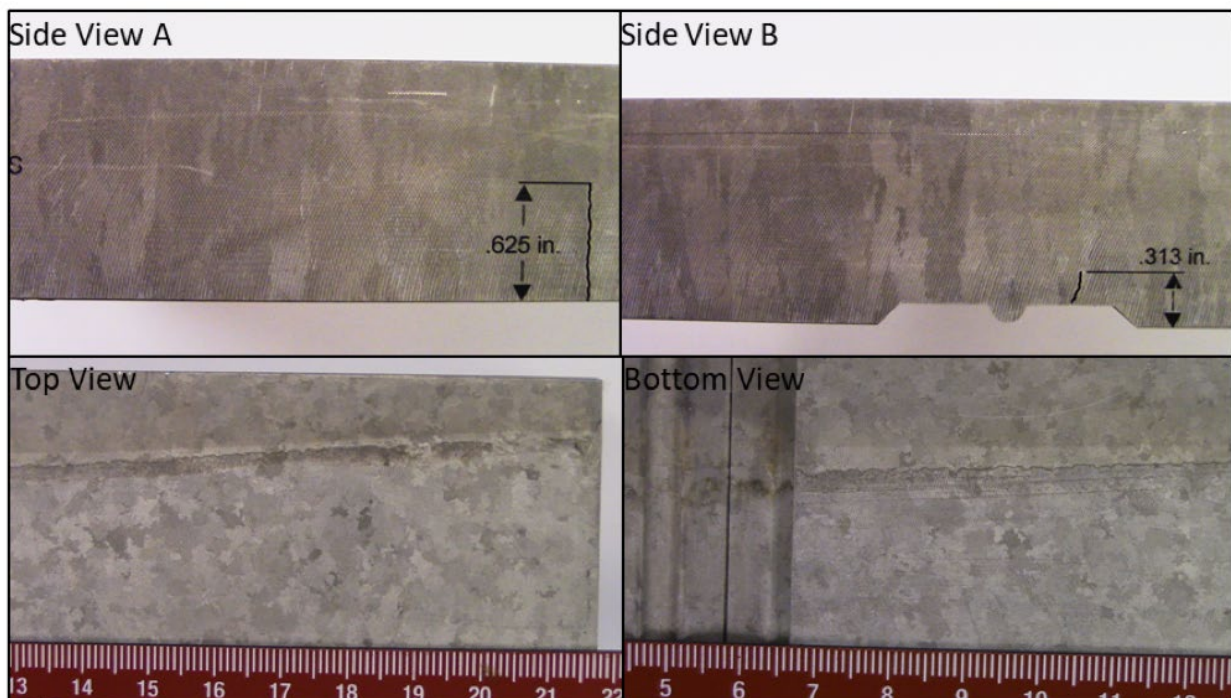
Figure 2-3
Macrographs of grain structure

Ultrasonic Probes

Three immersion probes (Figure 2-4) and one contact probe (Figure 2-5) were used for the study.
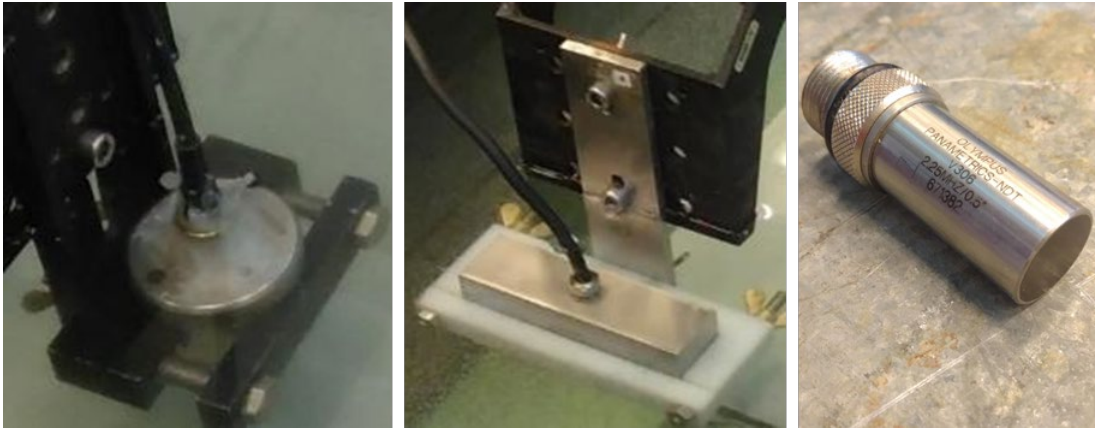
Figure 2-4
Immersion probes—500 kHz (left), 1 MHz (center), and 2.25 MHz (right)

Figure 2-5
Contact dual phased array 1 MHz

Immersion Probes—500 kHz, 1 MHz, and 2.25 MHz

Immersion probes were used to characterize the material properties of J7010-4 (see Table 2-1) for a couple of reasons. First, immersion inspection reduced potential experimental coupling issues; and second, single-element probes with longitudinal 0° inspection reduce the risk of numerical modeling and experimental errors.

One 64-element phased array transducer was used for material characterization, and it performed electronic scanning (E-scans) in the index axis with 14 elements. This probe was chosen because a 1-MHz single-element probe was not available for the study; thus, the phased array was used to reproduce the behavior of a single square element. This allowed for mechanical and E-scans to be performed in the scanning and index axes, respectively.

Table 2-1
Immersion probe—nominal settings used for material characterization of J7010-4

500 kHz	1 MHz Phased Array	2.25 MHz
• Immersion probe single element	• Immersion probe 64 elements linear phased array	• Immersion probe single element
• Circular crystal with a 37-mm diameter	• Pitch 1.4 mm (0.5-mm gap between elements)	• Circular crystal with a 12.7-mm diameter
• No crystal focusing	• 20-mm element elevation	• No crystal focusing
• Nominal frequency 500 kHz	• No crystal focusing	• Nominal frequency 2.25 MHz
	• Nominal frequency 1 MHz	
	The electronic settings are as follows:	
	• Electronic scan: 14-elements aperture with 1-element step	
	• No steering	

Contact Dual Phased Array—1 MHz

The contact probe was aimed at performing an angled beam inspection to evaluate the coarse grain modeling. Its nominal settings were as follows:

- Dual matrix array 2 (columns) × 16 (rows)

- Mean frequency: 0.976 MHz with a -6dB bandwidth of 65.31%

- Pitch 3.5 mm (primary axis) × 7.5 mm (secondary axis)

Information measured on the wedge using computer-aided design:

- Wedge length: 70 mm

- Wedge width: 51 mm

- Flat wedge surface

- Incidence angle: 18°

- Roof angle: 2°

Information observed with the transducer and wedge:

- Element numbering:
  – Priority: lines/columns
  – Line numbering: increasing
  – Column numbering: decreasing
  – Dual element approach: symmetrical

- Wedge velocity: 2340 m/s

The following information will be estimated using experiments conducted on the reference block as well as experienced judgment on certain parameters (see Section 3):

- Gap between rows and columns

- Distance between the two arrays (*L6* in Figure 2-6)

- Central sound path in the wedge (*L4* in Figure 2-6)

- Central exit point (*L2* in Figure 2-6)
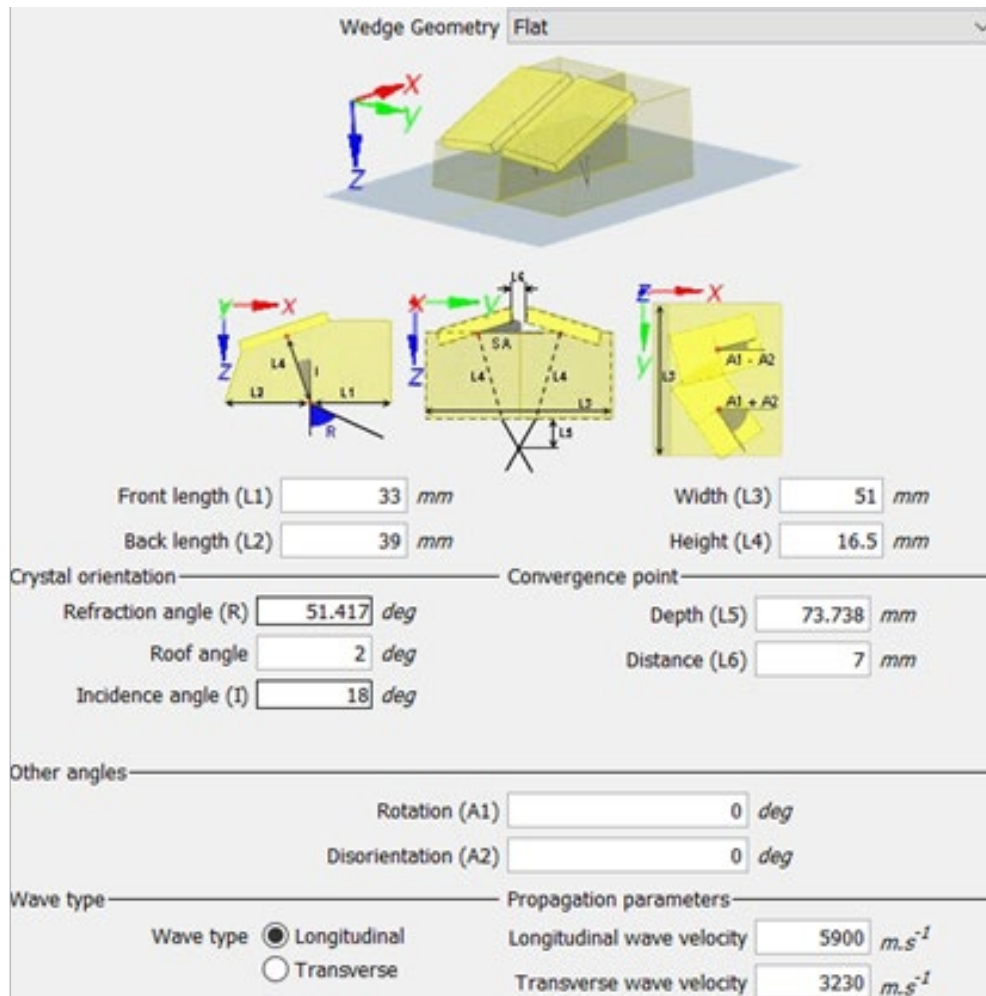
Figure 2-6
CIVA definitions

Experimental Setup for Data Collection

The experimental setup used a three-axis linear motion system (Figure 2-7) and the M2M MultiX ultrasonic acquisition unit for phased arrays. The components are immersed in a water tank.
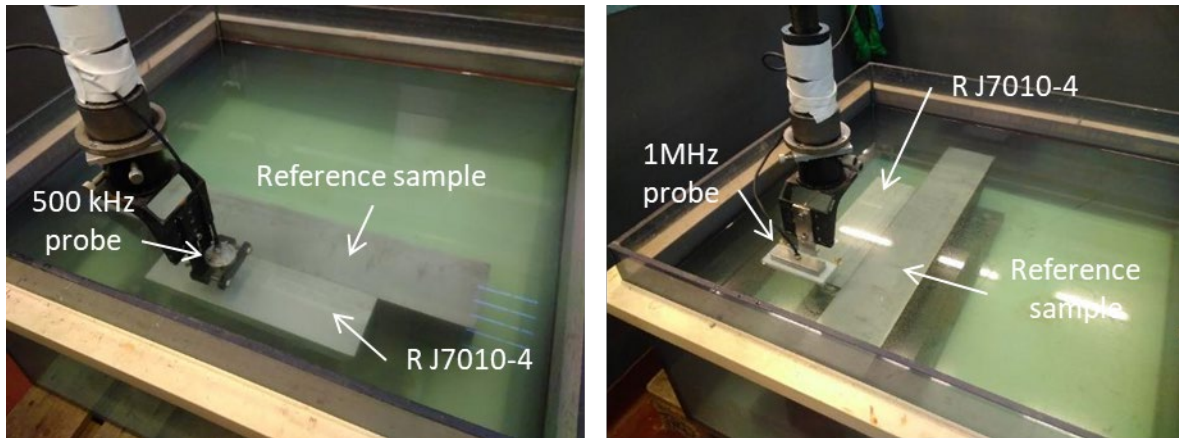
Figure 2-7
Experimental setup

3
PROBE CHARACTERIZATION

Characterization of the immersion probes is aimed at setting up the parameters of the CIVA probe panel. It is performed by collecting experimental UT data on the reference sample and comparing it (via A-scans) with corresponding CIVA simulations. The reference specimen's upper surface echo is used as the reference for the signal setting, and its SDHs are used as an amplitude reference. The amplitude reference is set on the SDH that minimizes the average error for all SDHs. The amplitude reference is set from the unrectified time-domain signal, and this is susceptible to phase sensitivity. All the simulated signals presented in this section were modeled using a Hanning shaped signal with the experimentally measured central frequency and -6 dB bandwidth for the respective probe being discussed.

Immersion Probe Characterization

500 kHz

The measured central frequency (560 kHz) and bandwidth (30%) were taken from the surface echo using the F-scan (Figure 3-1). The probe's signal phase (270°) was chosen from a set of A-scan simulations, with different values, that best match the experimental signal (Figure 3-2).
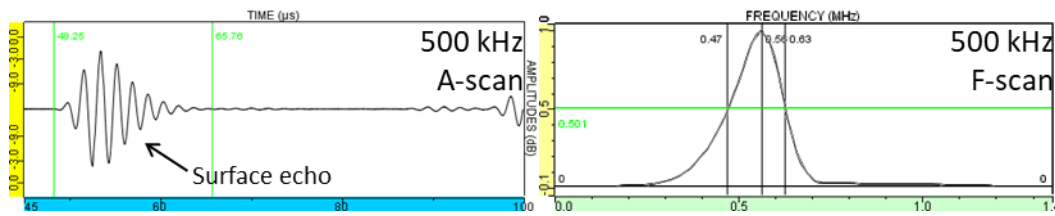
Figure 3-1
Central frequency and bandwidth extraction of 500-kHz immersion probe
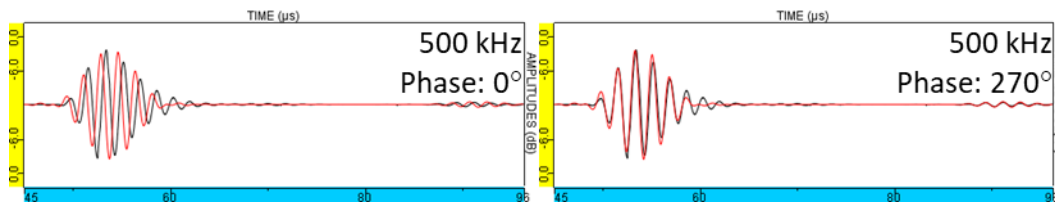
Figure 3-2
Phase extraction of 500-kHz immersion probe (black = experimental; red = simulation)

The amplitude reference was set for the 40-mm-deep SDH. Experimental (C-scan) and simulation values are reported in Appendix A to allow comparison with future results. Figure 3-3 compares the experimental (black curve) and the simulated (red curve) SDHs' responses. Black dots are given for the central position in the increment axis, and the error bars display the minimum and maximum values along the increment axis. The maximum error between simulated and experimental results was 2.0 dB. Furthermore, the SDHs' experimental response along the increment steps varied by up to 2.0 dB.
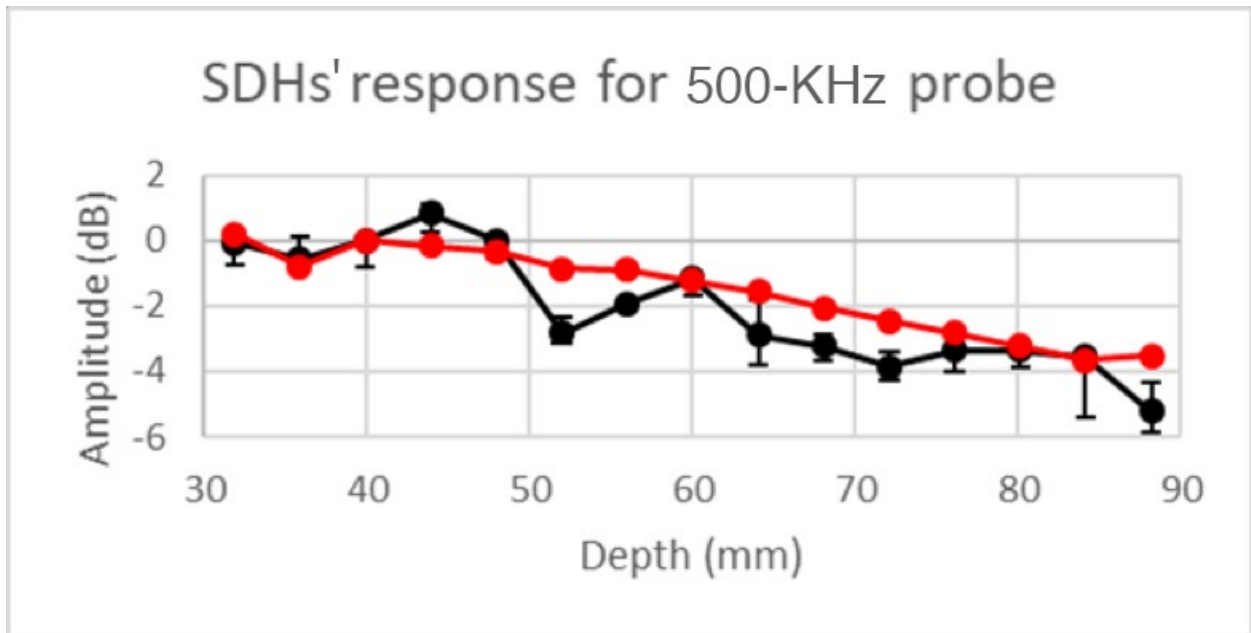
Figure 3-3
Comparison of SDHs' amplitude response for the 500-kHz immersion probe (black = experimental; red = simulation)

1 MHz

The probe was simulated with 14 active elements, which correspond to the experimental E-scan aperture. The central frequency (1.05 MHz) and bandwidth (65%) were extracted from the entry echo using the F-scan (Figure 3-4) at the central position of the experimental E-scan. The probe's signal phase (90°) was chosen from a set of A-scan simulations with different values that best match the experimental signal (Figure 3-5).
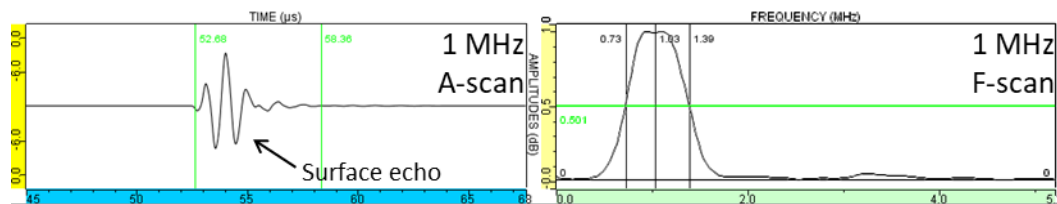
Figure 3-4
Central frequency and bandwidth extraction of 1-MHz immersion probe
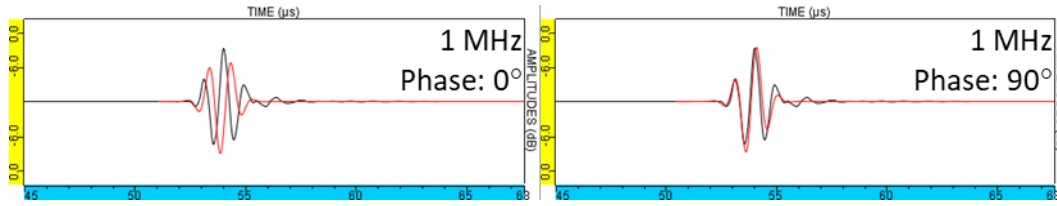
Figure 3-5
Phase extraction of 1-MHz immersion probe (black = experimental; red = simulation)

The amplitude reference was set for the 44-mm-deep SDH. Experimental and simulation values are reported in Appendix A to allow for comparison with further results. Figure 3-6 compares the experimental (black curve) and the simulated (red curve) SDHs' responses. Black dots are given for the central position in the E-scan. The error bars display the minimum and maximum values along the E-scan. The simulated maximum error is 1.7 dB and the SDHs' experimental response along the increment steps varied up to 2.5 dB.
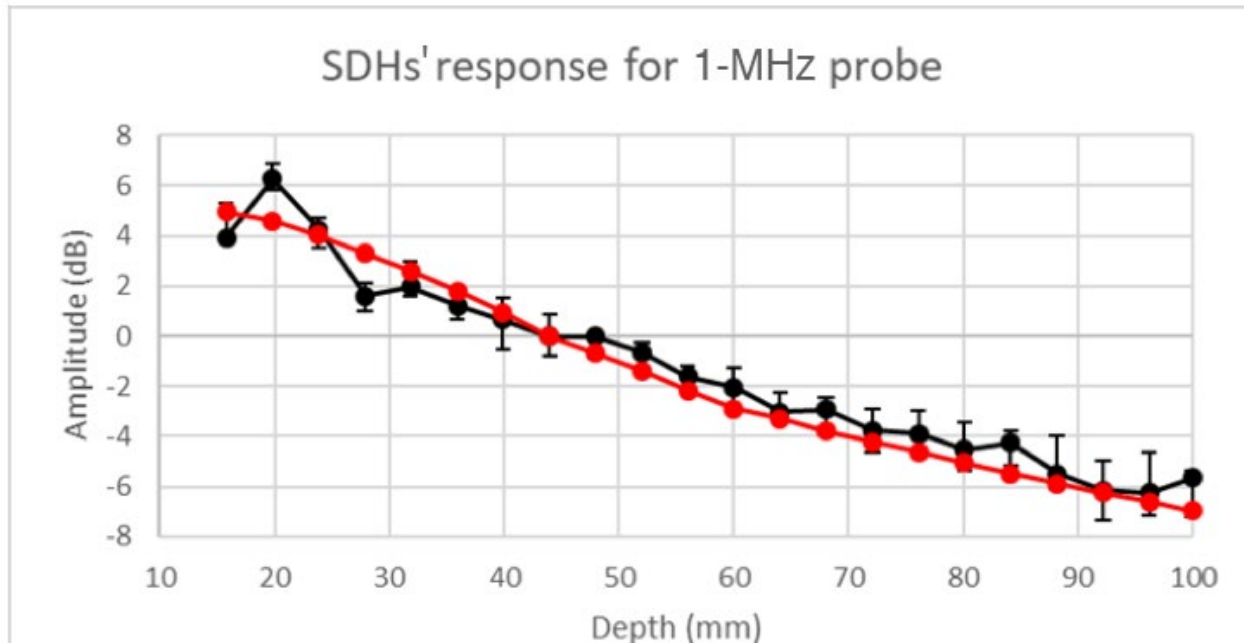
Figure 3-6
Comparison of SDHs' response for the 1-MHz immersion probe (black = experimental; red = simulation)

2.25 MHz

The central frequency (2.32 MHz) and bandwidth (58%) were extracted from the entry echo using the F-scan (Figure 3-7). The probe's signal phase (315°) was chosen from a set of A-scan simulations with different values that best match the experimental signal (Figure 3-8).
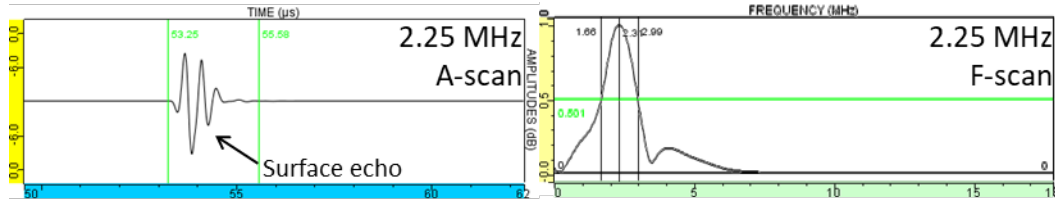
Figure 3-7
Central frequency and bandwidth extraction of 2.25-MHz immersion probe
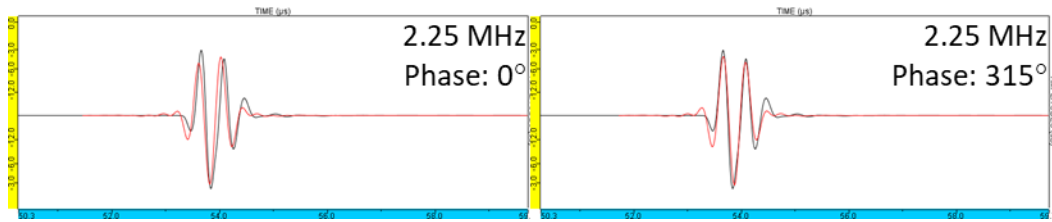
Figure 3-8
Phase extraction of 2.25-MHz immersion probe (black = experimental; red = simulation)

The amplitude reference was set for the 36-mm-deep SDH. Experimental and simulation values are reported in Appendix A to allow for comparison with further results. Figure 3-9 compares the experimental (black curve) and the simulated (red curve) SDHs' responses. Black dots are given for the central position in the increment axis, and the error bars display the minimum and maximum values along the increment axis. The simulated maximum error is 0.9 dB, and the SDHs' experimental response along the increment steps varies up to 1.4 dB.
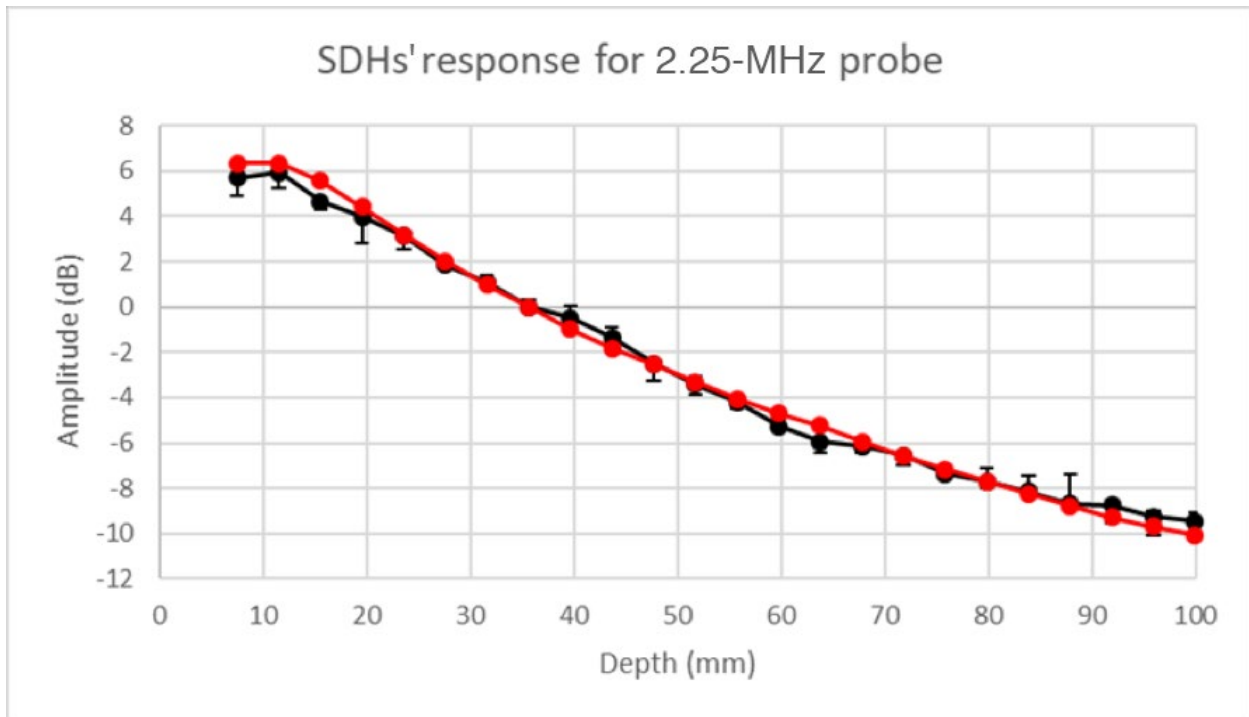
Figure 3-9
Comparison on SDHs of the 2.25-MHz immersion probe characterization (black = experimental; red = simulation)

Contact Probe Characterization

As per the immersion probes, the contact probe must be characterized to check the correct settings and define the reference values (Appendix A), allowing a comparison between experimental and simulation data. The description of the contact probe given in Section 2 allows setting all the parameters except the height ($L4$) and the distance between the arrays ($L6$), both set in CIVA's *Wedge Geometry* tab. Initial values are $L4 = 16.5$ mm and $L6 = 7$ mm.

The probe is first scanned on the characterization sample with null delay laws. The signal phase, the reference amplitude, and the wedge height are set on the 48-mm-deep SDH (Figure 3-10). The wedge height $L4 = 18$ mm matches the echo's time of flight (TOF), and the 20° phase matches the signal shapes. An A-scan's phase as manually adjusted to temporally align the experimental and simulated signal's shape peaks from the reflectors. When Figure 3-10 is viewed, only slight differences are observable between the 0° and 20° phase.
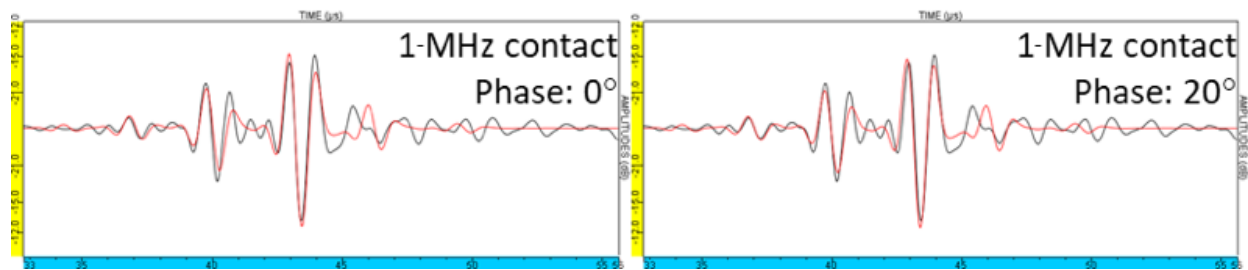
Figure 3-10
Phase extraction of the contact probe (black = experimental; red = simulation)

Figure 3-11 compares the experimental and the simulated SDHs' responses for both null delay law and one-point focus at 32-mm and 45° beam steering. The simulated maximum error is 2.0 dB for the null delay law and 1.9 dB for the 32-mm deep focusing. The SDHs' experimental response along the increment steps varies up to 3.4 dB for the null delay law and 1.3 dB for the 32-mm deep focusing.

Figure 3-12 displays the −12-dB beam shape with null delay law. The first 47 mm in depth appears to produce a complex beam shape that could be incorrectly simulated by CIVA as per the near field due to constructive and destructive wave interference phenomena. Ideally, the sound beam's shape would be measured experimentally and further used to compare with simulated results. Nonetheless, this explains the lowering of the experimental curve of Figure 3-11 (left) compared with simulation that occurs between 30-mm and 47-mm deep and the highest experimental variations along increments in the first 47 mm of depth. Due to this reason, only SDHs deeper than 47 mm shall be considered for the simulation agreement.
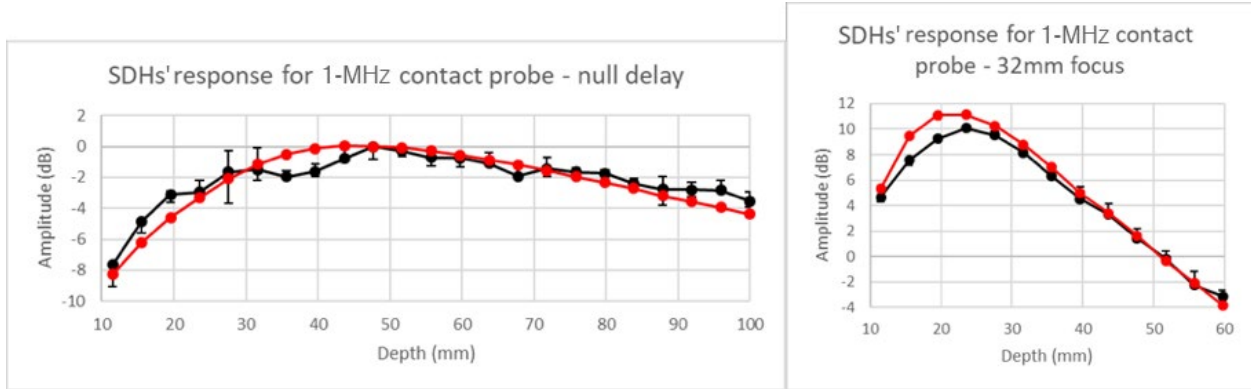
Figure 3-11
Comparison of SDHs' response for the contact probe for initial *L6* (black = experimental; red = simulation; left = null delay laws; right = 32 mm deep focusing)
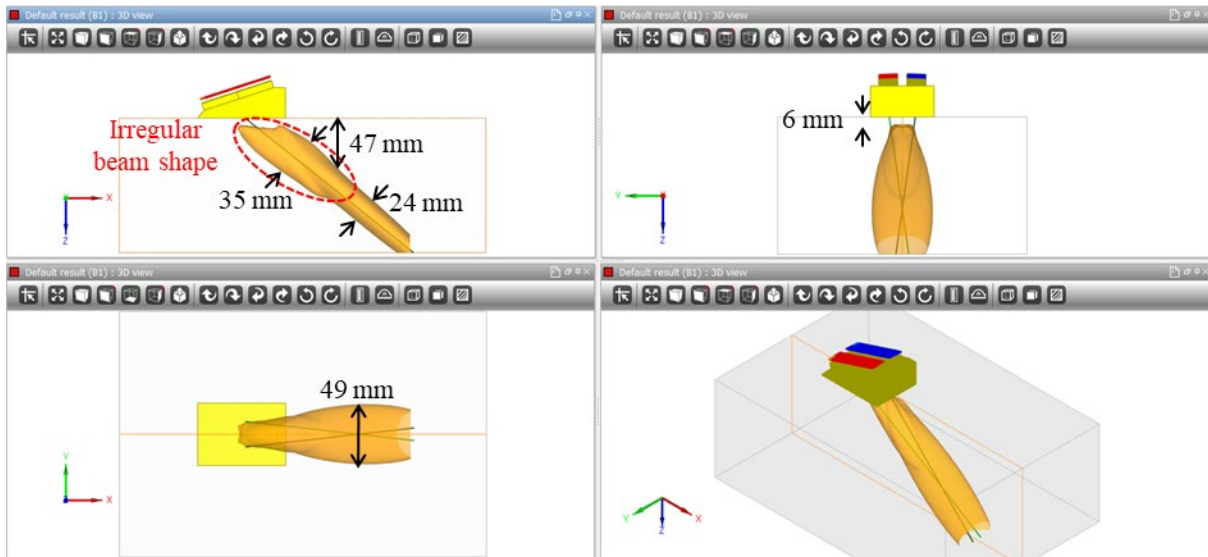
Figure 3-12
Simulated beam of the contact probe in the characterization sample with null delay law

Figure 3-13 displays the −12-dB beam shape while focusing at 32-mm depth with 45° steering. It is much better shaped than the null delay beam simulation and is more inclined to comparison with experimental data. This is confirmed by lower variations in the Figure 3-11 (right). All SDHs shall be considered for the simulation agreement with the one-point focusing.
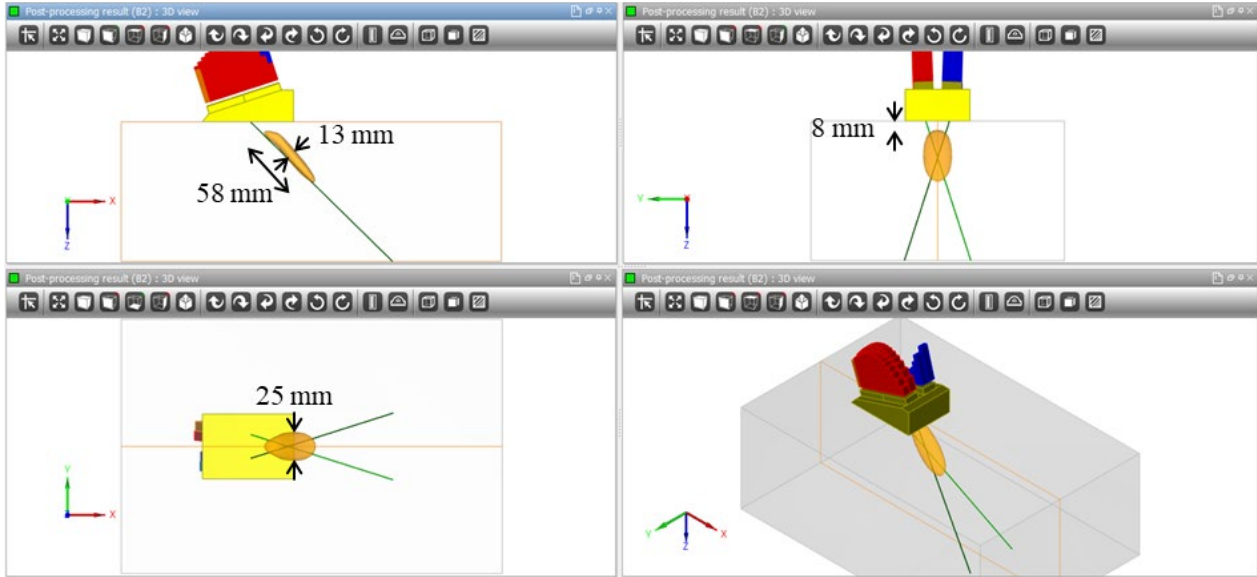
Figure 3-13
Simulated beam of the contact probe in the characterization sample with 32 mm at 45° steering

Simulations were then performed to find the value of the probes' separation distance (*L6*) offering the best agreement to experimental data, and the value *L6* = 10 mm was chosen. The simulated SDHs' responses were compared to experimental data in Figure 3-14 for the two delay laws. As described above, the comparison does not account for 10-mm to 45-mm-deep SDHs using the null delay law. The simulated maximum error is 1.0 dB for the null delay law and 1.1 dB for the 32-mm-deep focusing.
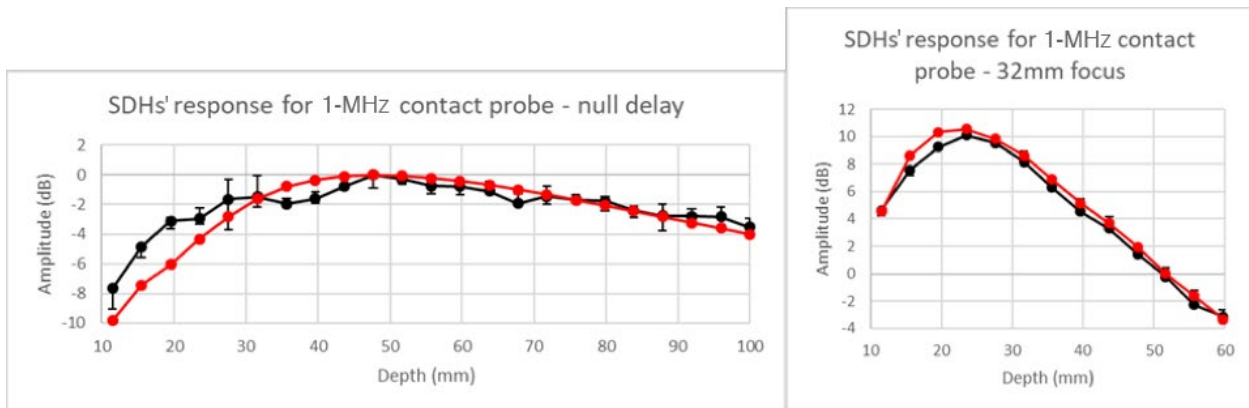
Figure 3-14
Comparison of SDHs' response for the contact probe for chosen *L6* (black = experimental; red = simulation; left = null delay laws; right = 32 mm deep focusing)

Figure 3-15 shows the beam simulated in the J7010-4 component modeled in CIVA. The beam is directly impacted by the local grain structure, and its shape changes for each position.
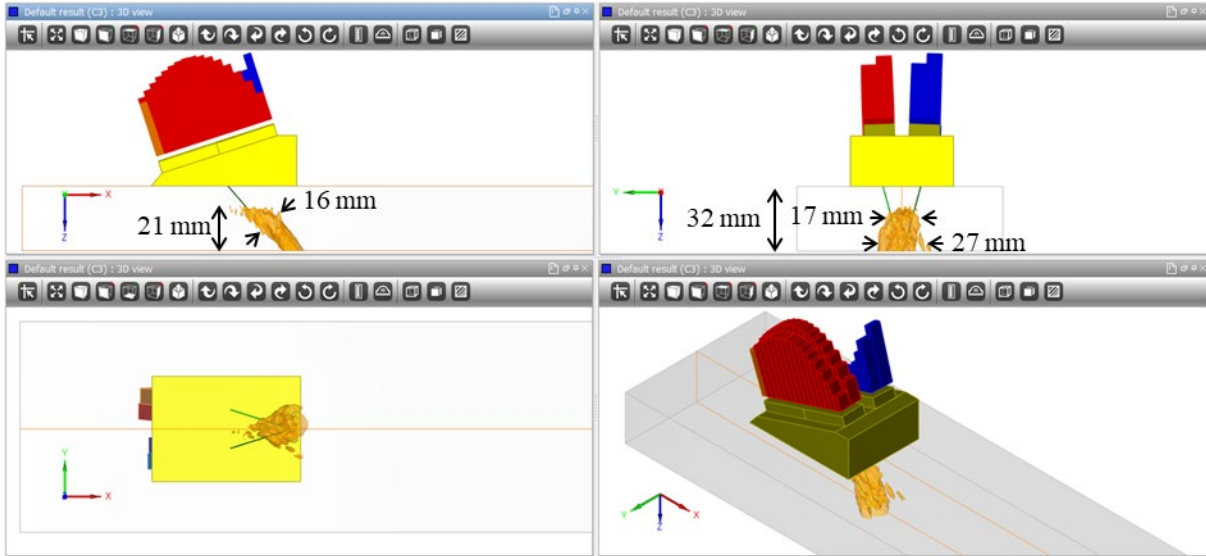
Figure 3-15
Simulated beam of the contact probe in the coarse grain structure with 32 mm at 45° steering

4
J7010-4 GRAIN-SIZE MEASUREMENTS

The physical size of grains in J7010-4 was measured to initialize CIVA parameters prior to fine-tuning the model parameters. Limitations such as the amount of polished and etched material surface and photo quality impede a highly accurate measurement, and for this reason values have been rounded within this section.

Selection Criteria

Macrographs were taken at the side, bottom, and top of J7010-4 (see Figure 4-1). The grains were predominantly vertically elongated from the bottom to top surface (that is, columnar). For the context of this report, a macrograph is a photograph taken at a scale such that its features are visible by the naked eye. The top and bottom surface macrographs show equiaxed grain sections, and side macrographs indicate columnar grain sections. Measurements were performed on the photographs in Figure 4-1 with the following considerations:

- Photographs should not overlap; measuring the same grains several times spoils the statistics.

- Each photograph should have a dimensional reference, a ruler or marking on the component.

- Photographs should be taken with the lens facing normal to the surface to minimize parallax that distorts the dimensions.

- Photographs should clearly show the grain structure after processing, if necessary.
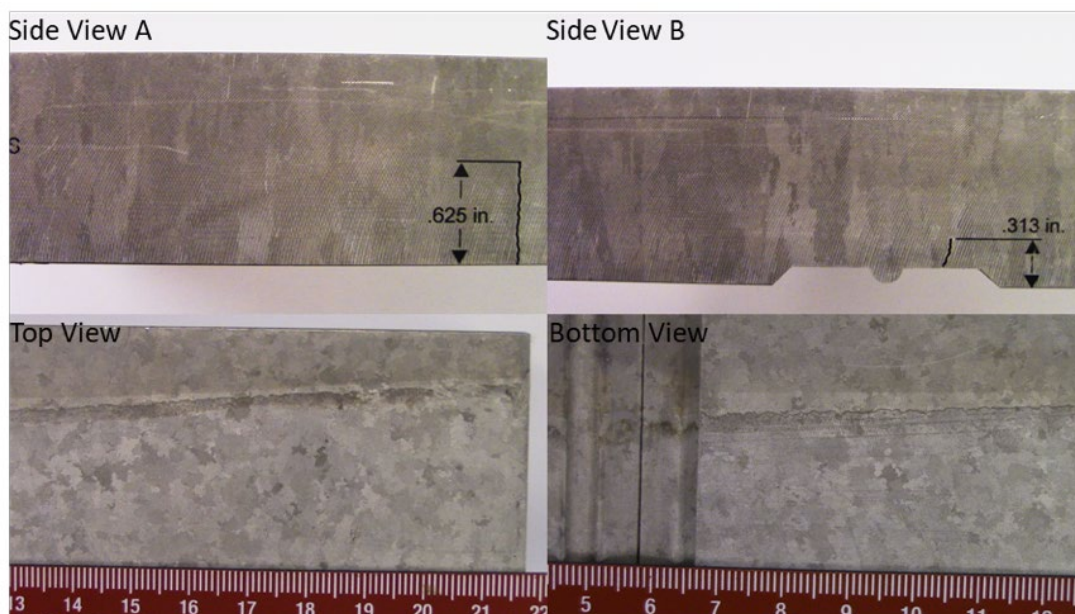
Figure 4-1
J7010-4 macrographs

Image Processing

The main difficulty encountered when analyzing the photographs was the subtle machining ridges on the bottom surface of J7010-4 (Figure 4-2). Image processing was applied on the photographs to solve this problem. The photographs were scaled to 10 pixels per millimeter to increase the contrast of the photograph for better grain measurements. The processing was done using the software ImageJ [6]. Figure 4-3 and Figure 4-4 show the processed images.

Figure 4-2
Impact of machining ridges
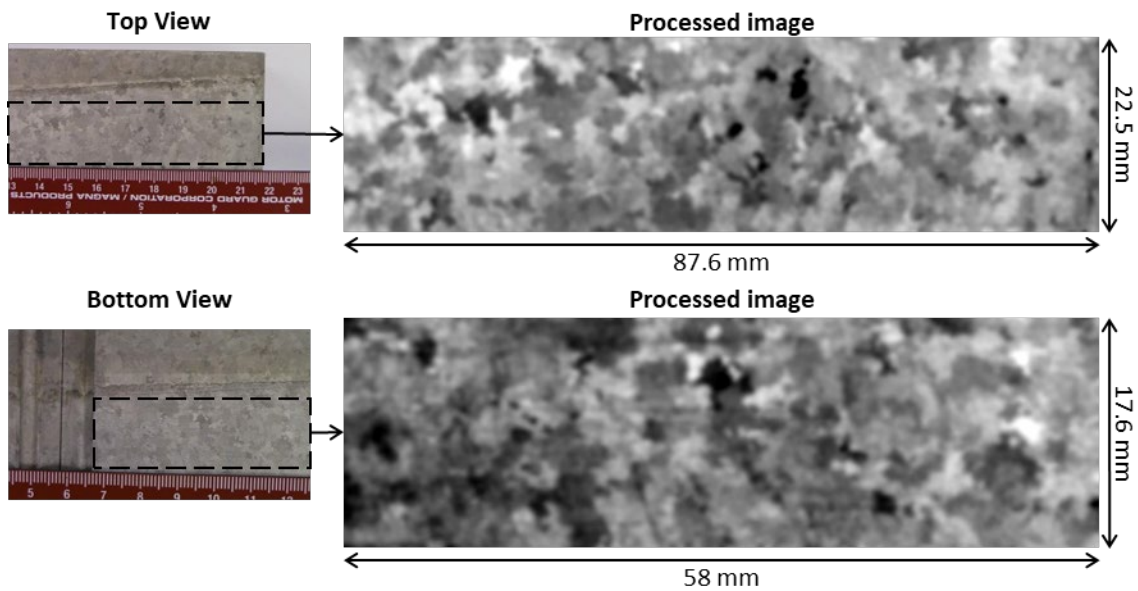
Figure 4-3
Image processing for top/bottom macrographs
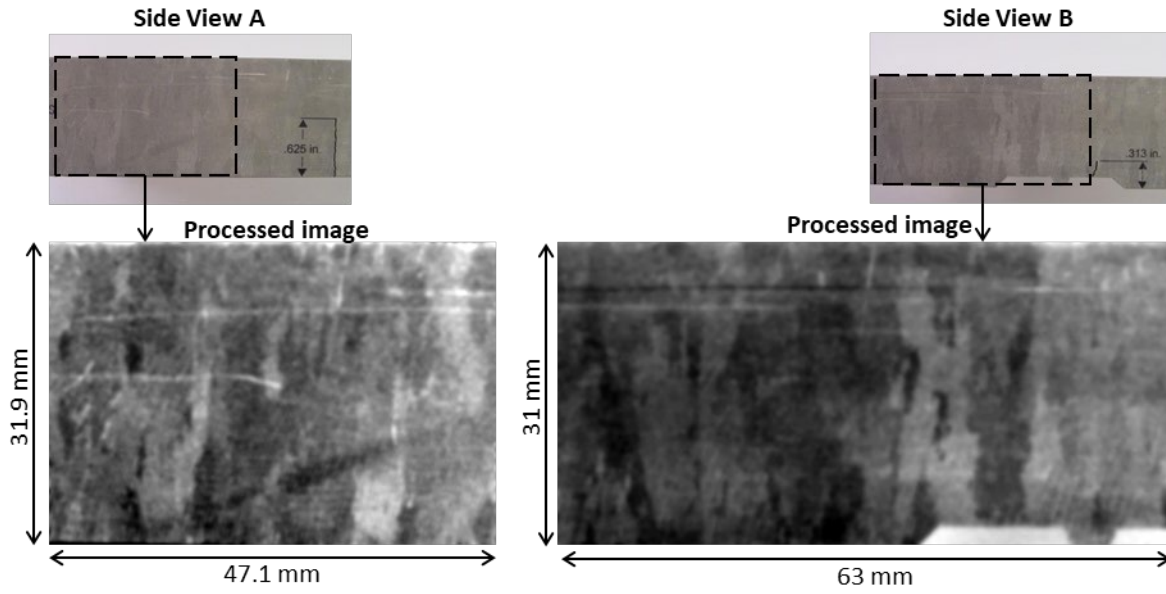
Figure 4-4
Image processing for side macrographs

Grain Sizing

From the processed images, the grains are manually traced and counted on tracing paper (Figure 4-5).
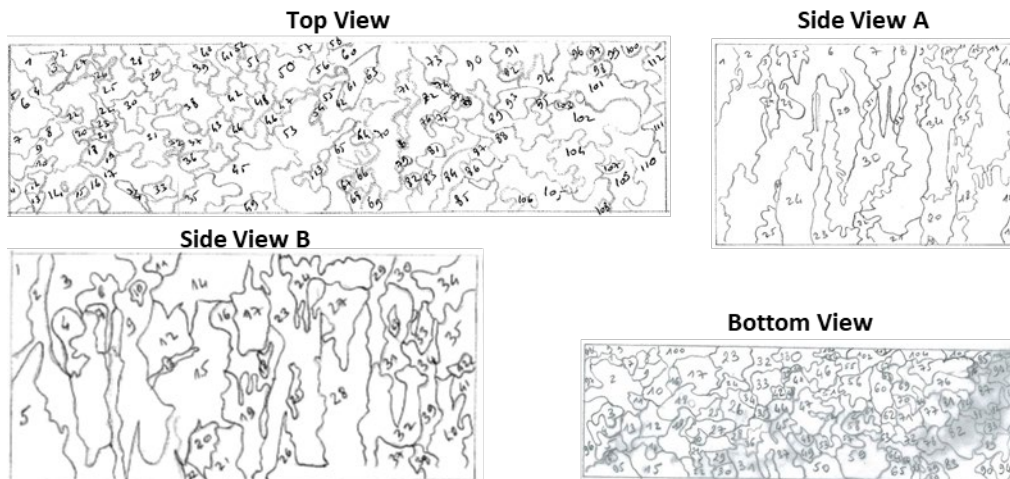
Figure 4-5
Manual grain counting

The imaging area and grain counts for the top and bottom views are given in Table 4-1. Since the grain structure for the top and bottom surface appears equiaxed, they will be assumed to have equal length sides (that is a square geometry approximation). Therefore, the mean sides for the top and bottom view are 4.3 mm and 3.0 mm, respectively. Averaging these values and rounding to the nearest 0.5 mm provides a cross-sectional grain size (s) of 3.5 mm for the top and bottom views.

Table 4-1
Cross-sectional grain size from the top and bottom views

Image	Image Area	Grain Count	Mean Grain Area	Grain Size (*s*)
Top view	1968.75 mm^2	113	17.4 mm^2	4.2 mm
Bottom view	1020.8 mm^2	110	9.3 mm^2	3.0 mm
Considered value			12.25 mm^2	3.5 mm

Side views A and B (see Figure 4-5) grain measurements are given in Table 4-2. Since the grains are columnar, their height (h) will be approximated assuming a rectangular geometry, and the width is taken from the previously measured cross-sectional grain size of 3.5 mm for the top and bottom views. Therefore, the mean grain area for side views A and B can be used to calculate the mean height of the grains in J7010-4. A considered value of 12.25 mm was used for h. The grain height was calculated as grain height is equal to the elongation x grain size; where the grain elongation is 3.5 (see Table 4-2) and grain size is 3.5 mm (see Table 4-1). Grain elongation (h/s) was calculated as 3.5, when rounding to 0.5 is considered (see Table 4-2).

Table 4-2
Side view A and B grain sizing

Image	Image Area	Grain Count	Mean Grain Area	Mean Height (*h*)	Elongation (*h/s*)
Side view A	1502.49 mm^2	35	42.9 mm^2	12.3 mm	3.5
Side view B	1953 mm^2	43	45.4 mm^2	13.0 mm	3.7
Considered value				12.25 mm	3.5

Validation

Figure 4-6 shows that the coarse grain CIVA model fits well with the macrographs. (More details are given in Section 8.)
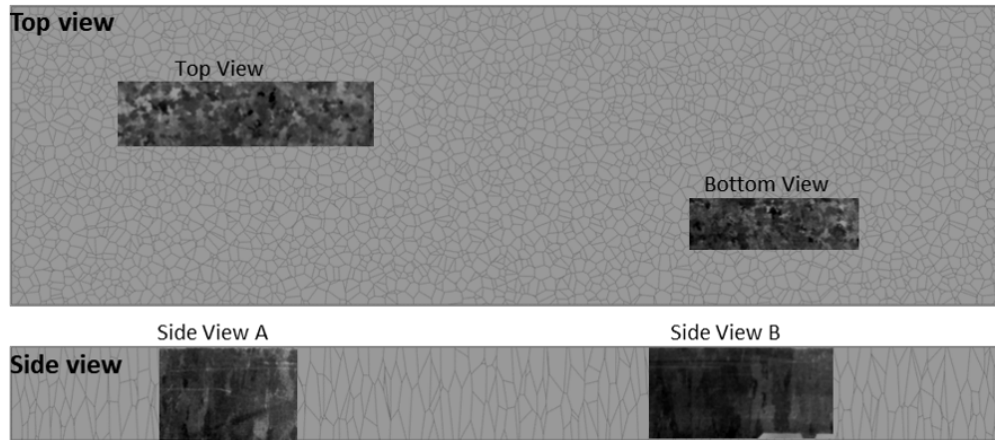
Figure 4-6
Coarse grain structure modeled by CIVA vs. scaled processed images

5
EXPERIMENTAL IMMERSION TESTING

In this section experimental data for immersion testing of J7010-4 are presented. The objective of this section is to characterize J7010-4 material properties such as nominal grain velocity and its distribution. These values will serve as initial CIVA specimen input parameters.

The study zone (Figure 5-1) was defined to ensure that the beam is only affected by the coarse grain structure—and not by geometries or flaws circled in red in Figure 5-1. The observed variations in TOF and the amplitude are both relevant characteristic values of the grain structure. The variation in amplitude and TOF are due to material variations between the coarse grains. The study zone measures 80 mm in length, 102 mm in width, and 32 mm in height. Experimental scanning covered the whole component, but CIVA analysis tools were used to crop the entire data set to an approximate study zone shown in Figure 5-1.
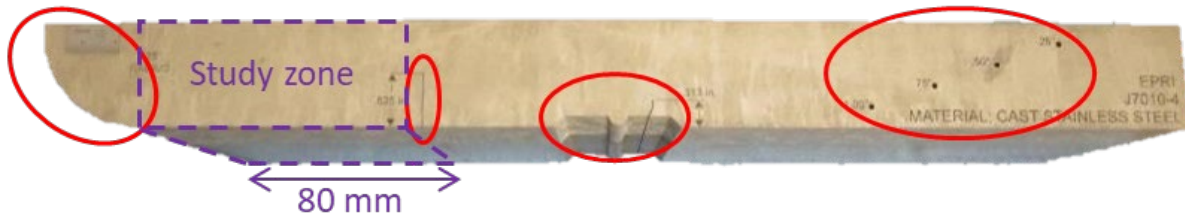
Figure 5-1
Definition of the study zone

A synchronization gate allowed an accurate TOF measurement between the surface's entry echo and bottom echo. In Figure 5-2 the red gate is set on the entry echo and the green gate is synchronized on the red one. The time signal recorded by the green gate is defined relative to the red gate's trigger. Local velocity is evaluated by measuring the TOF to the bottom echo from the green gate and is calculated knowing the component's thickness. The amplitude and the TOF were exported from CIVA to generate amplitude and TOF histograms. The amplitude plots and histograms in the following section use the SDH measurements as the reference point for 0 dB (see Appendix A).
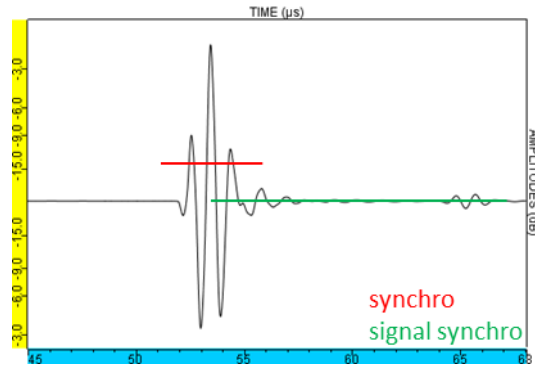
Figure 5-2
Synchronization gate

500 kHz

Figure 5-3 shows the study zone amplitude and TOF C-scans for the 500-kHz immersion probe. Due to the 500-kHz probe's large beam, the bottom echo is attenuated at the borders. The TOF C-scan shows two sharply defined zones: orange and yellow.
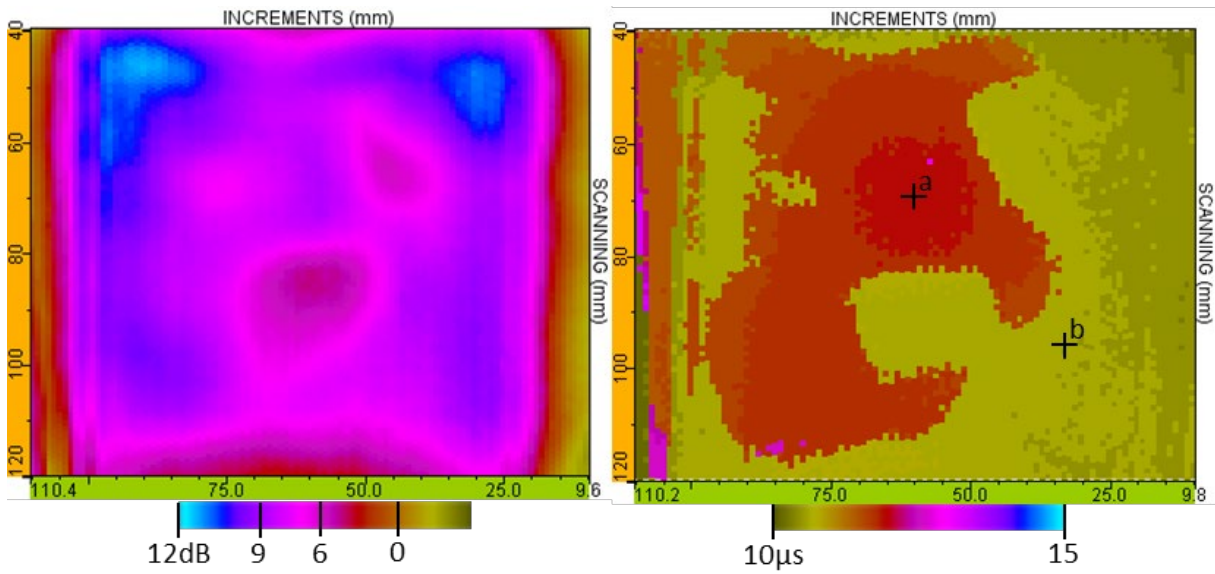
Figure 5-3
Amplitude (left) and TOF (right) C-scans in the study zone for 500-kHz immersion probe

An amplitude histogram (Figure 5-4) was calculated, and it has a nearly normal distribution with a slight left skew. A "homogenized" velocity histogram was calculated from the TOF C-scan and is shown on the right side of Figure 5-4. The homogenized velocity will be referred to throughout the report as a measured nominal or conglomerated velocity within the study zone. The homogenized velocity histogram has a bimodal distribution.
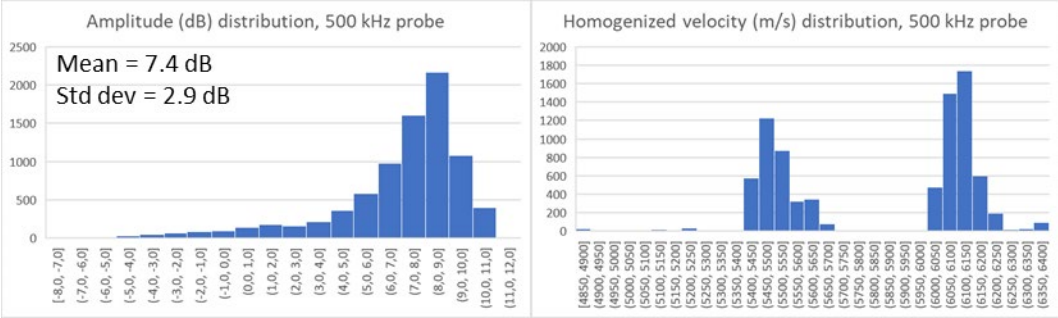
Figure 5-4
Amplitude (left) and homogenized velocity (right) histograms for 500-kHz immersion probe

Figure 5-5 shows a zoomed view of the rectified A-scans at positions *a* and *b* on the TOF C-scan (Figure 5-3). Position *a* is in the orange zone, and *b* is in the yellow zone. The difference in TOF between *a* and *b* is due to a phase change of approximately a half cycle. The TOF measurement is defined at the maximum of the rectified signal, and its time location "jumps" in half-cycle steps. These jumps are larger for lower-frequency probes and more likely to occur with narrower bandwidth (slower increase/decrease of amplitude between cycles). This explains the two distinctive peaks in the homogenized velocity histogram in Figure 5-4. This phenomenon could be addressed by applying an envelope to the A-scans, but the present study has been conducted with the rectified time-domain data. Future research could be conducted with an enveloping process of the A-scans to determine its effect on eliminating the phase dependency.
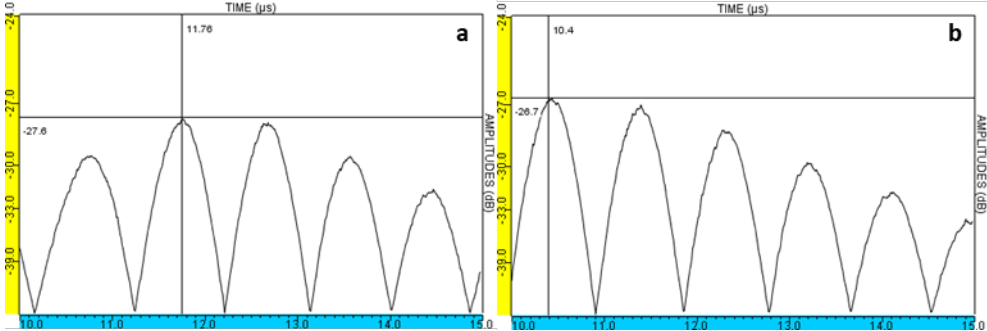
Figure 5-5
A-scan at positions *a* (left) and *b* (right) as depicted in Figure 5-3

1.0 MHz

Figure 5-6 shows the study zone amplitude and TOF C-scans for the 1-MHz immersion probe. Due to the probe's large beam, the bottom echo is attenuated at the borders. The amplitude C-scan indicates clear variations, while the TOF C-scan has much softer ones.

Both the amplitude and the homogenized velocity histograms (Figure 5-7) have a nearly normal distribution. The amplitude histogram has a slight left-skewed distribution.
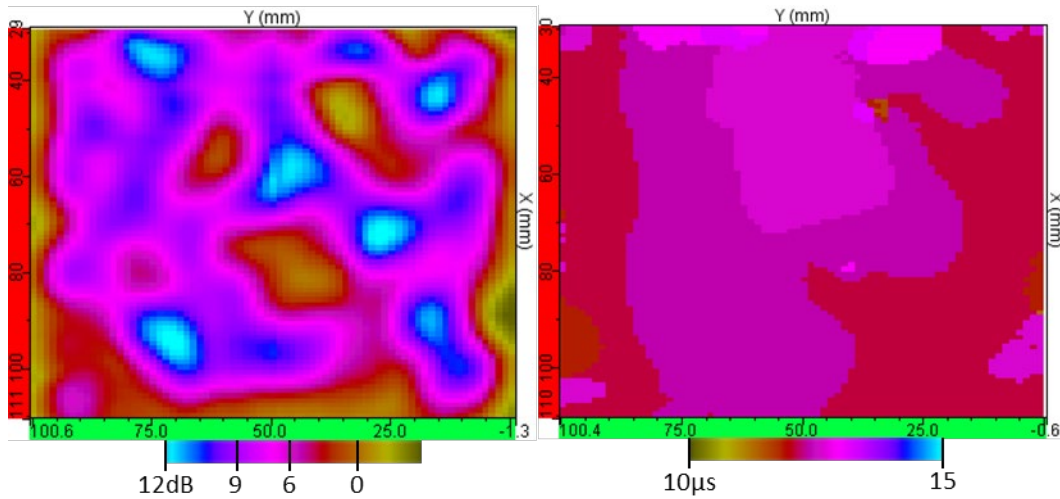
Figure 5-6
Amplitude (left) and TOF (right) C-scans in the study zone for 1.0-MHz immersion probe
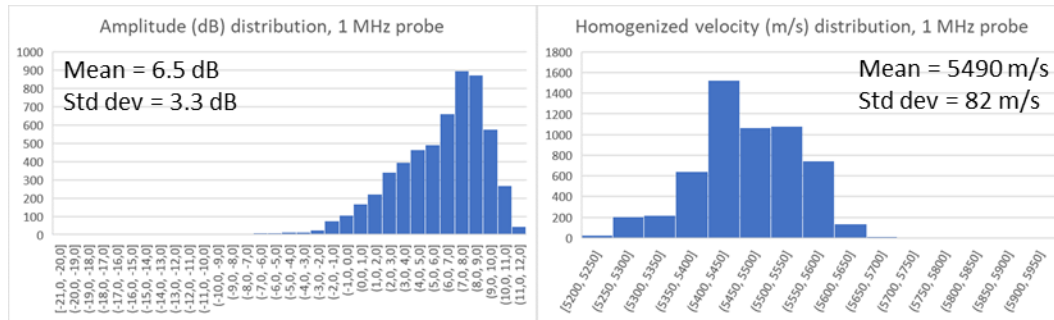
Figure 5-7
Amplitude (left) and homogenized velocity (right) histograms for 1-MHz immersion probe

2.25 MHz

Figure 5-8 shows the study zone amplitude and TOF C-scans for the 2.25-MHz immersion probe. The probe's narrower beam size makes the bottom echo less affected by the borders than the previous probes. Both the amplitude and TOF C-scans show clear variations across the scan surface.

Both the amplitude and the homogenized velocity histograms (Figure 5-9) have a nearly normal distribution. The amplitude standard deviation for the 2.25 MHz is the highest of the three inspection frequencies used because of the 2.25-MHz sensitivity with the grain structure.
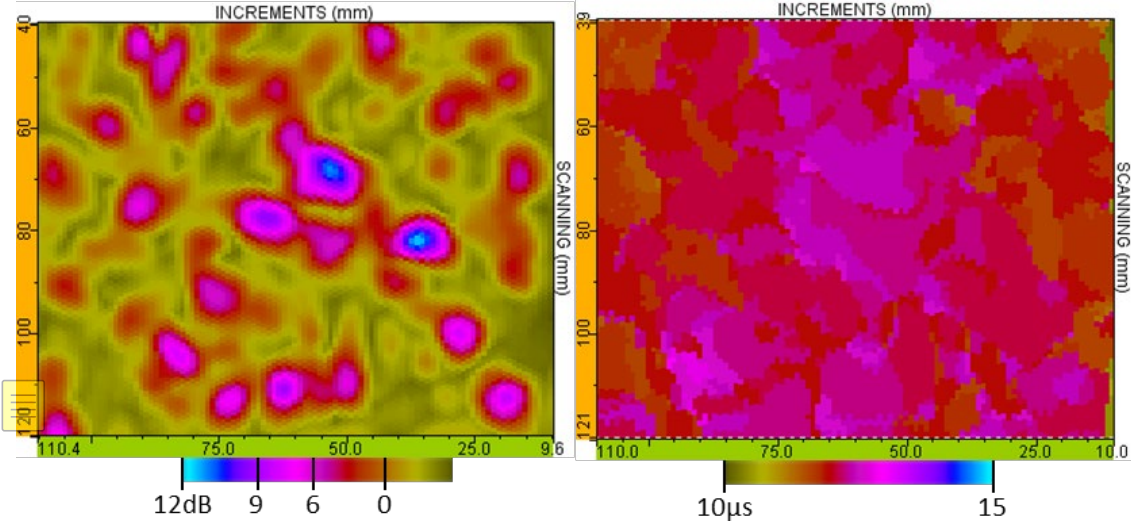
Figure 5-8
Amplitude (left) and TOF (right) C-scans in the study zone for 2.25-MHz immersion probe
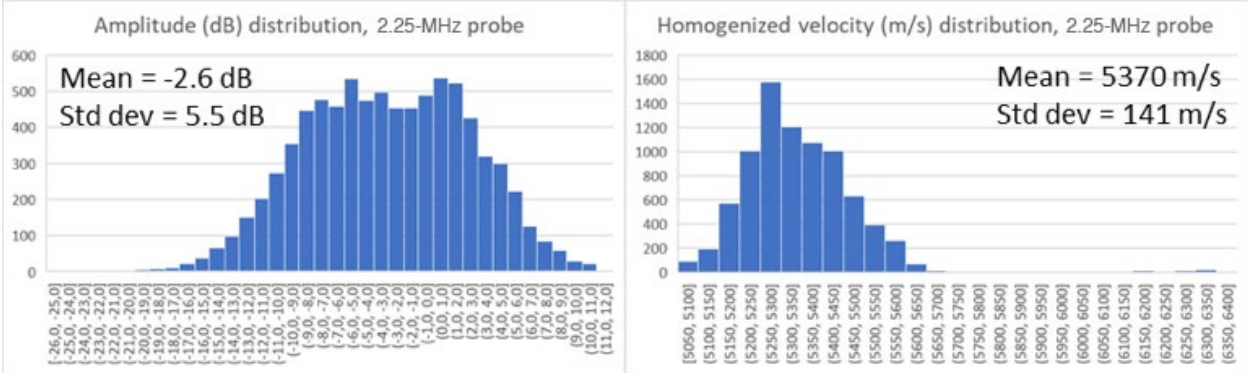
Figure 5-9
Amplitude (left) and homogenized velocity (right) histograms for 2.25-MHz immersion probe

6
DEVELOPING CIVA COARSE GRAIN MODELS

In this section, CIVA simulations are developed for coarse grain structures in immersion testing. The objectives of this section are to accomplish the following:

- Provide an introduction and description of relevant CIVA settings when developing coarse grain models.

- Systematically study and determine CIVA accuracy and sensitivity zone settings for conducting simulations pertinent to this research. This is necessary to ensure high-quality simulation results while minimizing computation time.

Modeling Coarse Grain Structures

CIVA is capable of simulating coarse grain structures with its semi-analytical approach [7] by splitting a component in multiple grains having their own material characteristics. The geometrical cell splits are based on Voronoï diagrams [8]. In the 2017 SP1 version of CIVA, this option is available for flat and cylindrical components.

Figure 6-1 shows the CIVA panels to describe a coarse grain specimen for a flat component. The cells' velocities for L-waves and transverse waves (T-waves) are defined with a uniform distribution. Again, T-waves are ignored in this study. The velocity distribution is defined according to the diagram in Figure 6-1; where, V_m is the average velocity and ΔV_x the dispersion defined in percent of V_m.
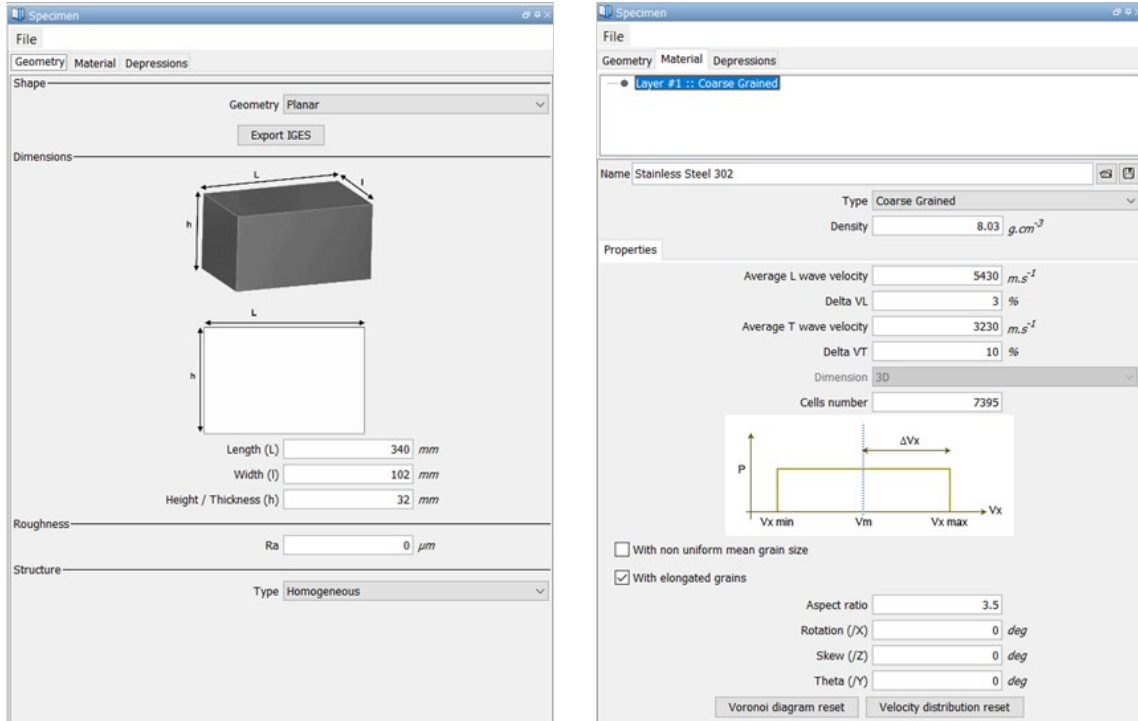
Figure 6-1
Coarse grain component definition in CIVA

CIVA parameter *Cells number* is the number of grains in the component. It can be evaluated by C_{vol}/G_{vol}, where C_{vol} is the component volume and G_{vol} is the mean grain volume. The component volume is calculated as follows: $L \times l \times h$ (Figure 6-1). The mean grain volume is calculated from grain-size measurements as follow: $s \times s \times h$; where s is 3.5 mm and h is 12.25 mm (see Section 4).

The CIVA option *With non-uniform mean grain size* allows a user to define grain-size variations such as multi-banded grain structures. The *With elongated grains* option allows a user to define grains such as the columnar grain structures that are used within this study. The buttons *Voronoï diagram reset* and *Velocity distribution reset* are generating new random sets of cells with their respective velocities. Changing the *Cells number* or the component's dimensions resets the Voronoï diagram. A given model's Voronoï diagram and respective velocity distribution can be reused if the aforementioned buttons or parameters are not modified or clicked.

As part of this study, it was important to investigate CIVA computation parameters that minimize computation time while maintaining high-quality simulated results. These specific CIVA computation parameters are as follows (see Figure 6-2):

- *Field accuracy*—increasing the field precision refines the probe mesh [7] to improve the computed ultrasonic field but increases the computation time.

- *Defect accuracy*—increasing the defect precision refines the flaw mesh [7] to improve the computed beam-defect interaction but increases the computation time.

- *Sensitivity zone*—the sensitivity zone is a three-dimensional box outside of which no interaction with flaws and geometric features is performed, which could save computation time when flaws and geometric features are out of the probe's range.
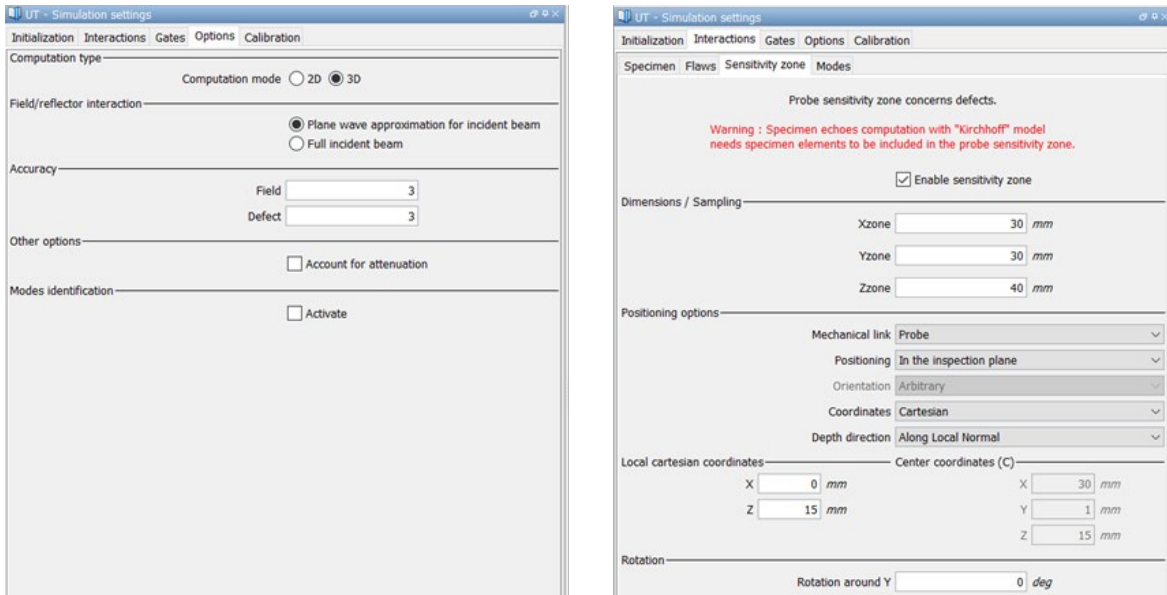
Figure 6-2
CIVA computation parameters

Initial Model Inputs Based on Experimental Data

J7010-4 immersion data, as presented in Section 5, provided initial CIVA component definitions. In this section, we discuss how the experimental homogenized velocity and velocity distributions were tested in CIVA models to determine how well they match the experimental immersion data. These baseline models were used to determine how well the material properties have been characterized for J7010-4 and to help determine the next steps for model refinement.

Table 6-1 reports the measurements performed from the immersion testing. The mean, minimum, and maximum of the homogenized velocities were considered for the whole set of data. The grain velocity distribution would be considered as normal, and the minimum and maximum measurements help to avoid extreme values, where σ is the standard deviation. As described in Section 5, the CIVA parameter *Average L-wave velocity* is initialized at V_m = 5,430 m/s.

Table 6-1
Velocity dispersion measurements from experimental data

		500 kHz	**1 MHz**	**2.25 MHz**
Homogenized velocities values	Mean	5874 m/s	5490 m/s	5370 m/s
	Min	4851 m/s (−18%)	5178 m/s (−5%)	5027 m/s (−6%)
	Max	6400 m/s (+9%)	5926 m/s (+8%)	6400 m/s (+19%)
Gaussian limits	Min	5400 m/s (−8%)	5250 m/s (−4%)	5050 m/s (−6%)
	Max	6250 m/s (+6%)	5650 m/s (+3%)	5650 m/s (+5%)
	σ	317 m/s (±5%)	82 m/s (±1.5%)	141 m/s (±3%)

Beam intensity plots were simulated for each immersion probe tested and are displayed in Figure 6-3 when considering a homogeneous material with $V_m = 5430$ m/s. The field computation step was chosen at approximatively $\lambda/10$, with λ being the wavelength; thus, the field computation steps were set to 1 mm for 500 kHz, 0.5 mm for 1 MHz, and 0.25 mm for 2.25 MHz. The −12-dB-beam width was measured in the transmission/reception condition at 20 mm, 18 mm, and 12 mm.
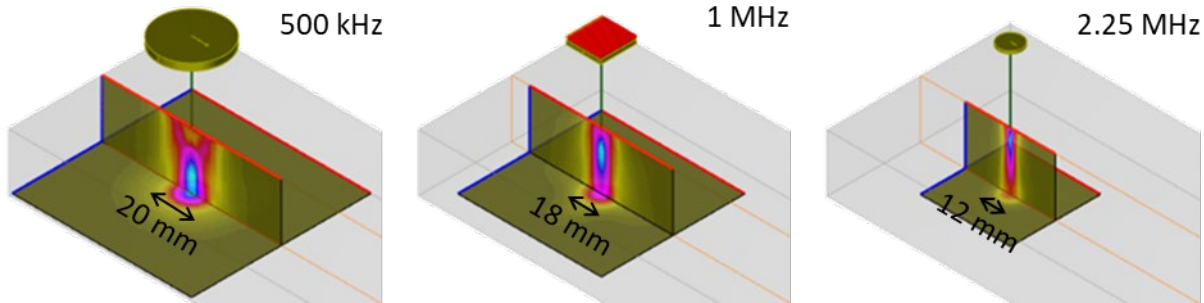
Figure 6-3
Probes' beam (transmit and receive [T/R]) in homogeneous material

Due to CIVA's flat plate and cylindrical geometrical limitations of coarse grain models, the component was defined with a flat geometry of J7010-4 dimensions (see Figure 2-2).

The *Average L-wave velocity* and *Delta VL* in the grains were set based on the experimental homogenized velocities distribution observed from the bottom echo; where *Delta VL* is the random velocity values from a uniform distribution, the *Average L-wave velocity* was set to 5430 m/s. To define *Delta VL*, three approaches could be considered from Table 6-1: choose the dispersion of minimum/maximum raw values, of minimum/maximum Gaussian, or the standard deviation. The last one was chosen, and the 3% value from the 2.25-MHz probe was taken for the initial setup of all inspection frequencies. Figure 6-4 overlaps the normal distribution and the uniform distribution between ±σ to compare their probability densities.
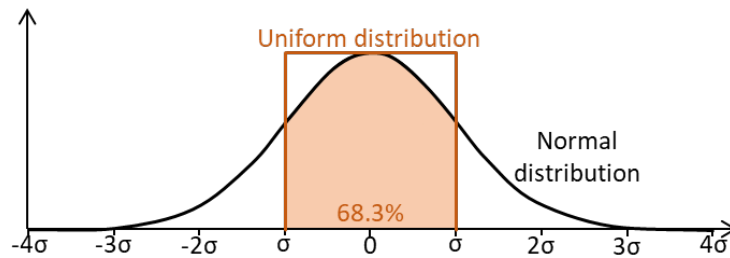
Figure 6-4
Normal vs. uniform distribution

T-wave (average and delta) were left at default values since T-wave was not used; computations were set to consider L-waves only. *Cells number* was such that $C_{vol}/G_{vol} = (340 \times 102 \times 32)/(3.5 \times 3.5 \times 12.25) = 7395$ cells. The *non-uniform mean grain size* option was not selected, and the grain elongation was taken from Table 4-2.

Beam simulations with a field precision of 1 were initially conducted using parameters given in Table 6-2, and their results are shown in Figure 6-5. Transmission/reception simulations are displayed in Figure 6-5. In Figure 6-5, the beam simulations are shown for a qualitative assessment of scattering effects as well as image smoothness. The vertical axis is specimen depth, and the horizontal axis is lateral dispersion of the sound field. All beams were significantly affected by the grain structure, and the lack of field precision was clearly observed for the 500-kHz probe.

Table 6-2
Initial grain settings in CIVA

Average L-Wave Velocity	Delta VL	Cells Number	Grain Elongation
5,430 m/s	3%	7,395	3.5
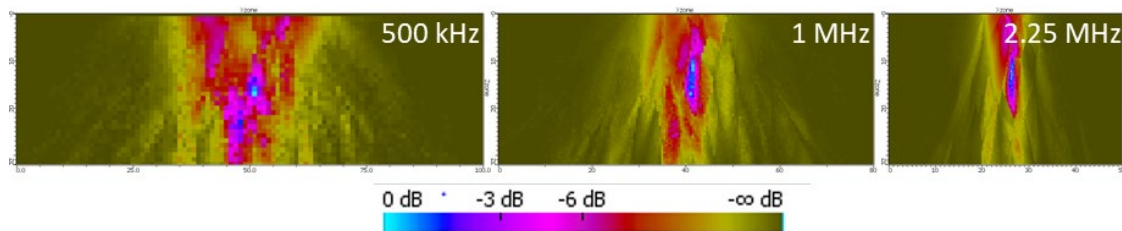
Figure 6-5
Probes' beam (T/R) with initial settings where the vertical axis is specimen depth and the horizontal axis is lateral dispersion of the sound field. The length scale is in millimeters.

Influence of Accuracy and Sensitivity Zone Settings

This section aims at defining the computation settings to ensure the suitability of the simulated data with minimum computation time.

Field Precision

The semi-analytic model of CIVA computes the field transmitted at a defined point by summing the contribution from each probe's surface mesh. The contributions are computed using the so-called pencil method [7]. The field precision parameter influences the size of the probe's surface mesh. The higher the field precision is, the smaller the surface mesh and the larger the number of mesh points. To summarize, a higher precision value will give more accurate results, but it increases the computation time.

The influence of the field precision on the computation of the beam is displayed for the three immersion probes in Figure 6-6. Field precision of 3 is chosen to guarantee correct computing. Increasing this value significantly increases the computation time with very few improvements in the result.
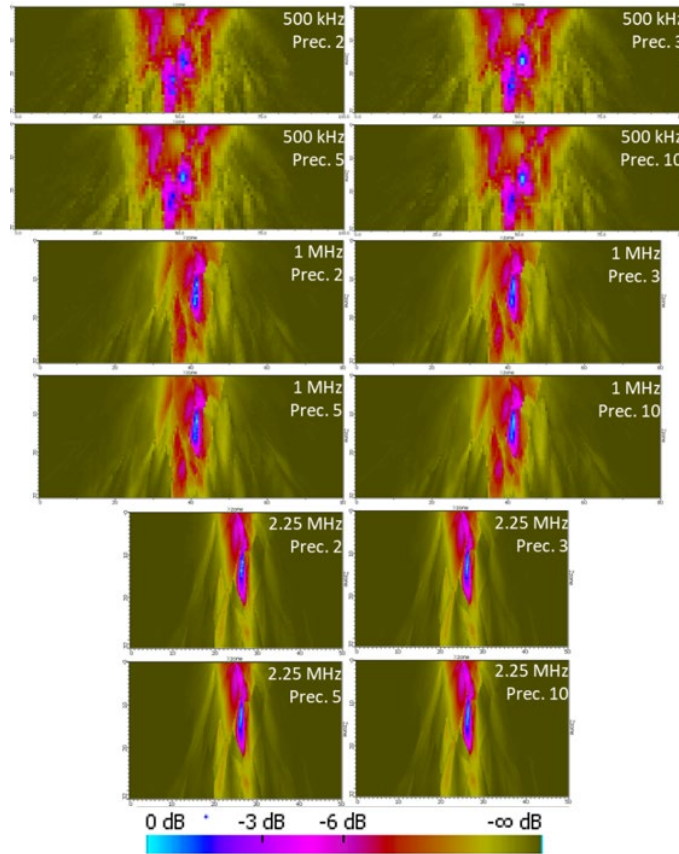
Figure 6-6
Field precision impact for the immersion probes where the vertical axis is specimen depth and the horizontal axis is lateral dispersion of the sound field. The length scale is in millimeters.

Defect Precision

The Kirchhoff model of CIVA computes the echo of a geometric feature by summing the contribution of each surface mesh of the feature [7]. The defect precision parameter influences the size of the geometry's surface mesh. The higher the defect precision is, the finer the component's surface mesh and the larger the number of points in this mesh. To summarize, a higher precision value will give more accurate results, but it increases the computation time.

The influence of the defect precision is evaluated (Figure 6-7) based on the responses from the bottom face echo for random positions on the component. Figure 6-7 displays the maximum amplitude of the signal at five different B-scan positions, and each position was more than 50 mm apart. Using such a small number of steps was aimed at limiting the computation time (see Appendix C). As the precision is increased, it's expected that the amplitude measurements will begin to stabilize. Therefore, for the purposes of this study, once an error of less than 1dB,

in reference to a defect precision of 10, was reached, convergence was considered achieved. The 2.25-MHz probe shows a convergence of results (error < 1 dB compared to precision 10) from a precision of 3. The 1-MHz probe shows a convergence of results from a precision of 5. Since the 500-kHz probe does not show convergence, a precision of 10 was considered. Also, for this study the 500-kHz probe produced a wavelength comparable to the average height of the grains.
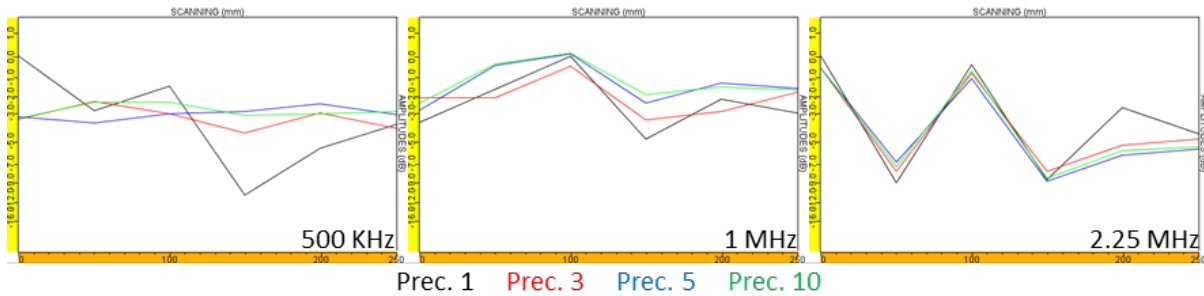
Figure 6-7
Defect precision impact for the immersion probes

Sensitivity Zone

The study zone, as described in Section 5, is approximately 80 × 100 mm with 1-mm steps, which makes approximately 8000 positions (or A-scans). Considering the computation time for 5 positions, scaling up to 8000 leads to a prohibitive amount of time. The use of the sensitivity zone allows reducing the computation effort by limiting the computation to the bottom face response. CIVA will compute only the response of the intersection off the surface and the sensitivity zone for geometry echoes. The compromise is to reduce it to the response's maximum value to save computation time, while sampling sufficiently to simulate an accurate echo.

Keeping the same B-scan configuration, different sensitivity zone sizes are compared in Figure 6-8. A good match (mean error < 0.5 dB across all five positions) is observed for 60 × 60 mm, 40 × 40 mm, and 30 × 30 mm.
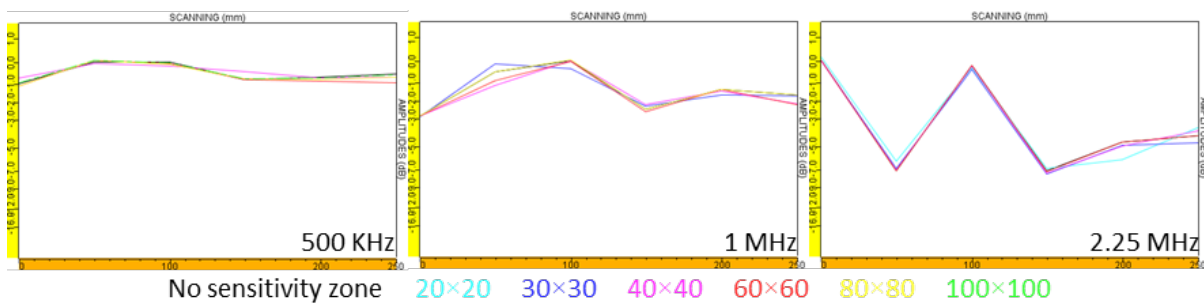
Figure 6-8
Sensitivity zone size impact

Final Accuracy and Sensitivity Zone Settings

The computation parameter study led to the settings defined in Table 6-3 for each immersion probe.

Table 6-3
Computation settings

Probe	Field Precision	Defect Precision	Sensitivity Zone
500 kHz	3	10	60 × 60 mm
1 MHz	3	5	40 × 40 mm
2.25 MHz	3	3	30 × 30 mm

7
SIMULATED IMMERSION TESTING

In this section, we discuss how CIVA immersion simulations were conducted and compared against experimental results from Section 5. The objectives of the work described in this section were as follows:

- Perform initial CIVA simulations using specimen material properties measured during work discussed in Sections 4 and 5 while using the computation parameters from Section 6. The results from these models acted as a baseline assessment for specimen input parameters.

- Conduct a parametric study on CIVA input parameters related to coarse grain models such as grain velocity, velocity distribution, grain size, and grain elongation. Studying these parameters allowed for insight during a manual optimization of the final CIVA model.

- Perform final CIVA simulations for immersion testing and a comparison with experimental results. The final CIVA input parameters were used for the contact problem simulations described in Section 8.

Initial Simulations

This section compares the immersion testing simulations, based on initial grain modeling inputs discussed in Sections 4 and 5 while using the chosen computation settings from Section 6, to the experimental data presented in Section 5. The comparisons are based on amplitude and TOF C-scans, and on amplitude and velocity histograms.

500 kHz

Figure 7-1 displays amplitude and TOF C-scans for both experimental and simulated data. The amplitudes show an overall match, with less accentuated variation for the simulations. The TOF C-scan shows a greater discrepancy; the experimental phase shift is not as prevalent in the simulation. Further research is needed to characterize this discrepancy; however, the simulated signal in comparison to the experimental signal, and its bandwidth, may have an influence.
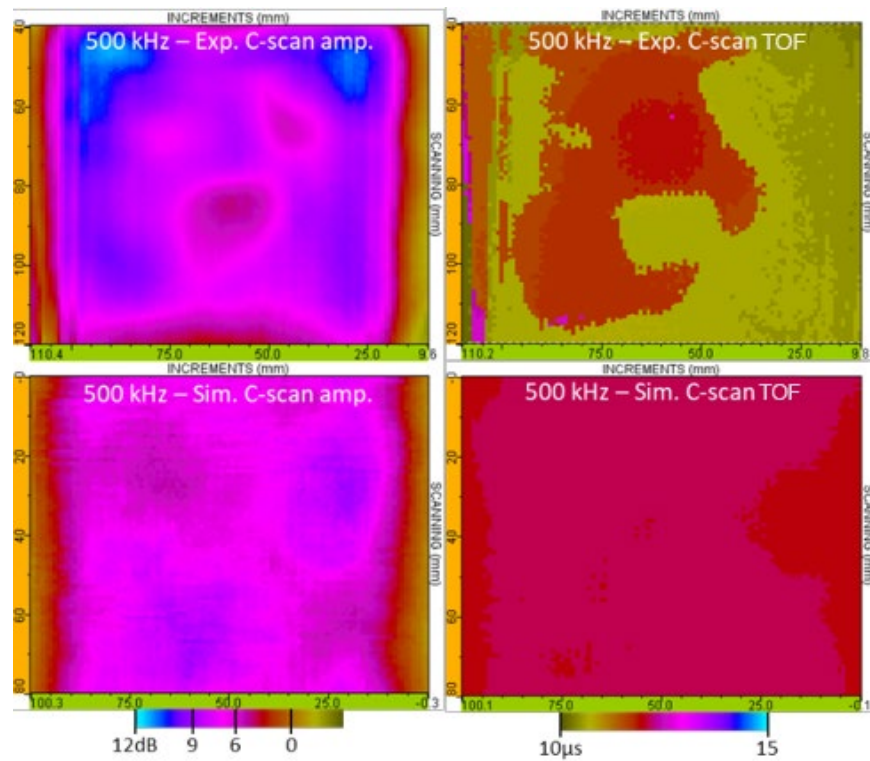
Figure 7-1
C-scans comparing the simulation with initial settings vs. experimental data at 500 kHz

Figure 7-2 displays amplitude and homogenized velocity histograms for both experimental and simulated data. As per the C-scans, the amplitude histograms match decently with a mean value error of 1.1 dB; but the experimental homogenized velocity histogram has two peaks, while the simulation has only one narrower peak.
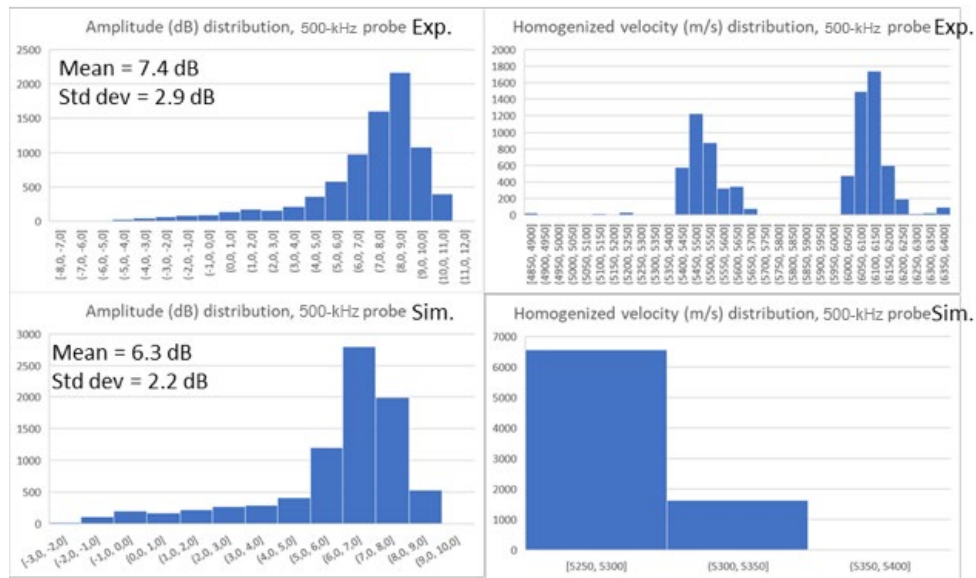
Figure 7-2
Histogram comparison of the simulation with initial settings vs. experimental data at 500 kHz

1 MHz

Figure 7-3 displays amplitude and TOF C-scans for both experimental and simulated data. The amplitudes show an overall match, with slightly less accentuated variations in the simulated results. The TOF C-scan shows much less variation for the simulation than for the experiment.
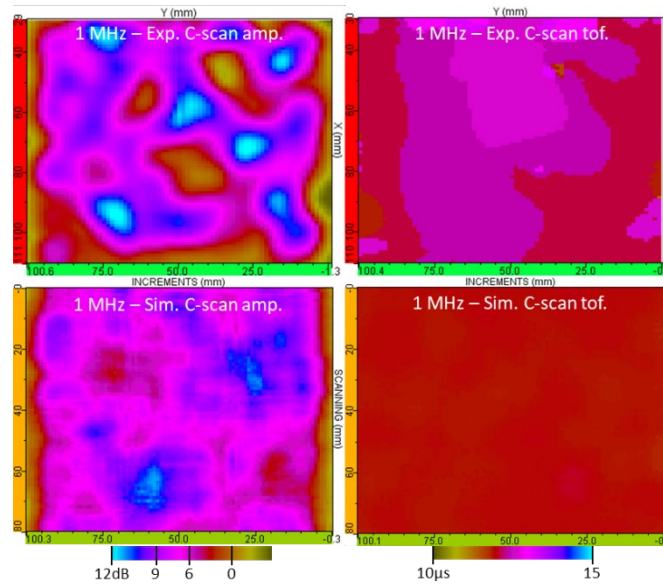
Figure 7-3
C-scans comparing the simulation with initial settings vs. experimental data at 1 MHz

Figure 7-4 displays amplitude and homogenized velocity histograms for both experimental and simulated data. As per the C-scans, the amplitude histograms match decently, but the homogenized velocity histogram is significantly narrower in simulation than in experiment.
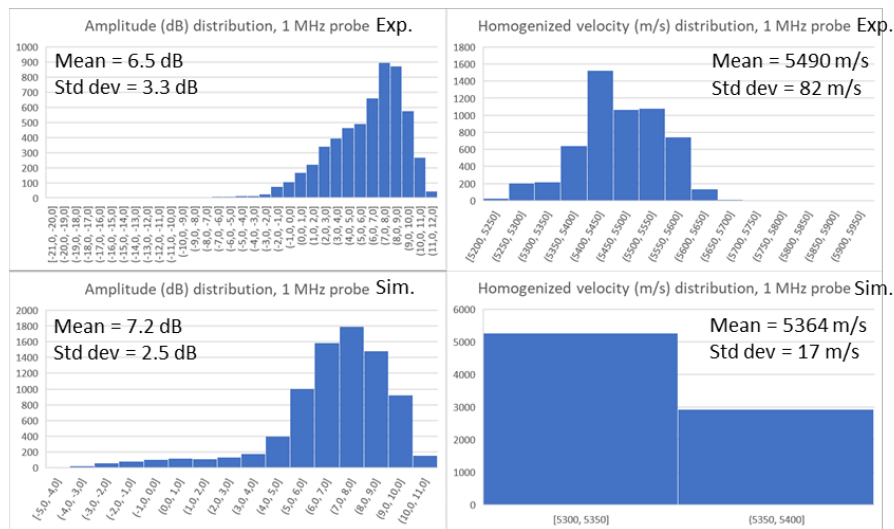
Figure 7-4
Histogram comparison of the simulation with initial settings vs. experimental data at 1 MHz

2.25 MHz

Figure 7-5 displays amplitude and TOF C-scans for both experimental and simulated data. The amplitudes show an overall match, with slightly fewer accentuated variations in simulated results. The TOF scans show fewer variations for the simulation than for the experiment.
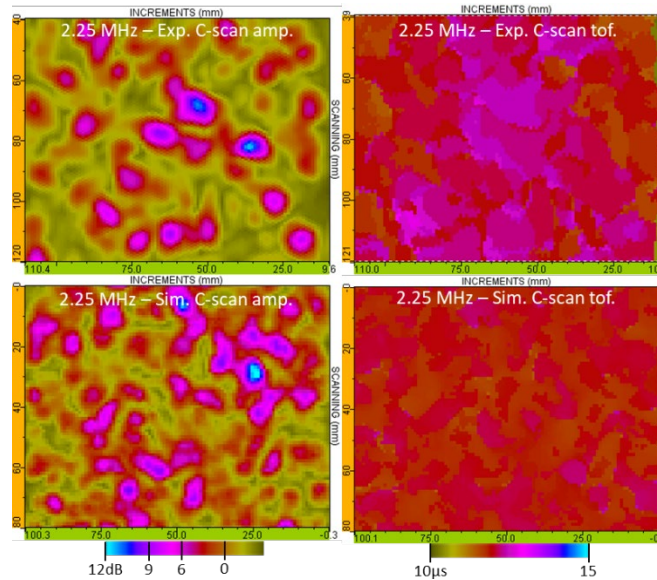
Figure 7-5
C-scans comparing the simulation with initial settings vs. experimental data at 2.25 MHz

Figure 7-6 displays amplitude and homogenized velocity histograms for both experimental and simulated data. As per the C-scans, the amplitude histograms match decently with the simulation, having a sharper peak in comparison with the experiment, which has a plateau. The homogenized velocity histogram is narrower in simulation than in experiment.
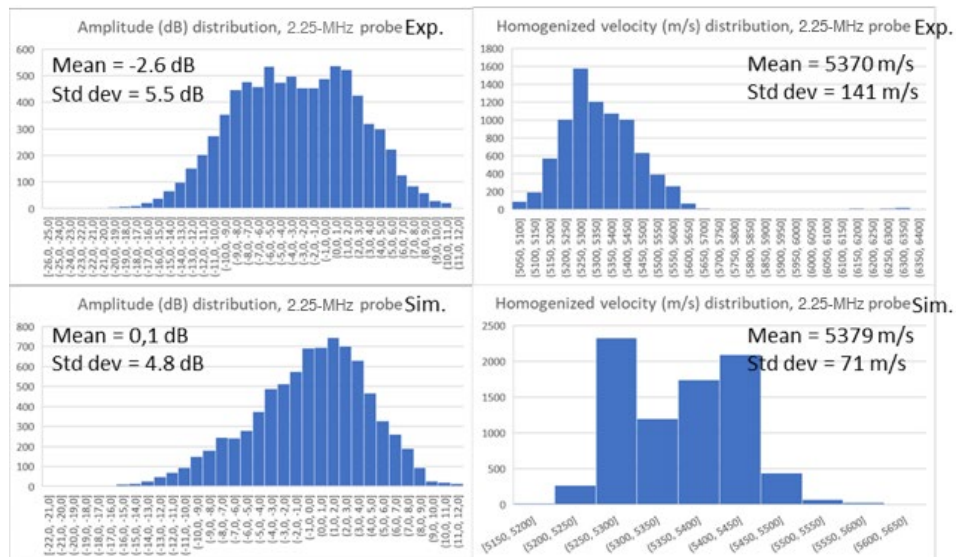
Figure 7-6
Histogram comparison of the simulation with initial settings vs. experimental data at 2.25 MHz

Parametric Study of Specimen Properties

The parametric study presented in this section was aimed at improving CIVA settings for the coarse grain description to better match the immersion experimental data, starting from the initial values determined from observations. This study was performed with the 2.25-MHz probe only because it is the more sensitive frequency studied for the coarse grain structure due to its higher frequency and narrower beam. The simulated scan was reduced to a 50 × 50-mm area (with a 1-mm step for both axes). This saved computation time, while minimally affecting the statistical fidelity of the results. When inspecting CASS materials, a lower frequency, such as 0.5–1 MHz, would likely be used; however, in this section, the objective was not to inspect the material for indications, but to use the 2.25-MHz probe to better evaluate material properties.

The influence of four parameters (average velocity, velocity dispersion, grain size, and grain elongation) on the indicators (amplitude and homogenized velocity mean and standard deviation) were observed near the initial settings. The initial settings were manually refined, based on the parameters' influence, to best match the experimental values.

Average Velocity

The influence of average grain velocity (CIVA parameter—*Average L-wave velocity*) is observed in red on Figure 7-7 for three *Average L-wave velocity* values—5330 m/s, 5430 m/s, and 5530 m/s. The experimental values are displayed with black dashed lines, and the initial setting is marked in green. Average velocity of grains has an influence on the homogenized velocity only, amplitude (mean and standard deviation) and velocity standard deviation are not affected.
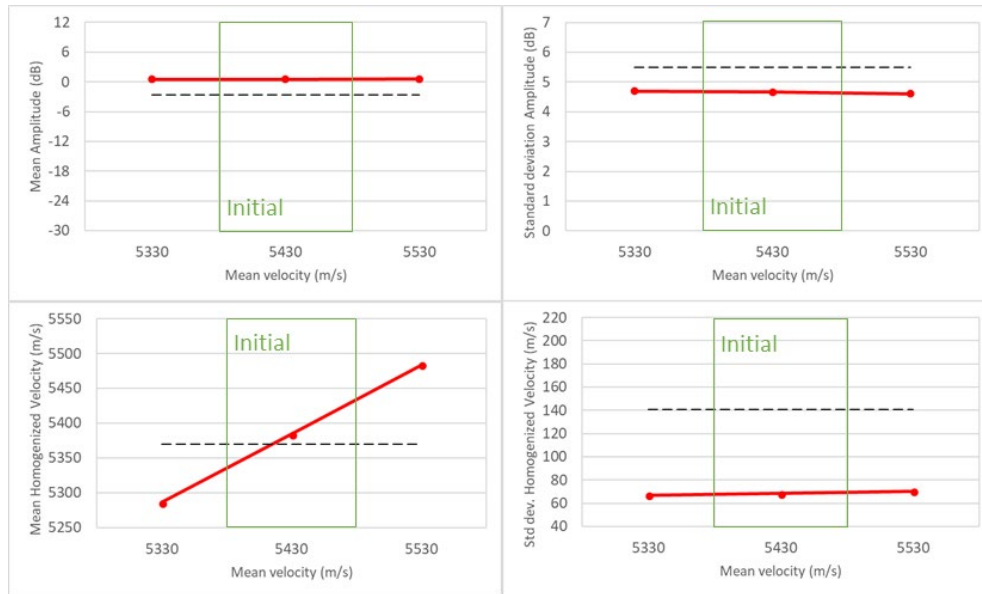
Figure 7-7
Average grain velocity study

Velocity Dispersion

The influence of the velocity dispersion of L-waves (CIVA parameter—*Delta VL*) is observed in red on Figure 7-8 for five *Delta VL* values—1%, 2%, 5%, and 10%. The experimental values are displayed with black dashed lines, and the initial setting is marked in green. This parameter affects the four observed indicators. Increasing grain velocity dispersion decreases the mean amplitude but increases the amplitude standard deviation up to 5%, staying stable above. The mean homogenized velocity also slightly decreases, while the homogenized velocity standard deviation obviously increases.
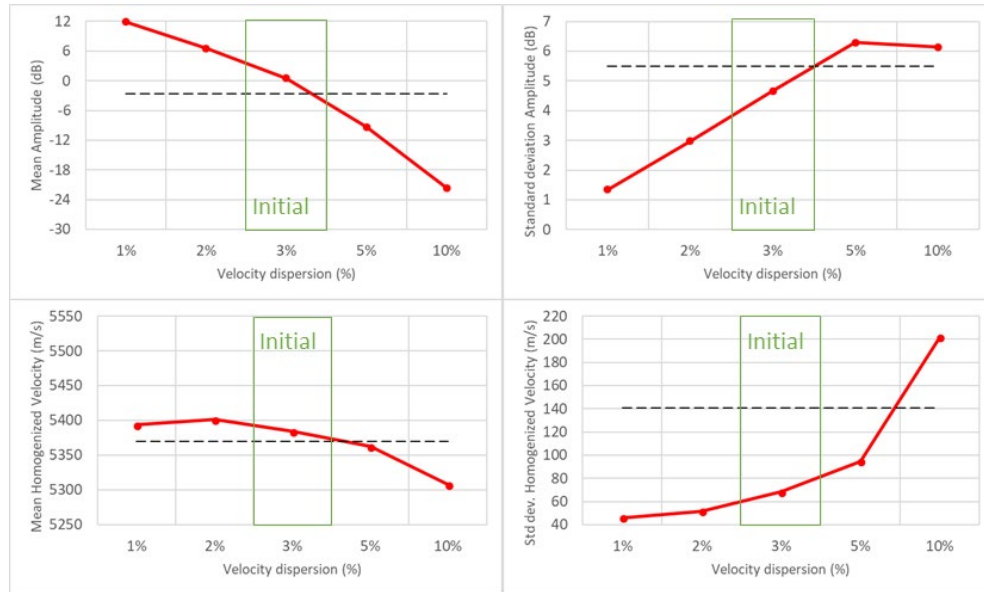
Figure 7-8
Velocity dispersion study

Grain Cross-Sectional Size

The influence of the grain's cross-sectional size (CIVA parameter—*Cells number* as a function of grain cross-sectional size, as defined in Section 4) is observed in red on Figure 7-9 for four values. The CIVA parameter *Aspect ratio* was held constant at 3.5 for this study. *Cells number* is defined for each case according to Table 7-1. The experimental values are displayed with black dashed lines, and the initial setting is marked in green. Increasing the cross-sectional size of a grain clearly affects the mean amplitude and standard deviation and the homogenized velocity standard deviation. The mean homogenized velocity is only slightly affected.

Table 7-1
Evaluation of *Cells number* depending on the cross-sectional grain size

Cross-Sectional Grain Size	Surface	Elongation	Grain Volume	Comp. Volume	*Cells Number*
1.50 mm	2.25 mm^2	3.50	11.81 mm^3	1,109,760 mm^3	**93,948**
2.50 mm	6.25 mm^2	3.50	54.69 mm^3	1,109,760 mm^3	**20,293**
4.50 mm	20.25 mm^2	3.50	318.94 mm^3	1,109,760 mm^3	**3,480**
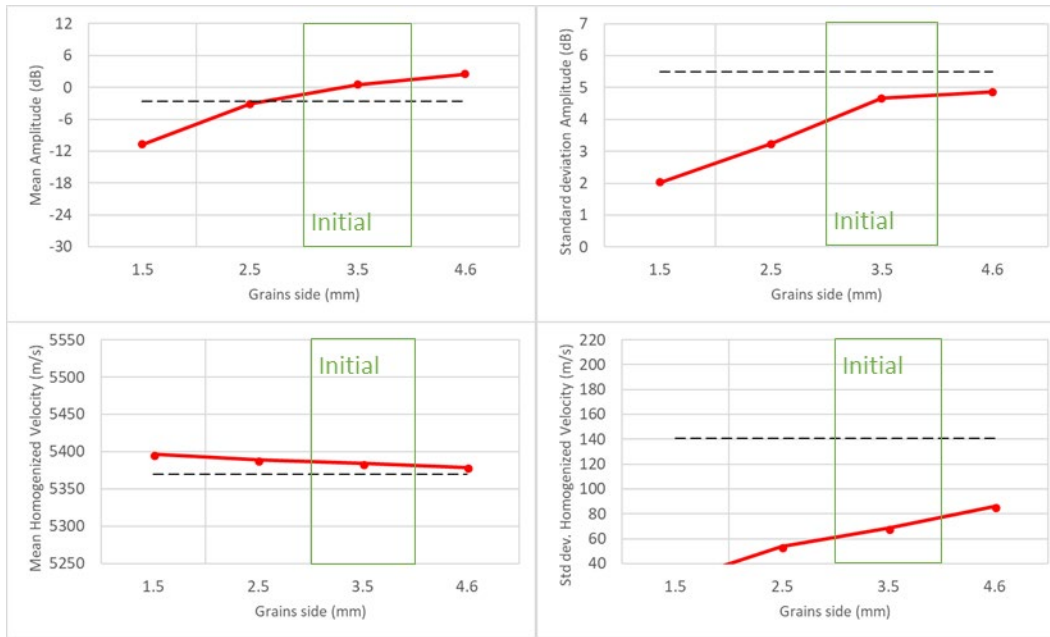
Figure 7-9
Grain cross-sectional size study

Grain Elongation

The influence of the grain elongation (CIVA parameters—*Cells number* and *Aspect ratio* as a function of elongation) is observed in red on Figure 7-10 for four operator values. The *Cells number* and *Aspect ratio* are defined for each case according to Table 7-2. The experimental values are displayed with black dashed lines, and the initial setting is marked in green. Increasing the grain elongation increases both amplitude and homogenized velocity standard deviations but decreases the mean amplitude. The measured mean homogenized velocity is only slightly affected.

Table 7-2
Evaluation of the Cells number depending on grain elongation

Side	Grain Surface	Elongation (*Aspect Ratio*)	Grain Volume	Comp. Volume	*Cells Number*
3.50 mm	12.25 mm^2	**1.50**	64.31 mm^3	1,109,760 mm^3	**17,256**
3.50 mm	12.25 mm^2	**2.50**	107.19 mm^3	1,109,760 mm^3	**10,353**
3.50 mm	12.25 mm^2	**4.50**	192.94 mm^3	1,109,760 mm^3	**5,752**
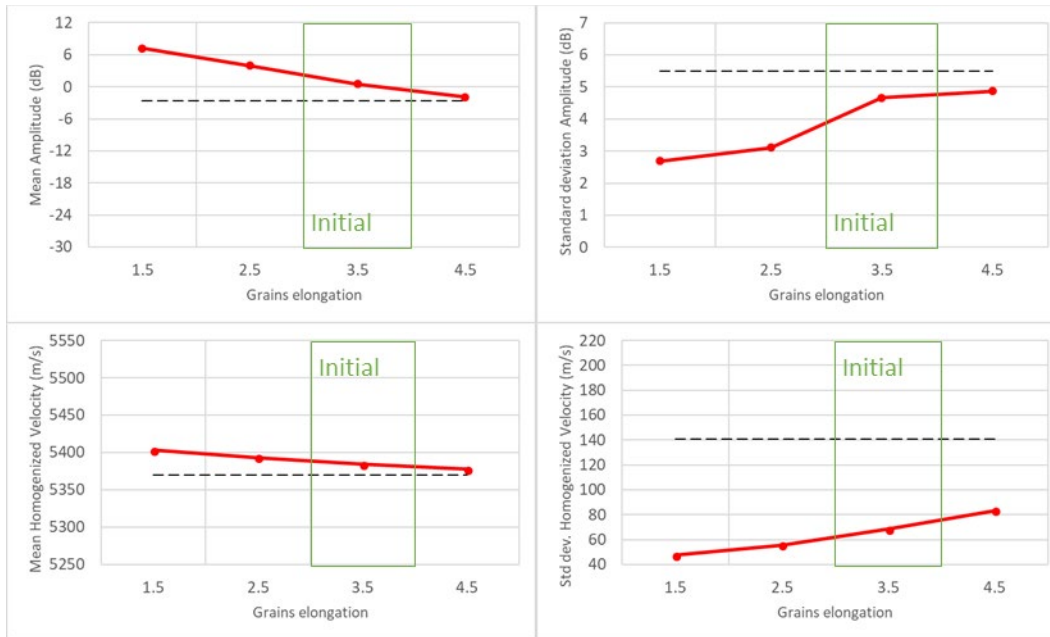
Figure 7-10
Grain elongation study

Manual Optimization of Specimen Properties

In this section, the initial settings for CIVA parameters *Delta VL*, *Cells number*, and *Aspect ratio* were manually refined using knowledge from the parametric study to best match the experimental values. Figure 7-11 shows the indicators for six tested solutions whose parameters are listed in Table 7-3. *Average L-wave velocity* was held constant at 5430 m/s for all tested solutions, and grain cross-sectional size was 4.5 mm. *Delta VL*, *Cells number*, and *Aspect ratio* were less quantifiable from experimental measurements, and they have an obvious influence, as shown in the parametric study, and are the parameters used for model refinement.
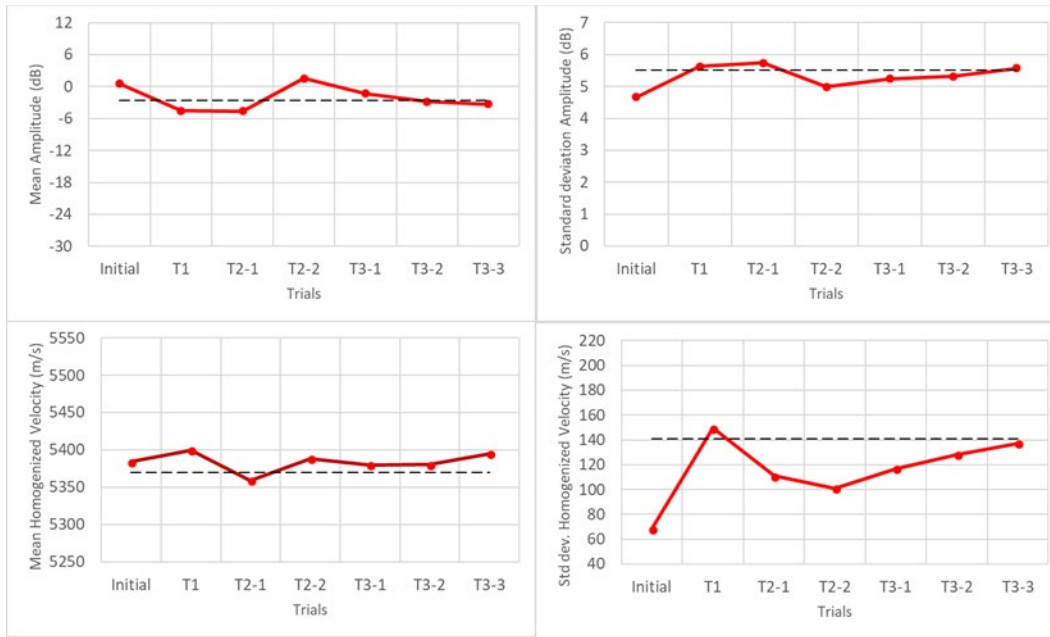
Figure 7-11
Manual study of CIVA input parameters

Table 7-3
Trials configuration for the manual study

Trial	CIVA Parameters		
	Delta VL	**Aspect Ratio**	**Cells Number**
Initial	3%	3.5	7395
T1	5 %	4.5	2706
T2-1	5 %	3.5	3408
T2-2	3 %	4.5	2706
T3-1	4 %	4	3045
T3-2	4.5 %	4	3045
T3-3	**4.5 %**	**4.5**	**2706**

The parametric study allowed the proposal for the first trial T1 by using the following qualitative approach:

- The reduction of the mean amplitude was predicted to be due mainly to an increase in the grain's velocity distribution. The reduction of mean amplitude is also attributed to an increase in grain elongation and grain cross-sectional area.

- The increase of the amplitude standard deviation was forecast to be mainly due to the velocity dispersion increase.

- The upholding of the mean homogenized velocity was forecast because of the weak influence of the parameters on this indicator.

- The significant increase of the homogenized velocity standard deviation was forecast with large contribution of all three parameters.

T1 showed a clear improvement of the amplitude and homogenized velocity standard deviations that were even overestimated. The amplitude passed from overestimated to underestimated with the same error. The second set of two trials, T2-1 and T2-2, allowed a check of the influence and the need to increase, the velocity dispersion and the grain elongation, respectively. Both confirmed their important contribution to the homogenized velocity standard deviation. The last set of trials, T3-1, T3-2, and T3-3, were to fine-tune different parameters. T3-3 showed a great correlation with experimental data and was chosen as the best coarse grain CIVA setting for the J7010-4 component. Note that the optimization methodology taken within this section could be performed in other manners, such as applying mathematical optimization techniques or selecting other variables and their respective magnitudes. The results reached within this section illustrated a process that can be taken by the user to achieve results they determine as satisfactory for their application.

Evaluation of Specimen Properties

The final configuration settings were evaluated first by applying several random sets of cell distributions and velocities attached to each cell, and second, by comparing the simulated results for the three immersion probes in the study zone with the experimental data.

Cells and Velocity Draws

Figure 7-12 compares the indicators for the five draws (D1 to D5) of Voronoï cells' generation and velocity of cells when using the 2.25-MHz probe. D1 to D5 used parameters from T3-3.

The mean amplitude varies 2.2 dB around the experimental value. The amplitude standard deviation varies 2.2 dB around the experimental value, while being slightly shifted above. The mean homogenized velocity varies 64 m/s around the experimental value and is slightly shifted above. The homogenized velocity standard deviation varies 27 m/s below the experimental value.

These results show the importance of the variability due to the random statistics of the Voronoï cells.
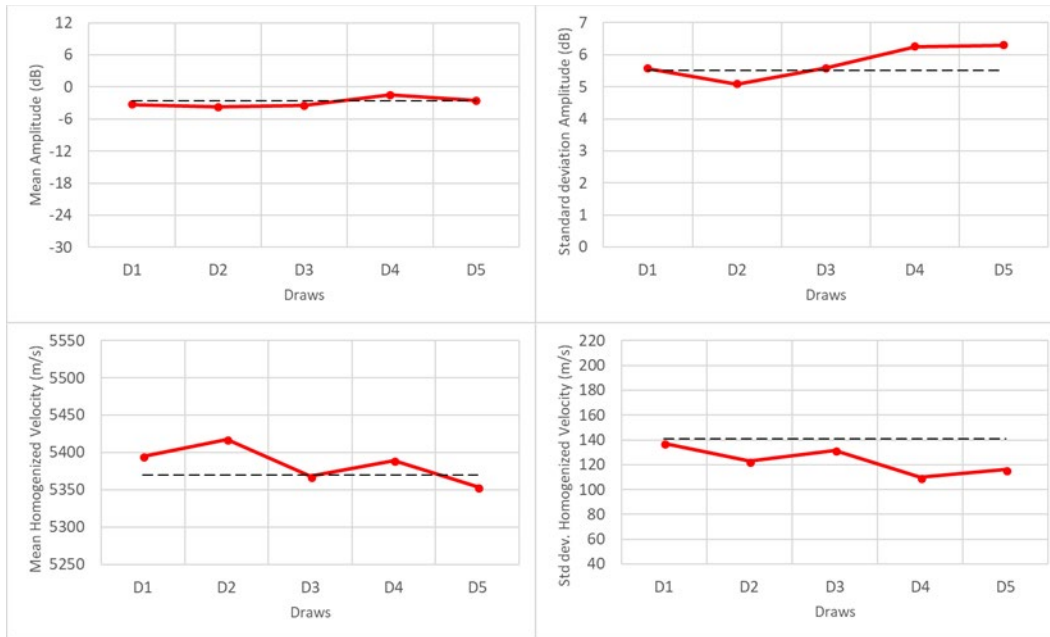
Figure 7-12
Results for five draws of random cells and velocity generation using the 2.25-MHz probe

Final CIVA Configuration Settings

Figure 7-13, Figure 7-15, and Figure 7-17 display amplitude and TOF C-scans for both experimental and simulated data for the 500-kHz, 1-MHz, and 2.25-MHz probes, respectively. Figure 7-14, Figure 7-16, and Figure 7-18 display amplitude and homogenized velocity histograms for both experimental and simulated data for the 500-kHz, 1-MHz, and 2.25-MHz probes, respectively.
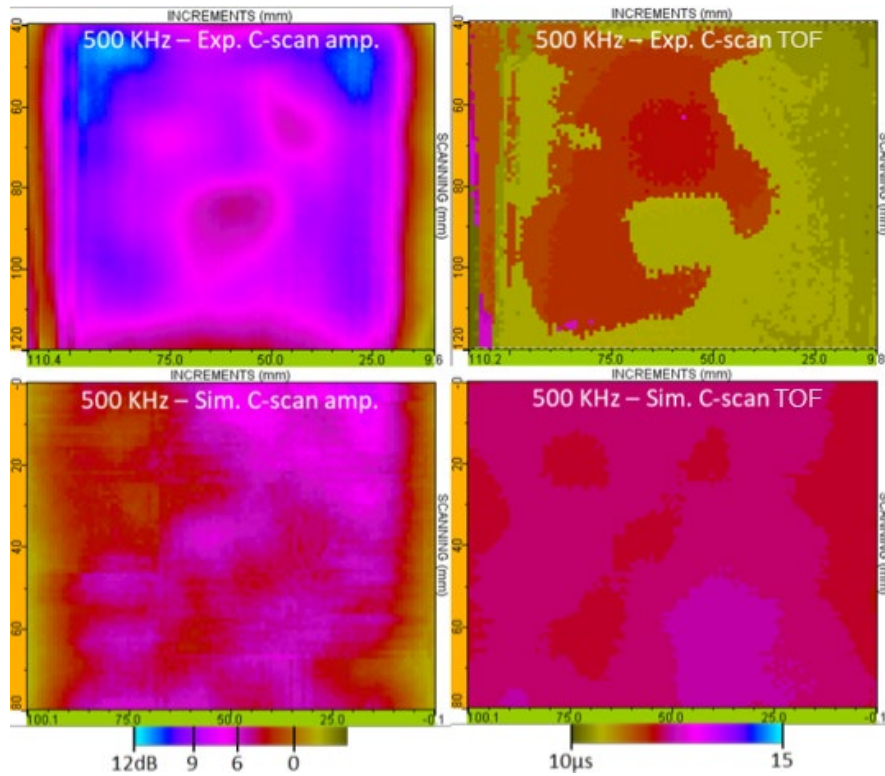
Figure 7-13
C-scans comparison of the simulation with final settings vs. experimental for 500-kHz probe
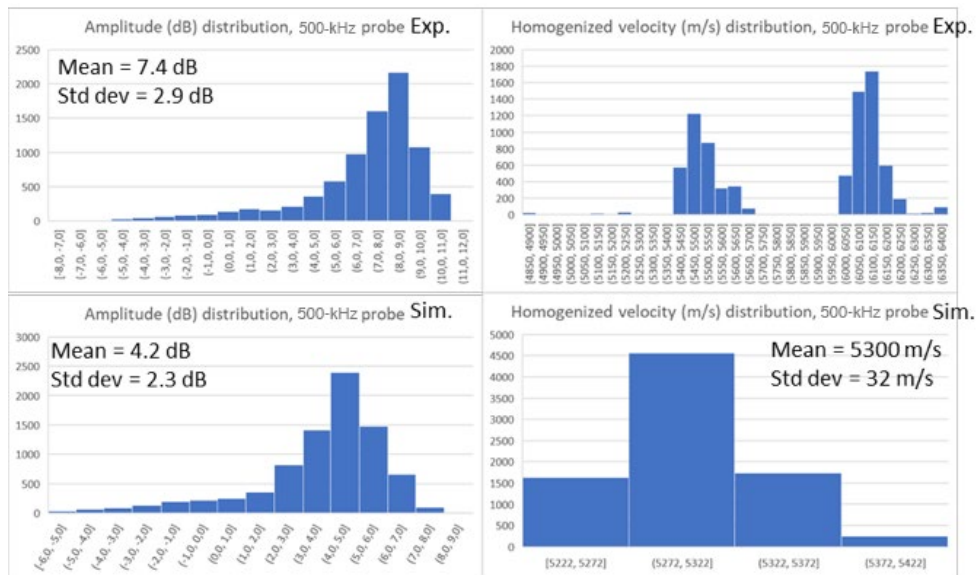
Figure 7-14
Histograms comparison of the simulation with final settings vs. experimental for 500-kHz probe
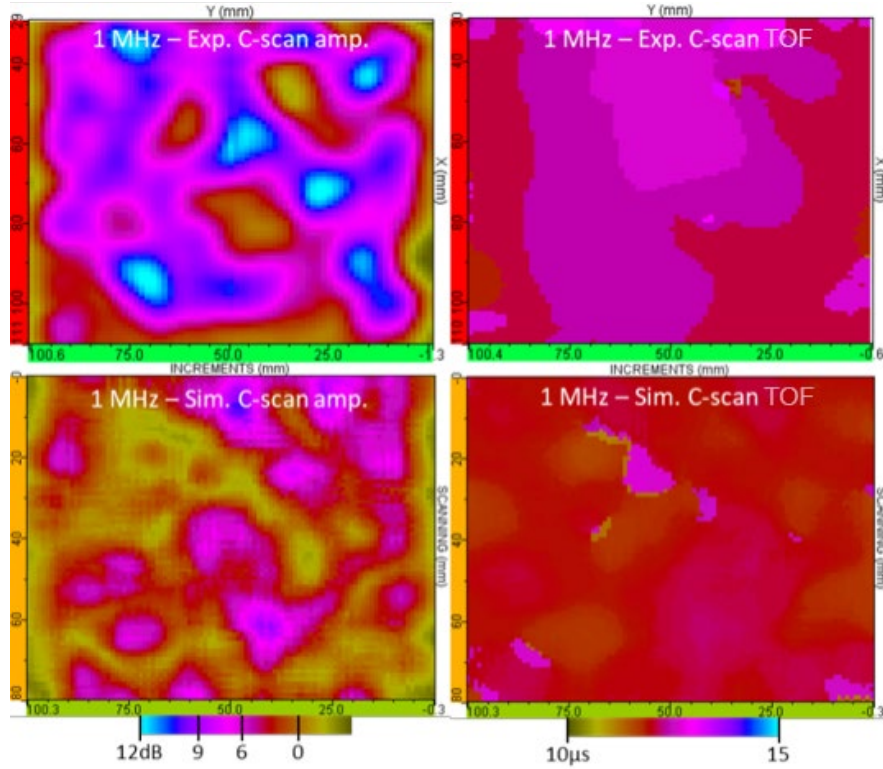
Figure 7-15
C-scans comparison of the simulation with final settings vs. experimental for 1-MHz probe
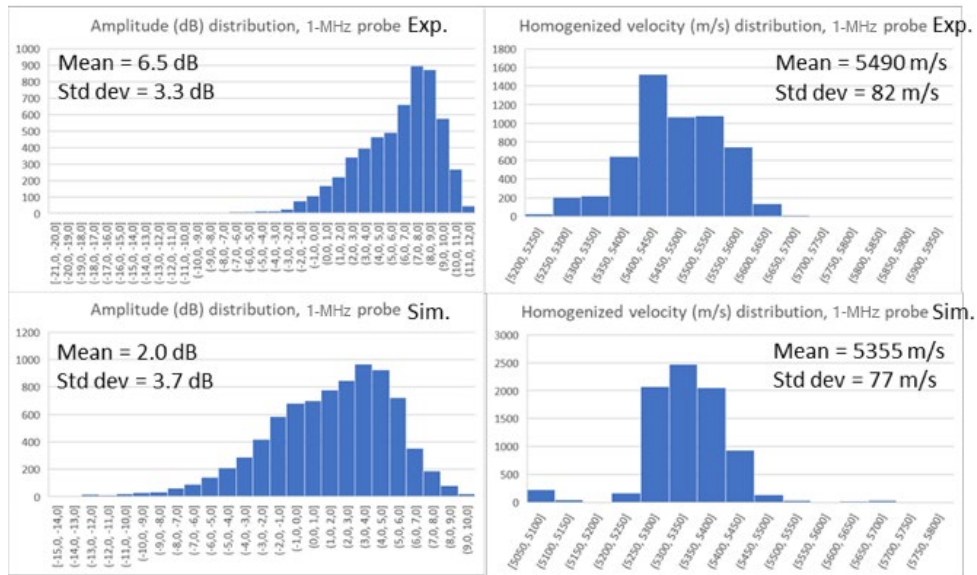
Figure 7-16
Histograms comparison of the simulation with final settings vs. experimental for 1-MHz probe
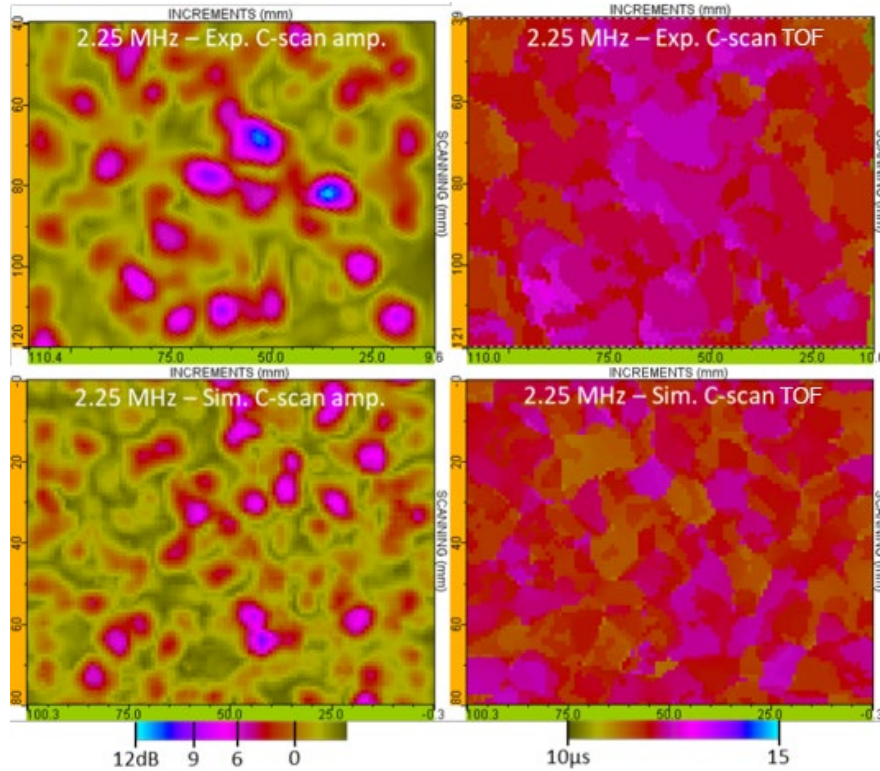
Figure 7-17
C-scans comparison of the simulation with final settings vs. experimental for 2.25-MHz probe
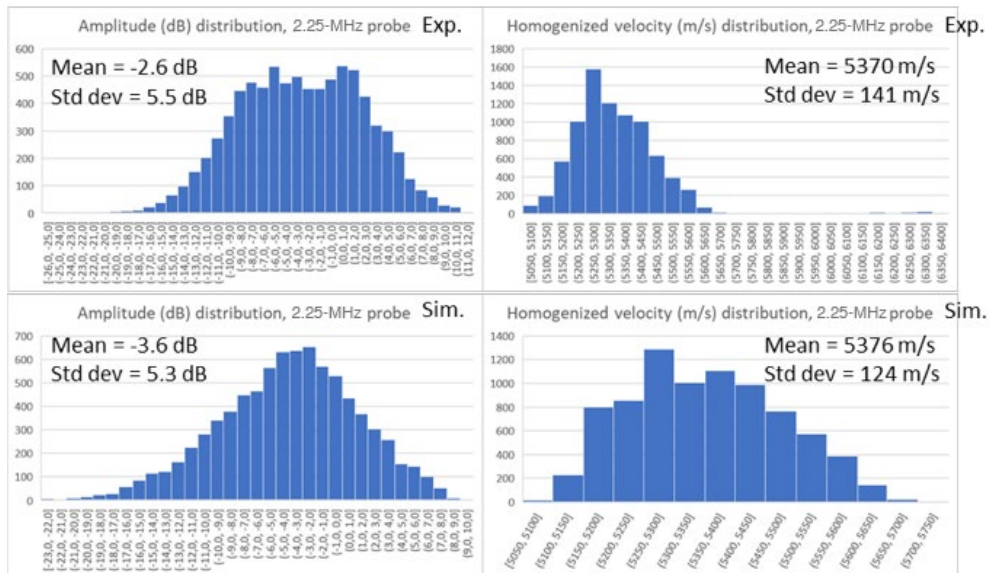
Figure 7-18
Histograms comparison of the simulation with final settings vs. experimental for 2.25-MHz probe

Simulations for the 500-kHz probe improved from the initial (Figure 7-1 and Figure 7-2) to final settings (Figure 7-13 and Figure 7-14), both in terms of amplitude and homogenized velocity; only the mean amplitude got slightly worse. The mean amplitude is undervalued by 3.2 dB, and the standard deviation by 0.6 dB. The simulation's homogenized velocity histogram still contains one peak—instead of two for experimentation—but it is wider than with the initial settings, which then makes for a better correlation with experimental data.

Simulation for the 1-MHz probe improved from the initial (Figure 7-3 and Figure 7-4) to final settings (Figure 7-16 and Figure 7-17), both in terms of amplitude and homogenized velocity variations; only the mean amplitude got slightly worse and homogenized velocity kept a reasonable error. The mean amplitude has an error of 4.5 dB, and the standard deviation is 0.4 dB. The mean homogenized velocity is undervalued by 135 m/s, and the standard deviation is 5 m/s.

Simulation for the 2.25-MHz probe significantly improved from the initial (Figure 7-5 and Figure 7-6) to final settings (Figure 7-17 and Figure 7-18), both in terms of amplitude and homogenized velocity variations. The mean amplitude has a discrepancy of 1 dB, and the standard deviation is 0.2 dB. The mean homogenized velocity is overestimated by 6 m/s, and the standard deviation undervalued by 17 m/s.

Table 7-4 contains the consolidated results for amplitude distribution and homogenized velocity measurements taken for experimental and simulated immersion tests. The experimental and initial and final simulated results are given in Table 7-4. As seen in Table 7-4, for 2.25 MHz the final simulated settings are closer to the experimental values in comparison with the initial simulation settings. This result is expected when considering that the manual parametric study was performed for the 2.25-MHz transducer.

Table 7-4
Comparison of experimental (exp.) and simulated (sim.) results for initial and final CIVA configuration settings

Frequency [MHz]	Method exp. or sim.	Amplitude Distribution Mean (std. dev.) [dB]	Homogenized Velocity Mean (std. dev.) [m/s]
0.5	Exp.	7.4 (2.9)	N/A
	Initial Sim.	6.3 (2.2)	N/A
	Final Sim.	4.2 (2.3)	5300 (32)
1.0	Exp.	6.5 (3.3)	5490 (82)
	Initial Sim.	7.2 (2.5)	5364 (17)
	Final Sim.	2.0 (3.7)	5355 (77)
2.25	Exp.	-2.6 (5.5)	5370 (141)
	Initial Sim.	0.1 (4.8)	5379 (71)
	Final Sim.	-3.6 (5.3)	5376 (124)

To evaluate these simulation results, please note that the random nature of the coarse grain involves the following limitations:

- The experimental data were observed in the study zone, but there is no guarantee that the study zone is purely applicable to the whole component's structure. Indeed, an extensive study would need to be performed to ensure the stability of the manufacturing process and to define the relevant study zone according to the model of the coarse grain in one or several components.

- Due to the random aspect of the coarse grain distribution, the simulation can reproduce the variations tendency but cannot estimate the exact same cartography.

- As observed earlier within this section, the random draws of the Voronoï cells and their velocities have an impact on simulation data, which is significant, as the considered zone is small. It means that the echo on a small flaw could significantly change depending on the random draw. This means that a correct evaluation of it would involve a large set of draws.

Another important factor to consider is the precision of the homogenized velocity calculation, which is based on the TOF between the maximum amplitude of the surface echo and the bottom echo. The precision of such a measurement can have an error up to the half-period (time between positive and negative alternations). Table 7-5 evaluates the impact of this uncertainty on the velocity for this component (thickness of 32 mm) based on a reference velocity (5430 m/s).

Table 7-5
Evaluation of homogenized velocity error

Frequency (f)	½ Period (t/2)	Erroneous TOF (TOF − t/2)	Erroneous Velocity (T/(TOF − t/2))	Velocity Precision (m/s)
500 kHz	1 µs	4.89 µs	6544 m/s	1114 m/s
1 MHz	0.5 µs	5.39 µs	5937 m/s	507 m/s
2.25 MHz	0.222 µs	5.67 µs	5644 m/s	214 m/s

Conclusions

We can state that the simulations obtained with the final CIVA settings provide a reasonable correlation with the experimental results and enable relevant studies on this component when considering the following uncertainties:

- The random aspects of Voronoï cells and their velocities

- The precision of the homogenized velocity calculation

- The variations of the experimental setup (see Section 3) evaluated to 2.0 dB, 2.5 dB, and 1.4 dB for the 500-kHz, 1-MHz, and 2.25-MHz probes, respectively

- The errors observed on the SDHs for the characterization (see Section 3) evaluated up to 2.0 dB, 1.7 dB, and 0.9 dB for the 500-kHz, 1-MHz and 2.25-MHz probes, respectively

8
CONTACT PROBE EVALUATION

This section aims at evaluating the final CIVA settings of the coarse grain model with the 1.0-MHz contact probe (dual phased array probe) (Section 2) on the J7010-4 component (Figure 8-1). The evaluation was performed with the SDHs and the large crack in a flat component due to CIVA limitations (Section 6). The curved bottom face, weld root geometry, and the small crack could not be simulated.
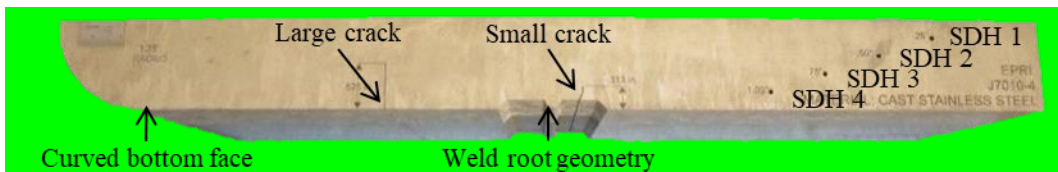
Figure 8-1
Flaws and geometries of J7010-4

Experimental Data of the Contact Probe on J7010-4

Two scans of the J7010-4 component were performed with a 1-mm step for both the scan and increment axes. The scans were performed for the skew 0° (beam steering oriented toward the curved bottom face) and skew 180° probe orientation (beam steering oriented away from the curved bottom face). Figure 8-2 shows the data for the probe in the two directions.
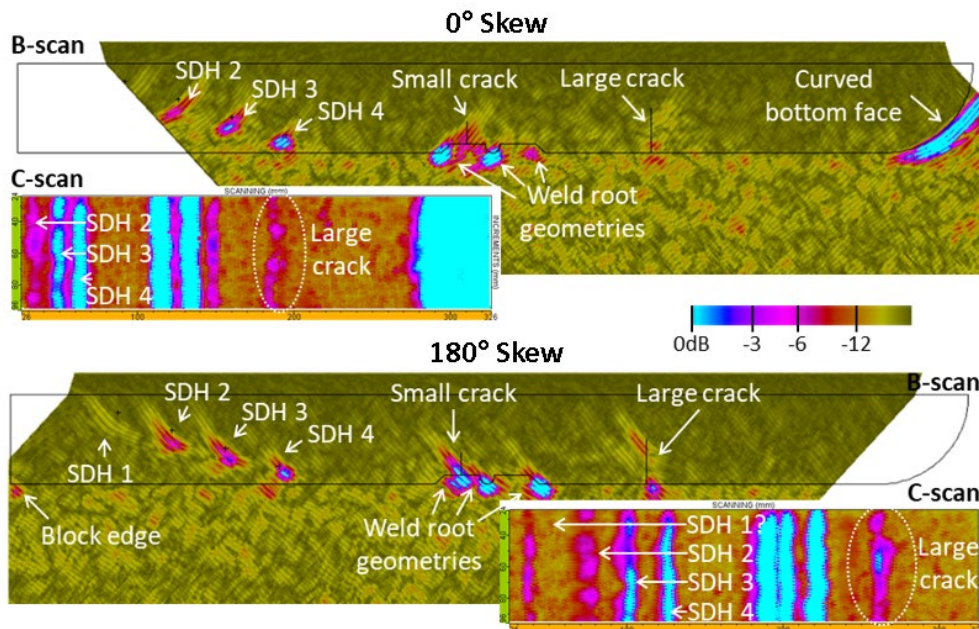
Figure 8-2
Experimental data of front orientation at the top and back at the bottom of the contact probe

The scans started with the rear corner of the probe at the corner edge of the component. Each of them is displayed as a C-scan and the B-scan of the central increment position. All the flaws and geometries are observed. SDH 1 has a lower amplitude than the others SDHs. Some structural noise appears below the bottom face. For all the flaws and geometries, the data show variations in amplitude and positioning.

Table 8-1 reports indicators extracted from experimental data to allow for future evaluations with the simulations. The amplitude variations are defined by the minimum and maximum. SDHs are only considered in the skew 180° direction to avoid partial shadowing effects. The large crack is studied from both skews. The small crack echo is affected by the weld root geometry that cannot be simulated in CIVA in the case of coarse grain structure.

Table 8-1
Experimental indicators for future simulations evaluation

Flaw	Skew	Minimum Amplitude	Maximum Amplitude
SDH 1	180°	−15.4 dB	−11.2 dB
SDH 2	180°	−9.7 dB	−3.4 dB
SDH 3	180°	−4.6 dB	1.8 dB
SDH 4	180°	−7 dB	3.6 dB
Large crack tip diffraction	180°	−14 dB	−7.7 dB
Large crack corner	180°	−8.2 dB	0.1 dB
Large crack tip diffraction	0°	−12.1 dB	−8.6 dB
Large crack corner	0°	−8.3 dB	−3.2 dB

Simulation Data of the Contact Probe on J7010-4

Computation Settings

This section aims at defining suitable computation parameters as performed for the immersion probes in Section 6. First, several values of the *field precision* parameters are compared in Figure 8-3. It shows that below a value of 10, some pixels cannot be evaluated, considering a pixel step of 0.5 mm ($\lambda/10$). This latest value of *field precision* 10 is then kept for future computations with the contact probe.
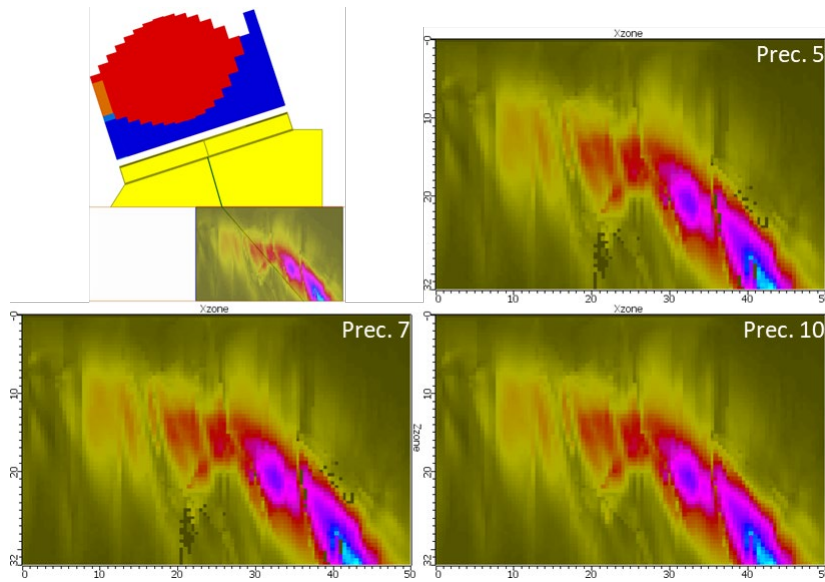
Figure 8-3
Field precision **impact for the contact probe**

Figure 8-4 compares the results with different *defect precision* values for a four-positions scan of the probe with random rectangular flaws. A *defect precision* of 3 (error < 1 dB from a precision of 10) is considered for the next computations with the contact probe.
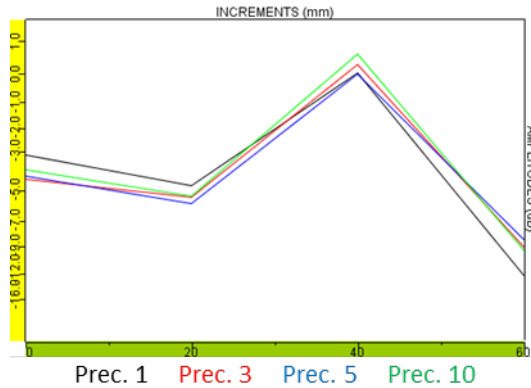
Figure 8-4
Defect precision **impact for the contact probe**

The sensitivity zone size was not studied here because its behavior is different for geometry and flaw echoes. In the first case, the sensitivity zone considers as a reflector only the intersection between the defined box and the geometry face. The second case considers the whole flaw since the defined box intersects the flaw, which means that for each position either the flaw echo is not evaluated, or it is correctly evaluated (binary phenomenon).

Simulations vs. Experimental Data

The C-scans zoomed on the four SDHs are compared between experimental and simulated data in Figure 8-5. Simulation and experiments were performed with the same scanning and index step of 1 mm. The simulation qualitatively matches the experiment well. Table 8-2 reports the indicators values of the simulation. This quantitative comparison shows again a good agreement considering the expected variations/uncertainties as described in Section 7.
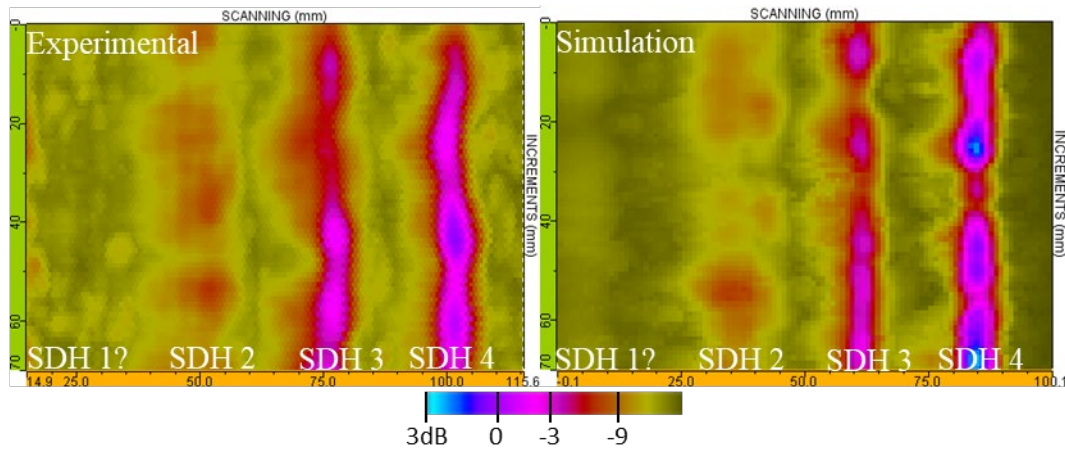
Figure 8-5
C-scans of the SDHs scanned in the skew 180° orientation for experiment (left) and simulation (right)

Table 8-2
Simulated indicators for the SDHs, delta (simulation - experiment) in parentheses

Flaw	Skew	Min Amplitude	Max Amplitude
SDH 1	180°	−20.4 dB (−5 dB)	−14.2 dB (−3 dB)
SDH 2	180°	−11.3 dB (−1.6 dB)	−3.5 dB (−0.1 dB)
SDH 3	180°	−4.8 dB (−0.2 dB)	1.1 dB (−0.7 dB)
SDH 4	180°	−2.4 dB (+4.6 dB)	5.6 dB (+2 dB)

Because of the extensive computation time (see Appendix C) on the large crack, only three increment positions were simulated. Positions 1, 2, and 3 in the simulation were compared to the increments 0 mm, 35 mm, and 70 mm in the experiment. Note that the simulation positions 1, 2, and 3 do not contain the exact same grain structures as experimental increments. That means this is a comparison between three different increments whose grain structures are still random in comparison with one another. Both Figure 8-6 and Figure 8-7 show experimental and simulated B-scans for skew 180° and 0° orientations, respectively. This qualitative comparison provides a relatively good match. Table 8-3 reports the indicators' values of the simulation. This quantitative comparison shows a good agreement, considering the expected variations/uncertainties of the configuration and the evaluation of the experimental indicators, which are strongly dependent on the size and location of the delimitation zone used. SNR was not used as a comparative metric.

Table 8-3
Simulated indicators for the large crack, delta (simulation – experiment) in parentheses –
∈ when between experimental minimum and maximum

Flaw	Skew	Position	Simulation Amplitude	Experimental Min	Max
Large crack tip diffraction	180°	1	−18.6 dB (−4.6 dB)	−14 dB	−7.7 dB
Large crack corner	180°	1	−11.5 dB (−3.3 dB)	−8.2 dB	0.1 dB
Large crack tip diffraction	0°	1	−9.6 dB (∈)	−12.1 dB	−8.6 dB
Large crack corner	0°	1	−6.3 dB (∈)	−8.3 dB	−3.2 dB
Large crack tip diffraction	180°	2	−13.1 dB (∈)	−14 dB	−7.7 dB
Large crack corner	180°	2	−6.4 dB (∈)	−8.2 dB	0.1 dB
Large crack tip diffraction	0°	2	−17 dB (−4.9 dB)	−12.1 dB	−8.6 dB
Large crack corner	0°	2	−8.7 dB (−0.5 dB)	−8.3 dB	−3.2 dB
Large crack tip diffraction	180°	3	−17 dB (-3.3 dB)	−14 dB	−7.7 dB
Large crack corner	180°	3	−9.7 dB (−1.5 dB)	−8.2 dB	0.1 dB
Large crack tip diffraction	0°	3	−12.3 dB (−0.2 dB)	−12.1 dB	−8.6 dB
Large crack corner	0°	3	−7.1 dB (∈)	−8.3 dB	−3.2 dB
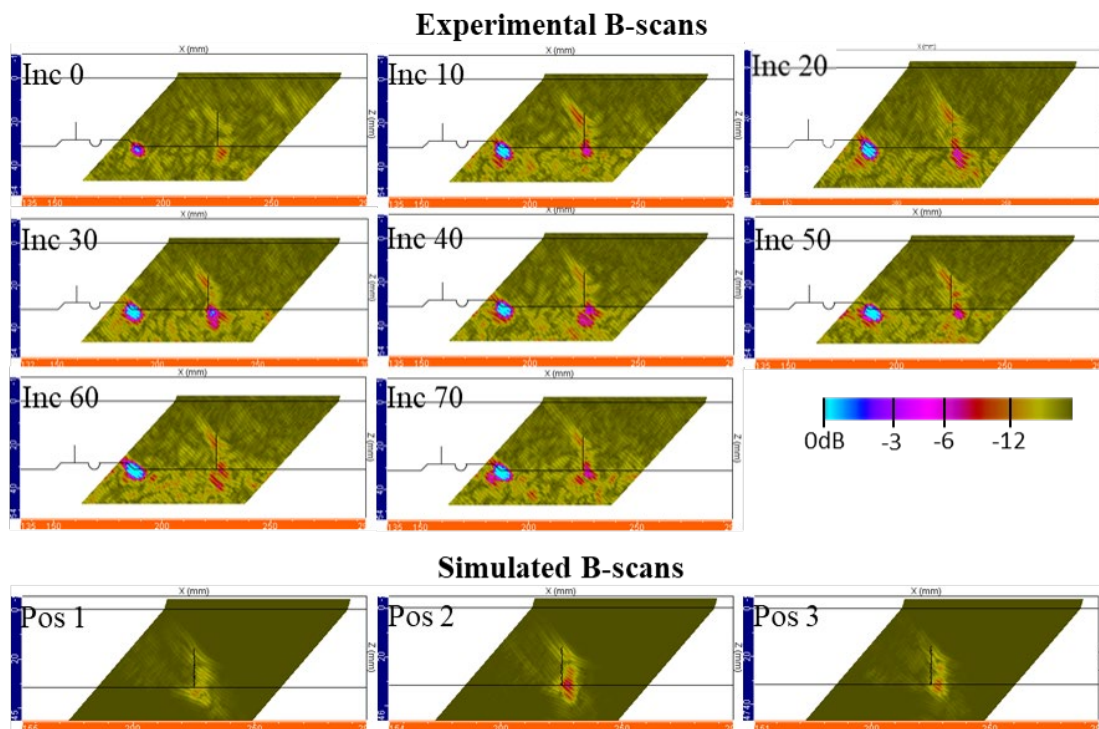
Figure 8-6
B-scans of the large crack scanned back for experiment (top) and simulation (bottom)
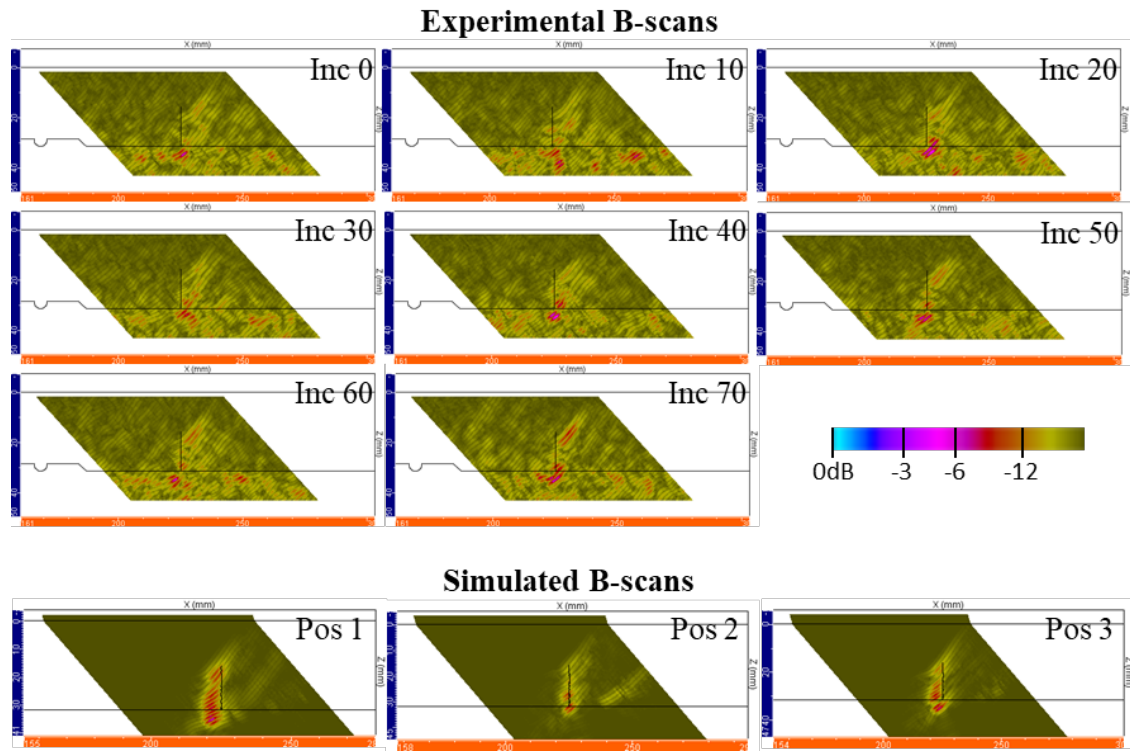
Figure 8-7
B-scans of the large crack scanned front for experiment (top) and simulation (bottom)

9
CONCLUSIONS

This report presented material characteristics of CASS that make its ultrasonic inspection and modeling and simulation difficult. As part of this research, an approach to define a coarse grain structure in CIVA for UT was proposed. Prior to coarse grain simulations, an effort was placed on properly characterizing the probes with a homogeneous material of well-known attributes to accomplish the following: define CIVA probe settings, define amplitude references, and evaluate experimental error and uncertainty due to the whole system chain.

To minimize experimental uncertainties, a set of reference experimental data was taken in immersion with a 0° longitudinal beam. A study zone was chosen such that its upper and bottom surface faces were parallel and its volume was free of flaws. The approaches presented within this report were based on results from a parametric study to best fit experimental results. The parametric study was performed with a 2.25-MHz probe because this high frequency gave maximum sensitivity with the grain structure. The correspondence to experimental data was evaluated with four metrics: mean amplitude, amplitude standard deviation, mean homogenized velocity, and homogenized velocity standard deviation.

CIVA model's coarse grains with Voronoï cells, each of which has randomly defined velocities with a uniform distribution. This report presented an application with a contact dual matrix phased array probe when delays are set to generate a 45° longitudinal angle beam focusing at the bottom of the sample. The simulations show a good qualitative and quantitative match with the experiments. SNR was not included in this study but would serve as a useful comparative metric between simulated and experimental data. Using SNR as a comparative metric could help with setting up simulations and adjusting input parameters.

Some limitations were observed in this report:

- As detailed in Section 7, the coarse grain structures present a random aspect that does not allow a user to reproduce the exact same experimental results. The user can only produce similar representative variations.

- The random aspects require the user to define a zone of study that is relevant to the manufacturing process and to multiply the Voronoï cells' generation and their velocity to ensure a correct evaluation of the induced variations.

- Currently, CIVA's predefined coarse grain structures are limited to components whose geometry is a plate or cylinder. This limitation prevented simulating specific geometrical features in J7010-4, such as the simulated weld root and counterbore. Other alternative solutions for modeling coarse grain structures with complex geometries were not presented in this report and are potential areas for future research.

- The proposed approach only considers longitudinal waves. Shear waves propagation in coarse grains was not considered in the present report and would need a specific extensive study.

- Single crystals in CASS materials are anisotropic, and the individual grains modeled here are isotropic with different velocity distributions. Future studies could use anisotropic base and weld materials for the individual grains to further understand modeling differences.

- The parametric study could be extended to include more test frequencies; however, this would significantly increase computation times.

The proposed modeling and simulation approach defined in this report was designed to be applied with any other similar samples and ultrasonic probes, when considering certain limitations. The next research step would be to apply this approach on another CASS sample, for instance, a component whose predominant geometry is cylindrical.

10 REFERENCES

1. A. Cinson, S. Crawford, A. Diaz, M. Larche, M. Prowant, and M. Anderson. *Phased Array Ultrasonic Sound Field Mapping in Cast Austenitic Stainless Steel*. Pacific Northwest National Laboratory, PNNL-23393, 2014.

2. T. Szabo. *Diagnostic Ultrasound Imaging: Inside Out*, 2nd ed. Elsevier Scientific Publishing, 2014, p. 257–265.

3. M. Anderson, A. Cinson, S. Crawford, S. Cumblidge, and A. Diaz, "Research and Evaluation of Advanced Nondestructive Examination (NDE) Methods for Addressing the Challenges of Inspecting Cast Austenitic Stainless Steel (CASS) Piping." Presented at the 7th International Conference on NDE in Relation to Structural Integrity for Nuclear and Pressurized Components (May 2009).

4. CEA, June 2018. [Online]. Available at http://www-civa.cea.fr/en/.

5. EXTENDE, May 2018. [Online]. Available at http://www.extende.com/.

6. ImageJ Software, March 2018. [Online]. Available at https://imagej.nih.gov/ij/.

7. M. Darmon, S. Chatillon, S. Mahaut, P. Calmon, L.J. Fradkin, and V. Zernov, "Recent advances in semi-analytical scattering models for NDT simulation," *Journal of Physics Conference Series* (online). Vol. 269, No. 1, p. 12 (2011). doi:101088/1742-6596/269/1/012013.

8. S. Mahaut et al., "Recent advances and current trends of ultrasonic modelling in CIVA," *Insight—Non-Destructive Testing and Condition Monitoring.* Vol. 51, No. 2 (2009).

A
AMPLITUDE CALIBRATIONS

This appendix presents the method to compare amplitudes of M2M MultiX experimental and CIVA simulation data. The calibration process relies on the probe characterization during which reference values are backed up.

Reference Values from Probe Characterization

As shown in Table A-1, during the characterization process, three reference values are considered:

- G_{ref} is the total experimental gain (hardware + software).

- Experimental amplitude is the experimental absolute amplitude (point [pt] unit) on the reference flaw.

- Simulation amplitude is the simulation absolute amplitude (pt unit) on the reference flaw.

Table A-1
Amplitude reference values for the probes

Probe	G_{ref}	Experimental Amplitude	Simulation Amplitude
Immersion 500 kHz	34.8 dB	495 pt	159.863 pt
Immersion 1 MHz	31.3 dB	318 pt	5.34 pt
Immersion 2.25 MHz	21.5 dB	383 pt	0.778 pt
Contact 1 MHz	70.1 dB	7400 pt	24.2 pt

Calibration of Experimental Data

Experimental data are calibrated based on the reference values of the probe considered (Table A-1). In the *Palette/Gain* tab of CIVA (see Figure A-1), the following parameters are defined as detailed:

- *Calibrate* is activated.

- *Reference amplitude* is set to the experimental amplitude value as given in Table A-1.

- *Hardware gain* is left to the current experimental value (G_{hard}).

- *Software gain* is set to G_{ref} - G_{soft} - G_{hard} where G_{soft} is the software gain of the current acquisition. This field should not be left void (set a value even if 0); otherwise the calibration is not correctly considered.
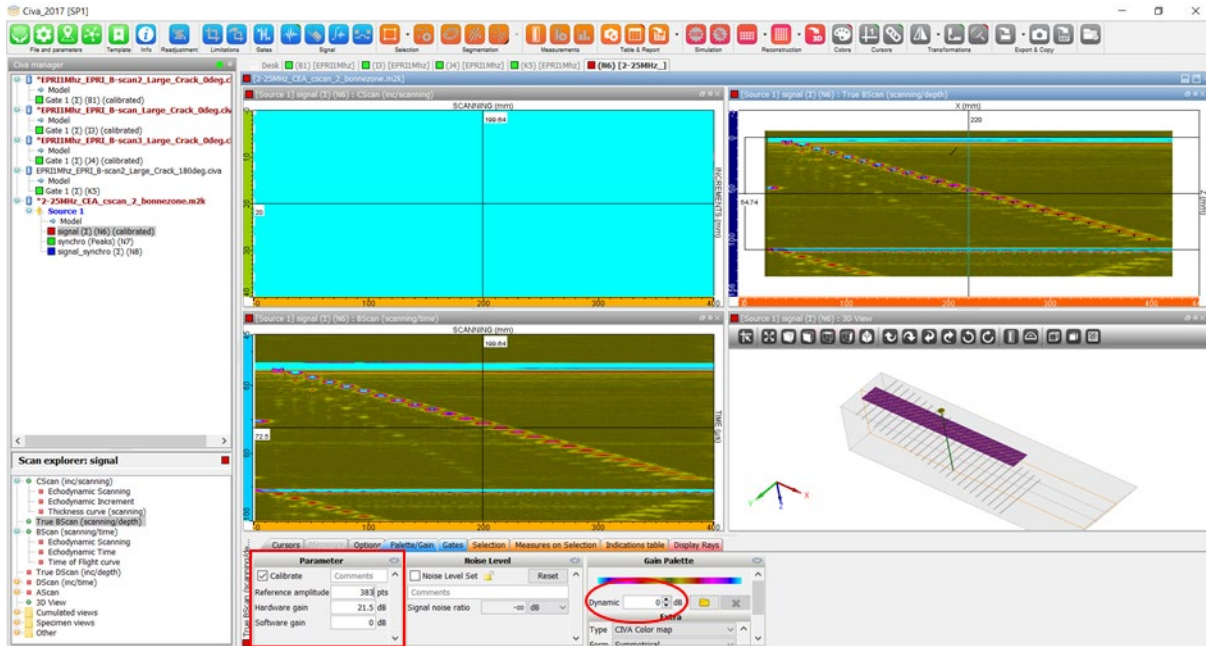
Figure A-1
Calibration of experimental data

Calibrate Simulation Data

Simulation data is calibrated based on the reference values of the probe considered (see Table A-1). In the *Palette/Gain* tab of CIVA (Figure A-1), the following parameters are defined as detailed:

- Calibrate is activated.

- *Reference amplitude* is set to the simulation amplitude value as given in Table A-1.

- *Hardware gain* and *Software gain* are set to 0.

B
ADDITIONAL DATA

Figures B-1 through B-14 display additional experimental and simulated data, not required in the report but still interesting for the reader.

Immersion Probe Characterization
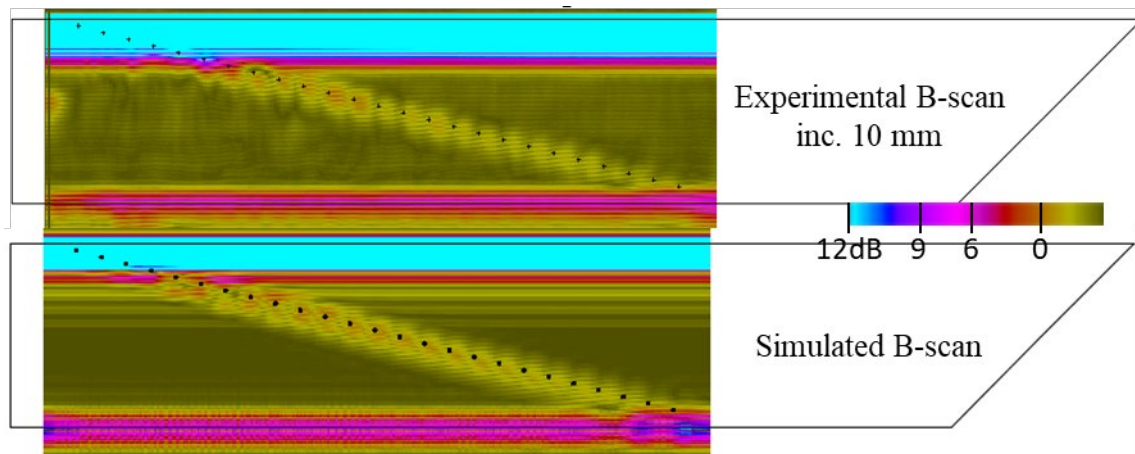
Figure B-1
500-kHz immersion probe characterization
Note: inc. = increment.
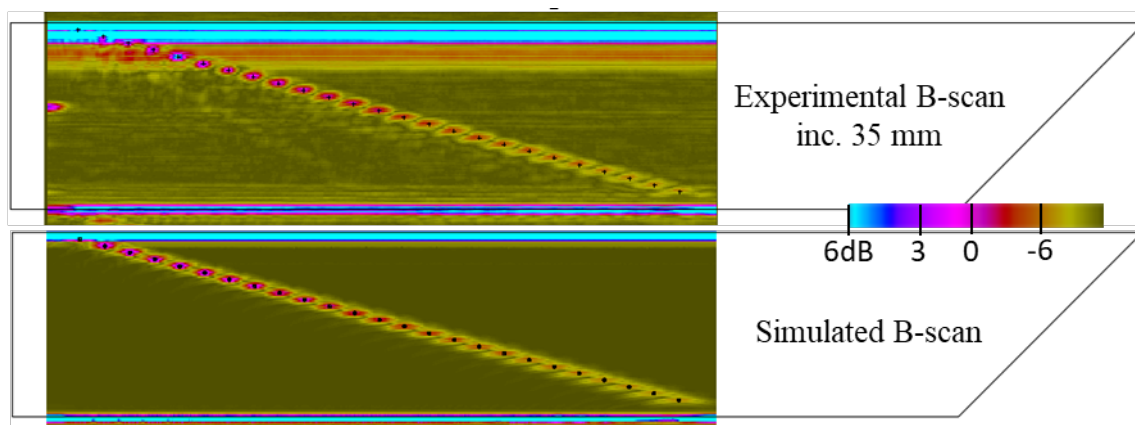
Figure B-2
1-MHz immersion probe characterization
Note: inc. = increment.
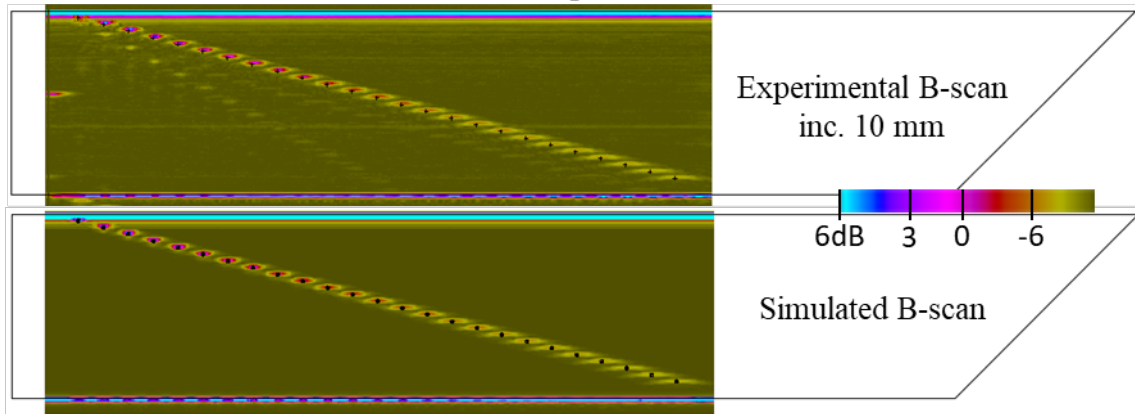
Figure B-3
2.25-MHz immersion probe characterization
Note: inc. = increment.
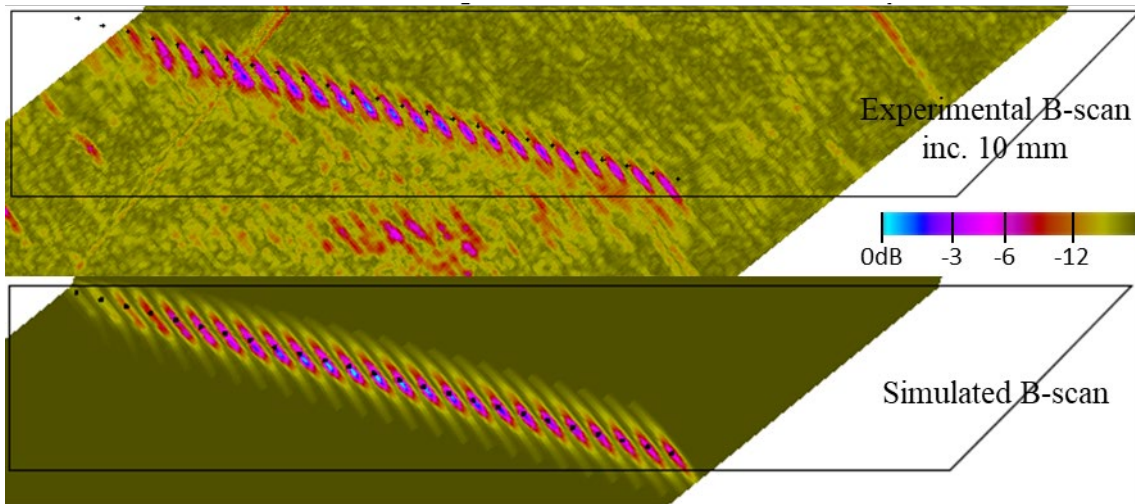
Figure B-4
1-MHz contact probe characterization with no steering
Note: inc. = increment.
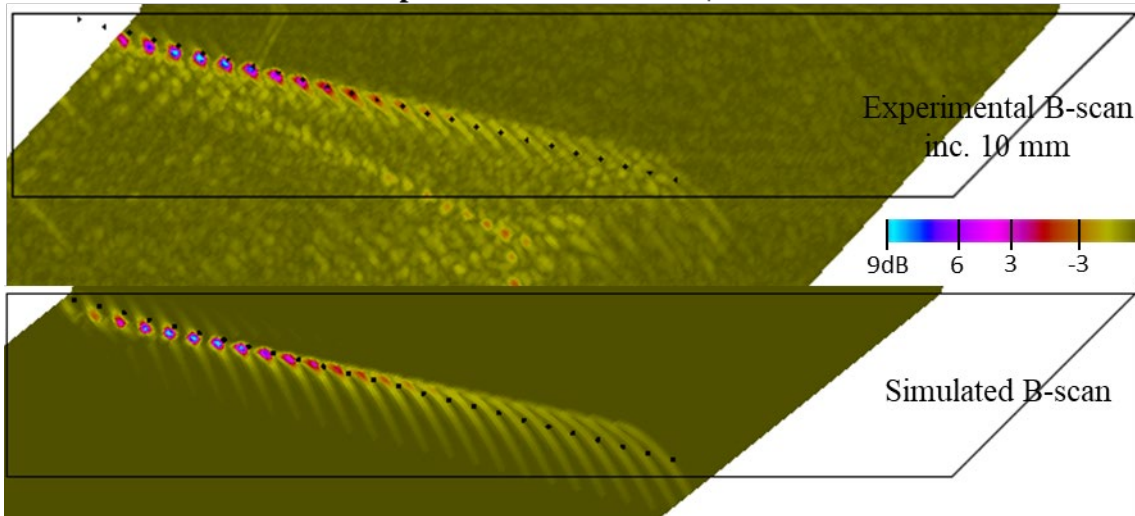
Figure B-5
1-MHz contact probe characterization with focusing at 32-mm depth using a 45° L-wave
Note: inc. = increment.

Experimental Data on the Full Sample
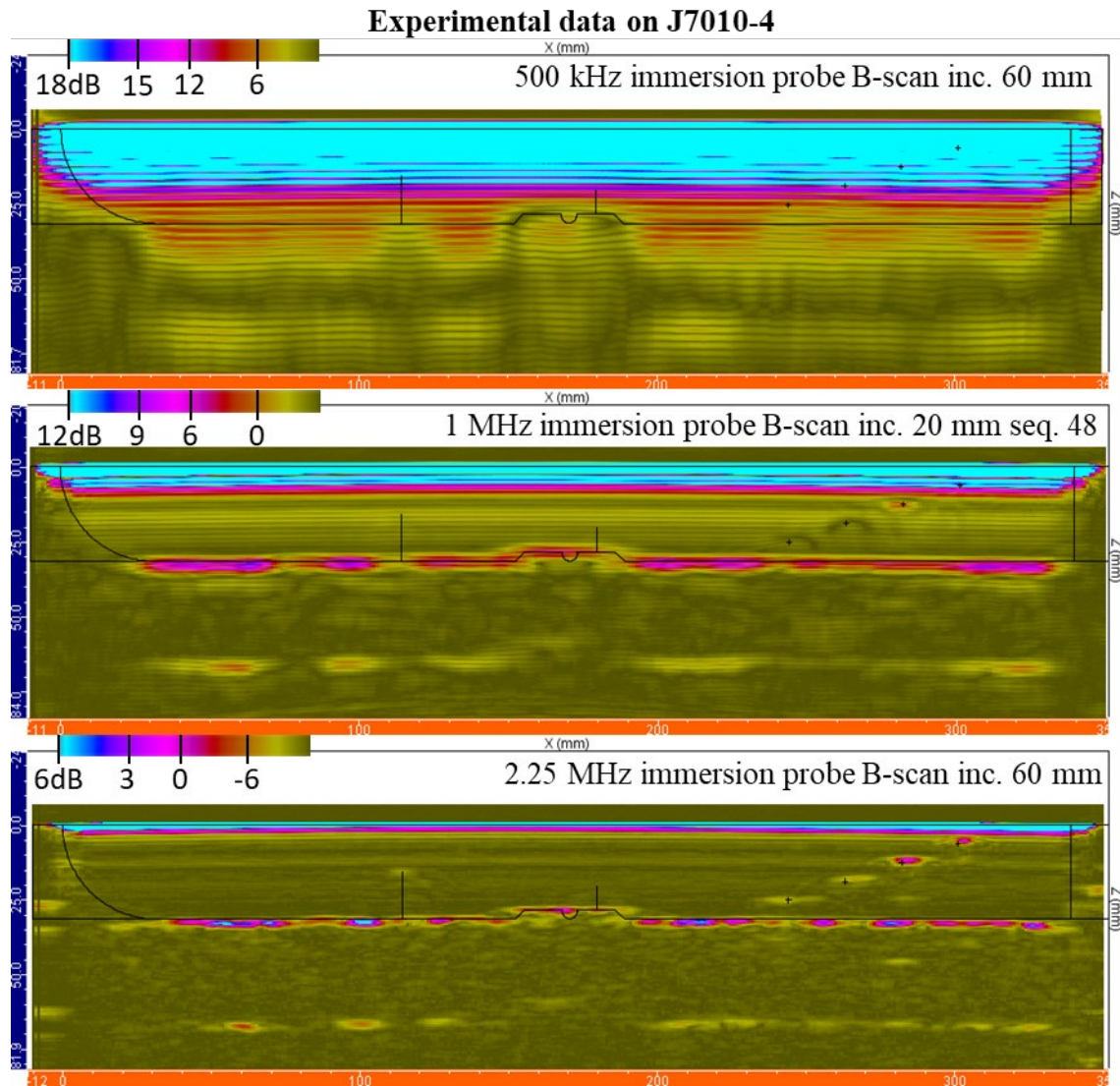
Figure B-6
Experimental data on J7010-4
Note: inc. = increment.

Parametric Study
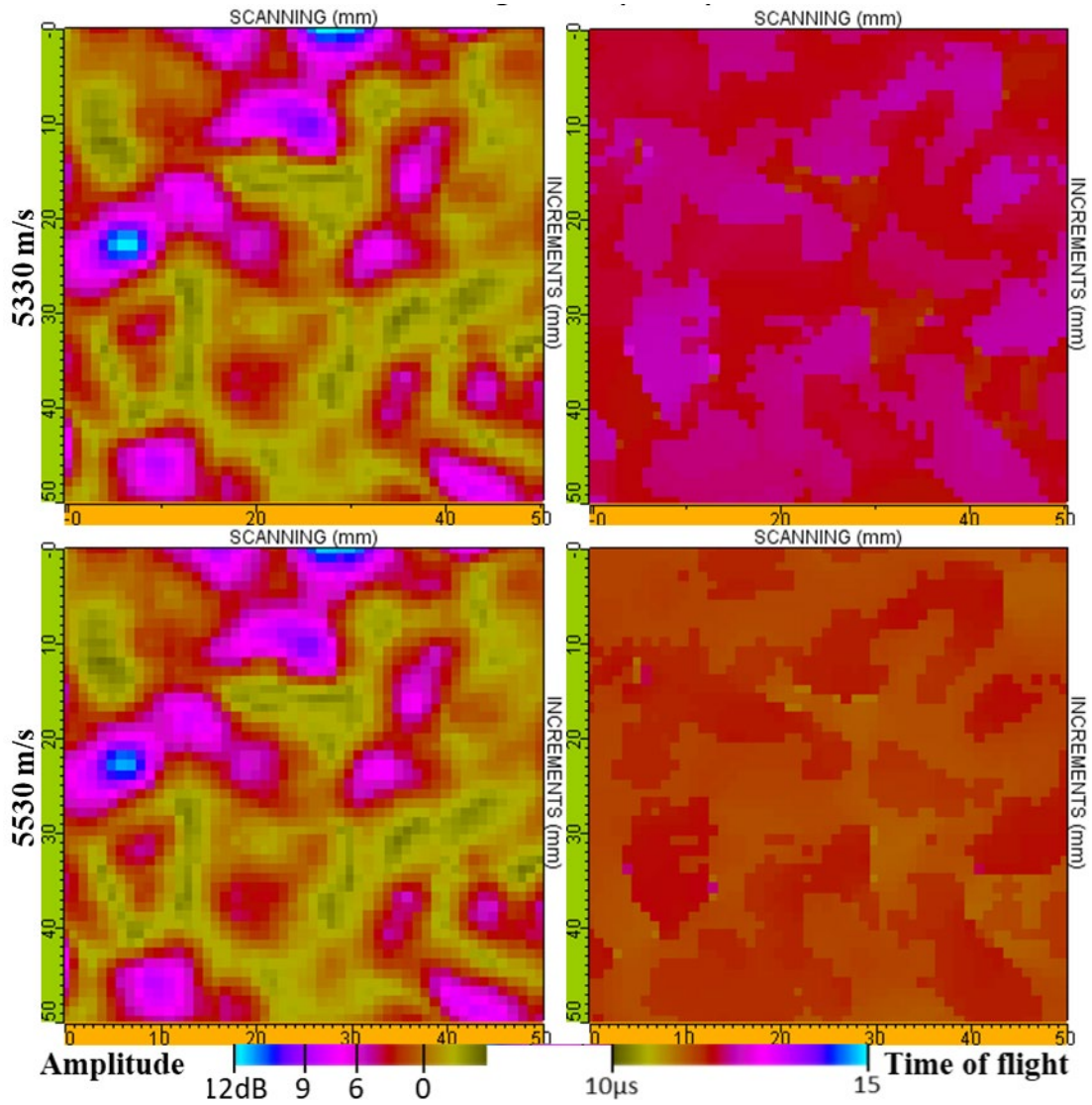
Figure B-7
Homogenized grain speed—amplitudes (left column) and times of flight (right column) as homogenized grain speed are varied at 5330 ms^{-1} (top row) and 5530 ms^{-1} (bottom row).
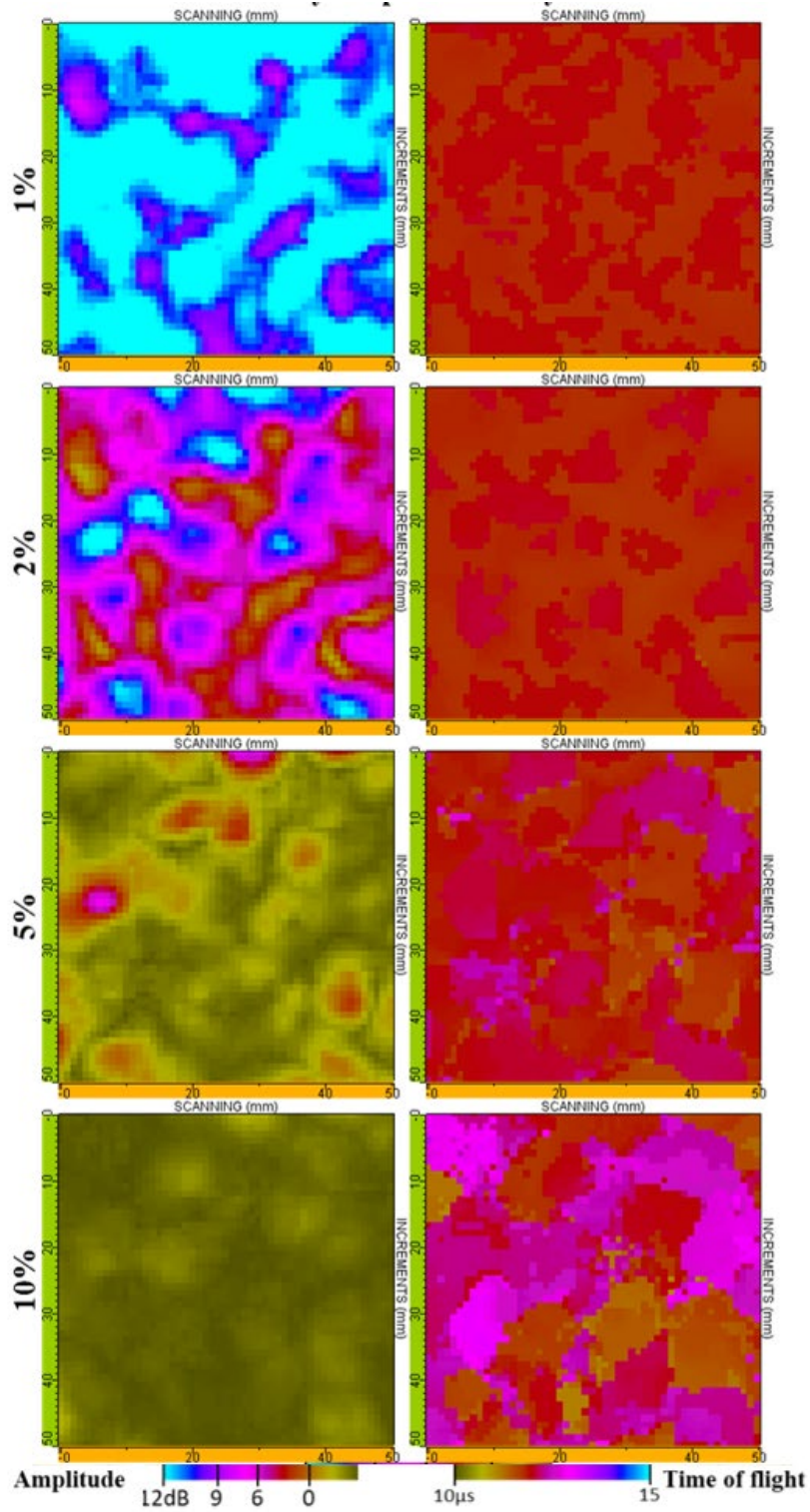
Figure B-8
Velocity dispersion—amplitudes (left column) and times of flight (right column) as velocity dispersion are varied, by row, from 1% to 10%
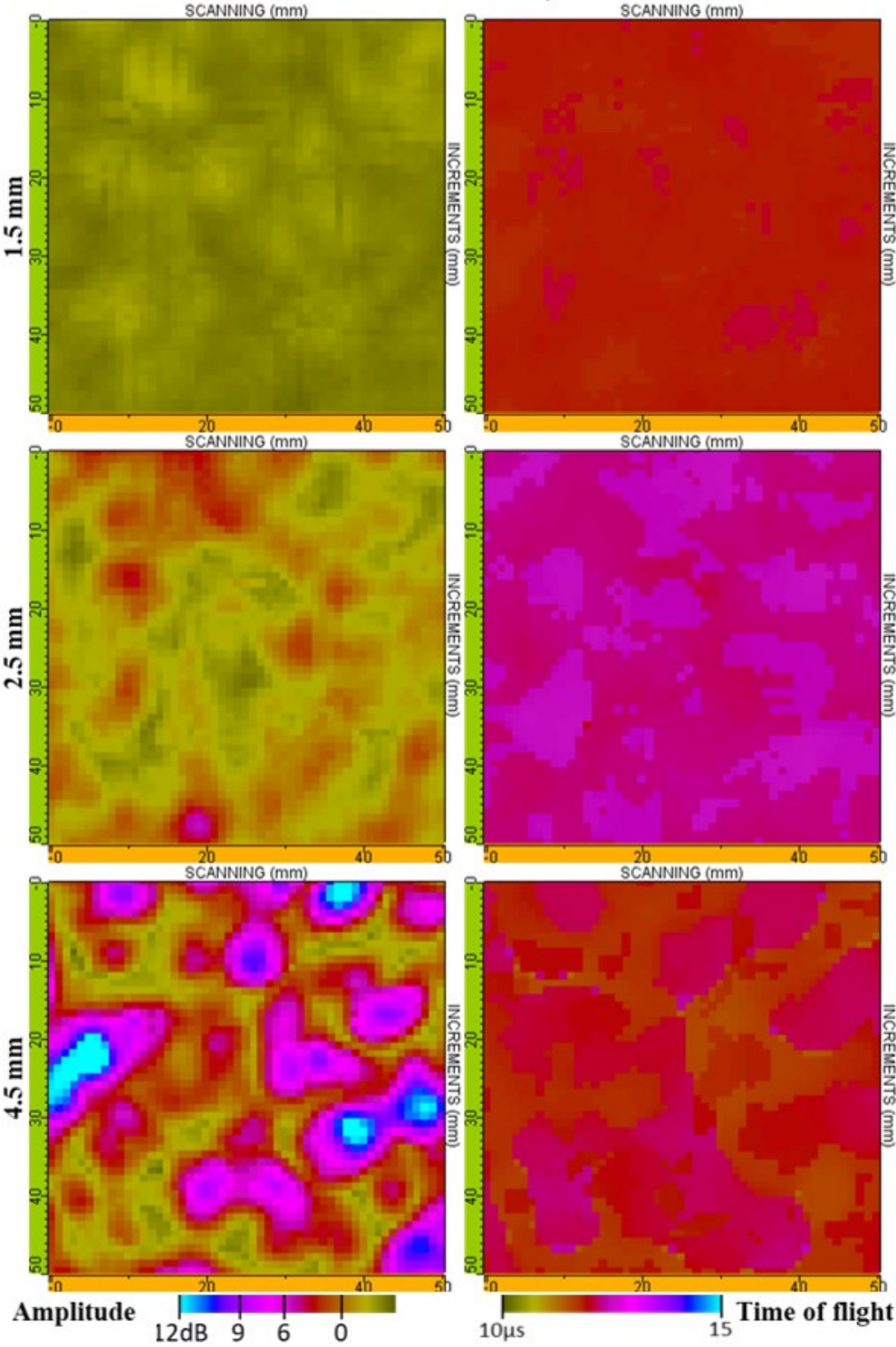
Figure B-9
Grain size—amplitudes (left column) and times of flight (right column) as grain size are varied, by row, from 1.5 mm to 4.5 mm
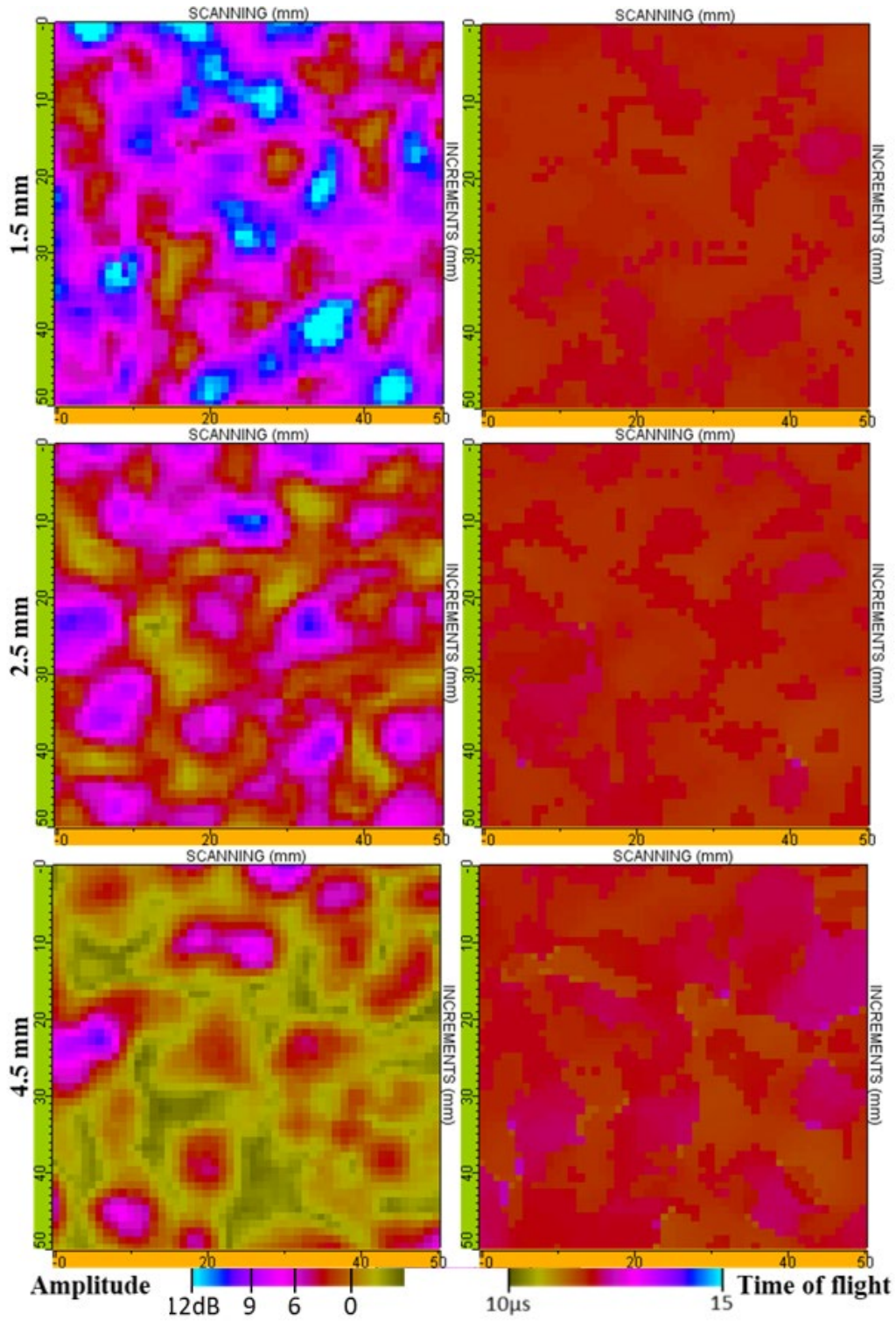
Figure B-10
Grain elongation—amplitudes (left column) and times of flight (right column) as grain elongation are varied, by row, from 1.5 mm to 4.5 mm
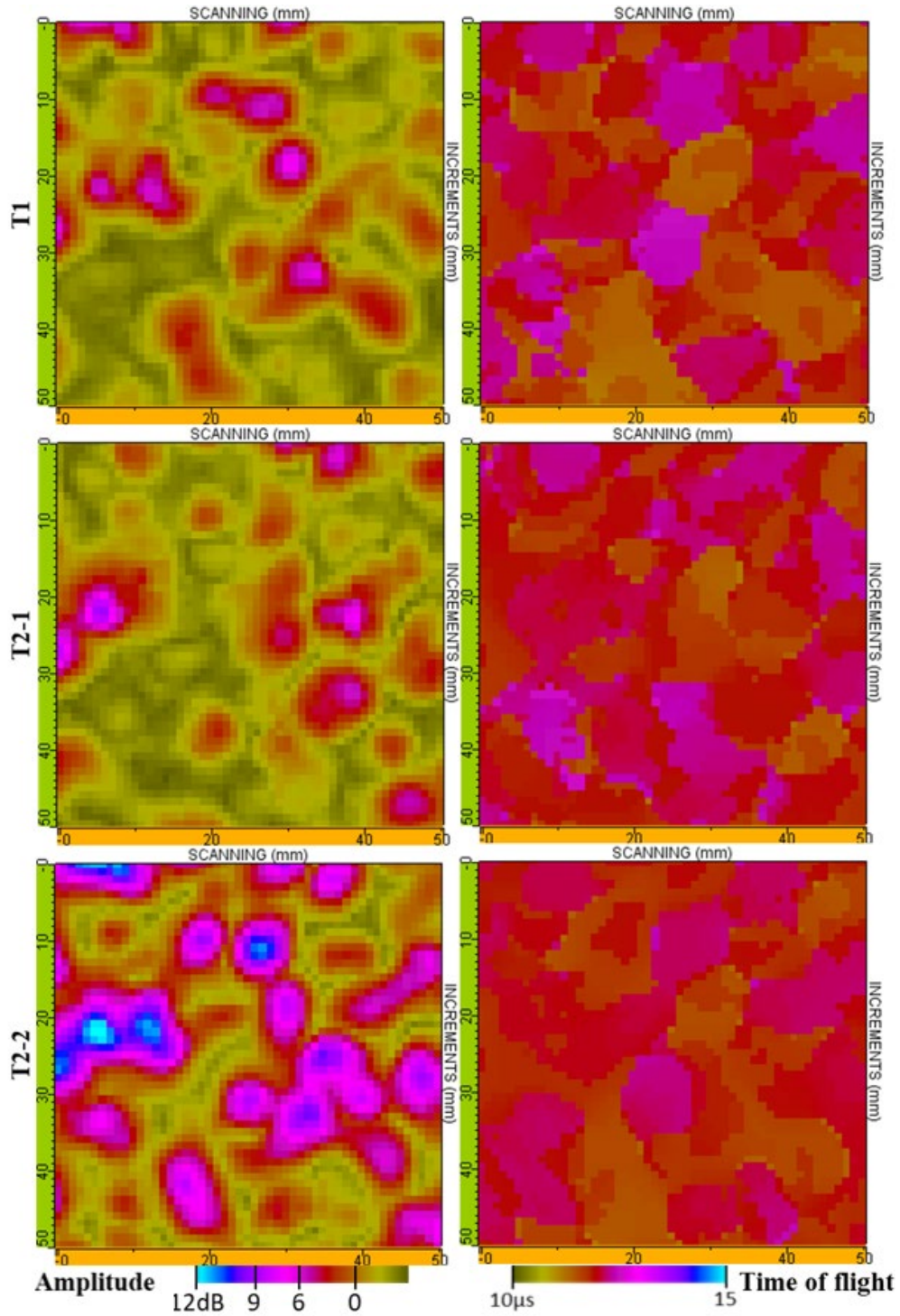
Figure B-11
Grain elongation, manual optimization (1/2)—amplitudes (left column) and times of flight
(right column) as grain elongation are varied, by row, for manual test sets T1, T2-1, and T2-2
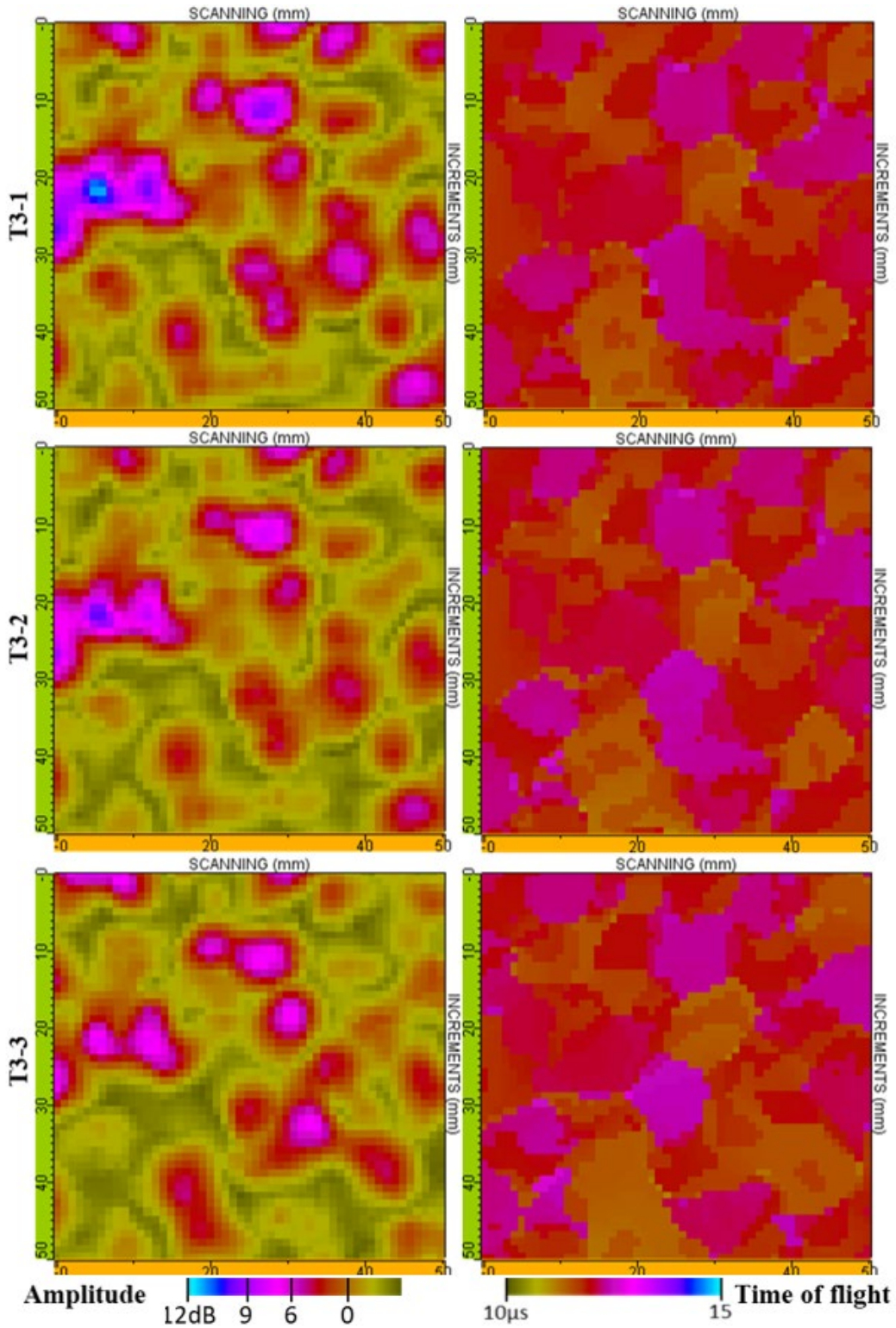
Figure B-12
Grain elongation, manual optimization (2/2)—amplitudes (left column) and times of flight
(right column) as grain elongation are varied, by row, for manual test sets T3-1, T3-2, and T3-3

Cells and Velocity Draws
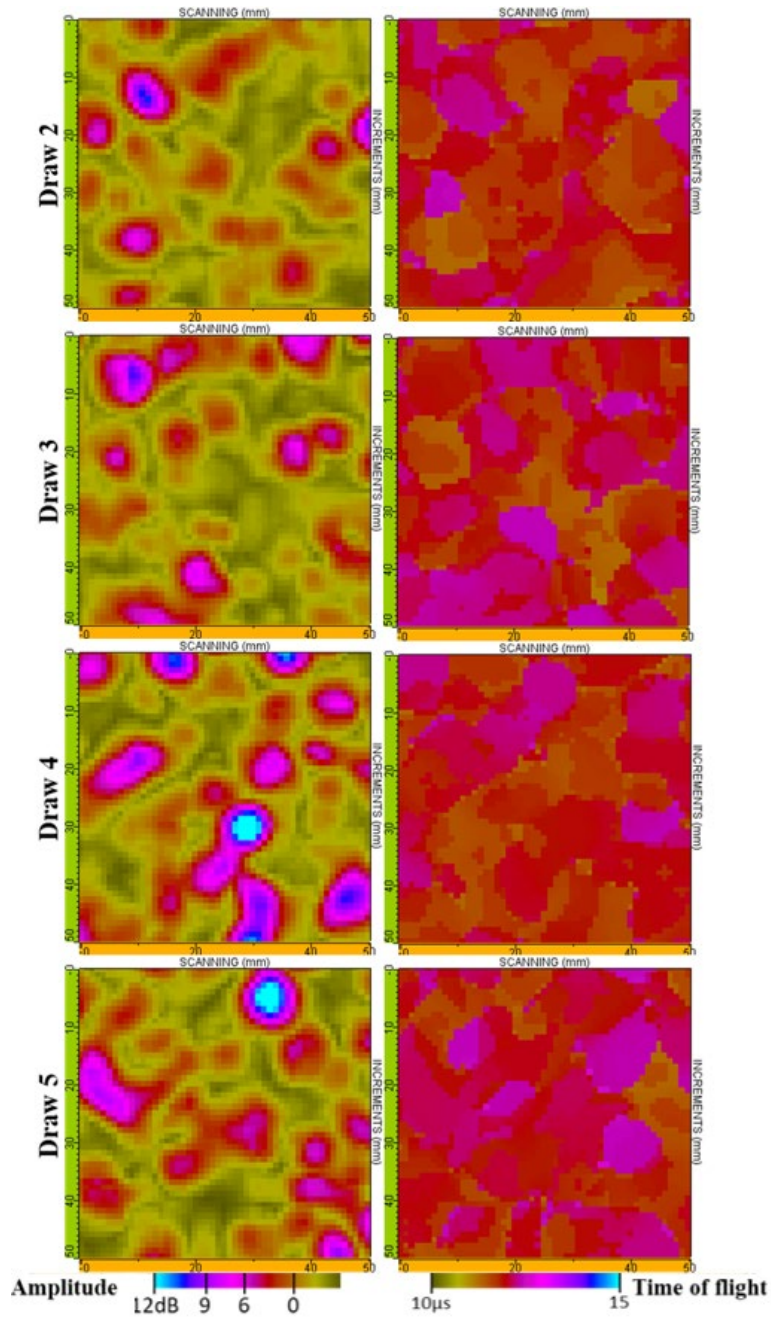
Figure B-13
Cells and velocity draws—amplitudes (left column) and times of flight (right column) as cells and velocity draws are varied, by row, for draw 1 to 5

Amplitude Measurements of Large Crack Tip Diffraction
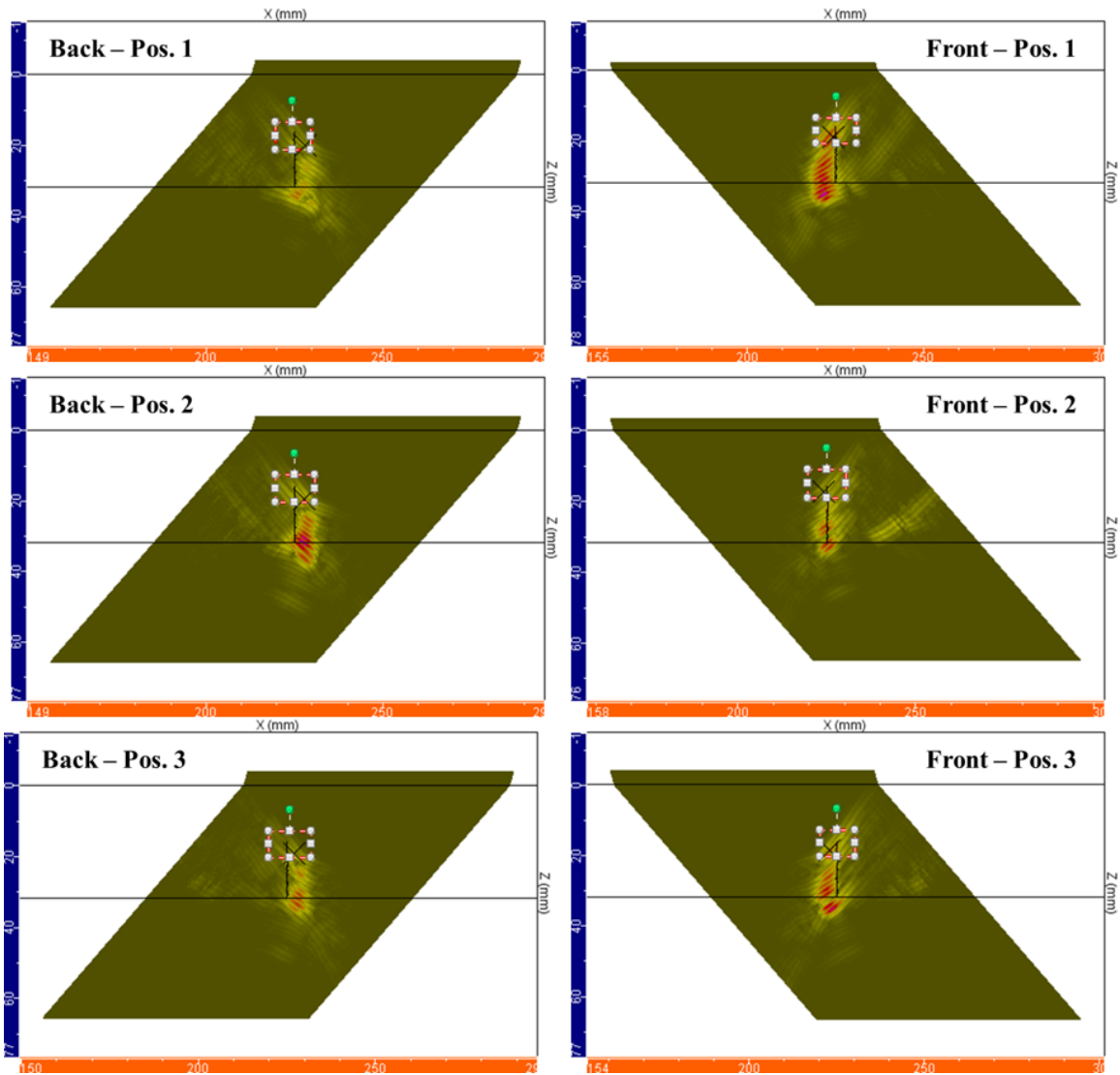
Figure B-14
Maximum amplitude for simulated large crack tip diffraction

C COMPUTING TIME

Table C-1
Computers used for simulations

Computer 1:	Computer 2:
• CPU: Intel i7-7700HQ • Processor (base/max) frequency: 2.8/3.8 GHz • RAM: 16 Gb • OS: Windows 10 • CIVA version: 2017 SP1	• CPU: Intel i7-4770 • Processor (base/max) frequency: 3.4/3.9 GHz • RAM: 16 Gb • OS: Windows 7 • CIVA version: 2017 SP1
Computer 3: • CPU: Intel i9-7940X • Processor (base/max) frequency: 3.1/4.4 GHz • RAM: 64 Gb • OS: Windows 10 • CIVA version: 2017 SP1	

Table C-2
CIVA computation time

Beam/Echo	Probe	Details	Time	Computer
Beam	Immersion 500 kHz	Homogeneous/bottom	7s	1
Beam	Immersion 500 kHz	Homogeneous/ cross-section	6s	1
Beam	Immersion 1 MHz	Homogeneous /bottom	33s	1
Beam	Immersion 1 MHz	Homogeneous/ cross-section	15s	1
Beam	Immersion 2.25 MHz	Homogeneous /bottom	12s	1
Beam	Immersion 2.25 MHz	Homogeneous/ cross-section	10s	1
Beam	Immersion 500 kHz	Coarse grain/prec. 1	2m 6s	1
Beam	Immersion 1 MHz	Coarse grain/prec. 1	5m 1s	1

Table C-2 (continued)
CIVA computations time

Beam/Echo	Probe	Details	Time	Computer
Beam	Immersion 2.25 MHz	Coarse grain/prec. 1	7m 48s	1
Beam	Immersion 500 kHz	Coarse grain/prec. 2	2m 55s	1
Beam	Immersion 500 kHz	Coarse grain/prec. 3	-	1
Beam	Immersion 500 kHz	Coarse grain/prec. 5	5m 49s	1
Beam	Immersion 500 kHz	Coarse grain/prec. 10	19m 49s	1
Beam	Immersion 1 MHz	Coarse grain/prec. 2	9m 15s	1
Beam	Immersion 1 MHz	Coarse grain/prec. 3	–	1
Beam	Immersion 1 MHz	Coarse grain/prec. 5	19m 1s	1
Beam	Immersion 1 MHz	Coarse grain/prec. 10	1h 4m 30s	1
Beam	Immersion 2.25 MHz	Coarse grainprec. 2	18m 43s	1
Beam	Immersion 2.25 MHz	Coarse grain/ prec. 3	–	1
Beam	Immersion 2.25 MHz	Coarse grain/prec. 5	44m 41s	1
Beam	Immersion 2.25 MHz	Coarse grain/prec. 10	2h 53m 30s	1
Echo	Immersion 500 kHz	Field prec. 3/ defect prec. 1	13m 18s	2
Echo	Immersion 500 kHz	Field prec. 3/ defect prec. 3	38m 54s	2
Echo	Immersion 500 kHz	Field prec. 3/ defect prec. 5	58m 25s	2
Echo	Immersion 500 kHz	Field prec. 3/ defect prec. 10	1h 58m 58s	2
Echo	Immersion 1 MHz	Field prec. 3/ defect prec. 1	44m 23s	2

Table C-2 (continued)
CIVA computation time

Beam/Echo	Probe	Details	Time	Computer
Echo	Immersion 1 MHz	Field prec. 3/ defect prec. 3	2h 7m 14s	2
Echo	Immersion 1 MHz	Field prec. 3/ defect prec. 5	3h 21m 21s	2
Echo	Immersion 1 MHz	Field prec. 3/ defect prec. 10	7h 4m 24s	2
Echo	Immersion 2.25 MHz	Field prec. 3/ defect prec. 1	1h 51m 3s	2
Echo	Immersion 2.25 MHz	Field prec. 3/ defect prec. 3	5h 21m 11s	2
Echo	Immersion 2.25 MHz	Field prec. 3/ defect prec. 5	9h 5m 52s	2
Echo	Immersion 2.25 MHz	Field prec. 3/ defect prec. 10	18h 38m 35s	2
Echo	Immersion 500 kHz	Sensitivity zone 40 × 40 mm	1m 35s	2
Echo	Immersion 500 kHz	Sensitivity zone 60 × 60 mm	3m 11s	2
Echo	Immersion 500 kHz	Sensitivity zone 80 × 80 mm	5m 57s	2
Echo	Immersion 500 kHz	Sensitivity zone 100 × 100 mm	9m 58s	2
Echo	Immersion 1 MHz	Sensitivity zone 30 × 30 mm	1m 34s	2
Echo	Immersion 1 MHz	Sensitivity zone 40 × 40 mm	3m 2s	2
Echo	Immersion 1 MHz	Sensitivity zone 60 × 60 mm	6m 23m 24s	2
Echo	Immersion 1 MHz	Sensitivity zone 80 × 80 mm	11m 35s	2
Echo	Immersion 2.25 MHz	Sensitivity zone 20 × 20 mm	1m 36s	2
Echo	Immersion 2.25 MHz	Sensitivity zone 30 × 30 mm	3m 20s	2
Echo	Immersion 2.25 MHz	Sensitivity zone 40 × 40 mm	5m 33s	2

Table C-2 (continued)
CIVA computation time

Beam/Echo	Probe	Details	Time	Computer
Echo	Immersion 2.25 MHz	Sensitivity zone 60 × 60 mm	13m 16s	2
Echo	Immersion 500 kHz	C-scan 80 × 100 mm	52h 35m 22s	2
Echo	Immersion 1 MHz	C-scan 80 × 100 mm	45h 34m 13s	2
Echo	Immersion 2.25 MHz	C-scan 80 × 100 mm	53h 55m 59s	2
Echo	Immersion 2.25 MHz	C-scan 50 × 50 mm	19h 52m 44s	2
Echo	Immersion 2.25 MHz	C-scan 50 × 50 mm, Vel. = 5330	19h 52m 56s	2
Echo	Immersion 2.25 MHz	C-scan 50 × 50 mm, Vel. = 5530	20h 45m 26s	2
Echo	Immersion 2.25 MHz	C-scan 50 × 50 mm, ΔVel. = 1%	18h 16m 11s	2
Echo	Immersion 2.25 MHz	C-scan 50 × 50 mm, ΔVel. = 2%	19h 0m 26s	2
Echo	Immersion 2.25 MHz	C-scan 50 × 50 mm, ΔVel. = 5%	21h 48m 48s	2
Echo	Immersion 2.25 MHz	C-scan 50 × 50 mm, ΔVel. = 10%	23h 48m 13s	2
Echo	Immersion 2.25 MHz	C-scan 50 × 50 mm, size = 1.5	85h 25m 38s	2
Echo	Immersion 2.25 MHz	C-scan 50 × 50 mm, size = 2.5	34h 33m 13s	2
Echo	Immersion 2.25 MHz	C-scan 50 × 50 mm, size = 4.5	13h 17m 7s	2
Echo	Immersion 2.25 MHz	C-scan 50 × 50 mm, elong. = 1.5	29h 51m 39s	2
Echo	Immersion 2.25 MHz	C-scan 50 × 50 mm, elong. = 2.5	22h 47m 19s	2
Echo	Immersion 2.25 MHz	C-scan 50 × 50 mm, elong. = 4.5	18h 23m 38s	2
Echo	Immersion 2.25 MHz	C-scan 50 × 50 mm, T1	12h 43m 42s	2

Table C-2 (continued)
CIVA computation time

Beam/Echo	Probe	Details	Time	Computer
Echo	Immersion 2.25 MHz	C-scan 50 × 50 mm, T2-1	14h 10m 2s	2
Echo	Immersion 2.25 MHz	C-scan 50 × 50 mm, T2-2	12h 6m 8s	2
Echo	Immersion 2.25 MHz	C-scan 50 × 50 mm, T3-1	13h 5m 16s	2
Echo	Immersion 2.25 MHz	C-scan 50 × 50 mm, T3-2	13h 10m 10s	2
Echo	Immersion 2.25 MHz	C-scan 50 × 50 mm, T3-3	12h 40m 57s	2
Echo	Immersion 2.25 MHz	C-scan 50 × 50 mm, D2	3h 43m 8s	3
Echo	Immersion 2.25 MHz	C-scan 50 × 50 mm, D3	3h 37m 0s	3
Echo	Immersion 2.25 MHz	C-scan 50 × 50 mm, D4	3h 31m 1s	3
Echo	Immersion 2.25 MHz	C-scan 50 × 50 mm, D5	3h 30m 29s	3
Echo	Immersion 500 kHz	C-scan 80 × 100 mm	9h 13m 3s	3
Echo	Immersion 1 MHz	C-scan 80 × 100 mm	28h 19m 3s	2
Echo	Immersion 2.25 MHz	C-scan 80 × 100 mm	34h 49m 40s	2
Beam	Contact 1 MHz	3D / Coarse grain/prec. 1	1h 20m 56s	1
Beam	Contact 1 MHz	Field precision 1	6m 52s	2
Beam	Contact 1 MHz	Field precision 2	9m 58s	2
Beam	Contact 1 MHz	Field precision 3	10m 41s	2
Beam	Contact 1 MHz	Field precision 5	18m 56s	2
Beam	Contact 1 MHz	Field precision 7	20m 36s	2

Table C-2 (continued)
CIVA computation time

Beam/Echo	Probe	Details	Time	Computer
Beam	Contact 1 MHz	Field precision 10	1h 3m 24s	2
Echo	Contact 1 MHz	Field prec. 10, defect prec. 1	4m 52s	2
Echo	Contact 1 MHz	Field prec. 10, defect prec. 3	9m 55s	2
Echo	Contact 1 MHz	Field prec. 10, defect prec. 5	12m 17s	2
Echo	Contact 1 MHz	Field prec. 10, defect prec. 10	21m 20s	2
Echo	Contact 1 MHz	J7010-4 SDHs, back	86h 16m 8s	2
Echo	Contact 1 MHz	J7010-4 large crack, front, 1	137h 12m 30s	2
Echo	Contact 1 MHz	J7010-4 large crack, back, 1	110h 30m 34s	2
Echo	Contact 1 MHz	J7010-4 large crack, front, 2	124h 12m 3s	2
Echo	Contact 1 MHz	J7010-4 large crack, back, 2	119h 7m 54s	2
Echo	Contact 1 MHz	J7010-4 large crack, front, 3	108h 34m 13s	2
Echo	Contact 1 MHz	J7010-4 large crack, back, 3	106h 40m 4s	2

Note: Simulation times that were not recorded are shown by a dash in the time column.
Prec. = precision; vel. = velocity; elong. = elongation.

Export Control Restrictions

Access to and use of this EPRI product is granted with the specific understanding and requirement that responsibility for ensuring full compliance with all applicable U.S. and foreign export laws and regulations is being undertaken by you and your company. This includes an obligation to ensure that any individual receiving access hereunder who is not a U.S. citizen or U.S. permanent resident is permitted access under applicable U.S. and foreign export laws and regulations.

In the event you are uncertain whether you or your company may lawfully obtain access to this EPRI product, you acknowledge that it is your obligation to consult with your company's legal counsel to determine whether this access is lawful. Although EPRI may make available on a case by case basis an informal assessment of the applicable U.S. export classification for specific EPRI products, you and your company acknowledge that this assessment is solely for informational purposes and not for reliance purposes.

Your obligations regarding U.S. export control requirements apply during and after you and your company's engagement with EPRI. To be clear, the obligations continue after your retirement or other departure from your company, and include any knowledge retained after gaining access to EPRI products.

You and your company understand and acknowledge your obligations to make a prompt report to EPRI and the appropriate authorities regarding any access to or use of this EPRI product hereunder that may be in violation of applicable U.S. or foreign export laws or regulations.

The Electric Power Research Institute, Inc. (EPRI, www.epri.com) conducts research and development relating to the generation, delivery and use of electricity for the benefit of the public. An independent, nonprofit organization, EPRI brings together its scientists and engineers as well as experts from academia and industry to help address challenges in electricity, including reliability, efficiency, affordability, health, safety and the environment. EPRI members represent 90% of the electric utility revenue in the United States with international participation in 35 countries. EPRI's principal offices and laboratories are located in Palo Alto, Calif.; Charlotte, N.C.; Knoxville, Tenn.; and Lenox, Mass.

Together…Shaping the Future of Electricity

3002013160